Liquid Droplets and Gas Interactions in Two-phase Flow

by

Maria Regina Gomes Zoby

Department of Mechanical Engineering
Imperial College of Science, Technology and Medicine
Exhibition Road
London SW7 2AZ

Thesis submitted for the degree of Doctor of Philosophy in the Faculty of Engineering of the University of London and for the Diploma of Membership of Imperial College

2010

I hereby declare that the work presented in this thesis is solely my own work and that to my knowledge this work is original except where otherwise indicated by reference to other authors. No part of this work has been submitted to any other degree or diploma.

Maria Regina Gomes Zoby

Abstract

The work focuses on the interactions of the two phases (liquid and gas) in droplet flows. Most studies of sprays do not resolve the liquid phase nor the near field and droplets are treated as point sources of mass, momentum, energy and species. In the present work, two- and three-dimensional Direct Numerical Simulations of fully resolved droplet arrays are analysed. Simulations of droplets arrays in inert and reacting environments are performed and evaporation rates and fuel vapour mixing in laminar and turbulent flows are assessed.

The novel model developed in this work combines the one- and two-fluid formulations for multiphase flows. The energy transport equation is solved based on a one-fluid formulation while the species, velocities and pressure equations are solved with a two-fluid formulation. In addition, a Level Set technique is combined with the Ghost Fluid method in a mass conserving approach in order to track the liquid interfaces. The numerical algorithm was parallelised in order to satisfy the computational demand of the simulations.

The validation tests performed show that the model implemented is able to capture the dynamic behavior of droplet interactions and heat and mass transfer across interfaces. The effects of turbulence and droplet density on droplet evaporation rates in reacting flows is investigated for n-heptane and kerosene droplet arrays. The evaporation rates are compared to existing models commonly used in Large Eddy Simulations and Reynolds-averaged Navier-Stokes computations. A shell around the droplet approach is proposed in order to estimate the gas properties used in these models. It is noted that this approach allows the models to capture transients and provides predictions of the evaporation rates with errors around 2%.

The gas phase mixing is assessed by examining the distribution of scalar dissipation. Novel multi-conditional models are proposed that use mixture fraction, distance to previous droplet and zone of location as the conditioning variables for the scalar dissipation. The scalar dissipation is found to be well predicted in terms of magnitude and distribution. The accurate representation of the mean scalar dissipation is achieved. The β-PDF description of the mixture fraction seems to capture well the global behaviour for a laminar environment and for time averaged results in the turbulent cases.

Acknowledgements

There are many people who helped me during this long and intense period of my PhD. First, I would like to express my sincere gratitude to my supervisor Prof. Andreas Kronenburg for the opportunity of doing the PhD and for the many questions and advices that guided my work. I would also like to thank Dr. Fred Marquis for accepting being my supervisor in the last years, for the fundamental guidance and priceless support.

During this period, I met special people and their friendship is possibly the most important outcome of this experience. I am particularly thankful to Dr. Salvador Navarro-Martinez, my dear friend and non-official supervisor for his vital help. I thank all my Imperial College friends and mostly Francesco Bottone, Nakul Prasad, Pierre Le Fur, Ghenadie Bulat, Konstantina Vogiatzaki and the "new generation" of room 600. The most special thanks to the ones who became my family in London: Claudio Lettieri, Bruno Carmo, Sgouria Lyra and Sandeep Saha. I wish also to thank my friends Tiziana Rossetti, Magdalena Wolkanowska, Danilo Fumagalli, Nicola Debiasi and my volleyball partners for all the special moments lived together.

This work would not had been realised without the support of my family. Their love and trust were present everyday. I could never put in words how thankful I am or how important they are to me. I am also grateful to my friends across the Atlantic who always supported me througout this period.

Finally, I would like to acknowledge the CNPQ - Ministery of Science and Technology of Brazil - for the financial support (Process 200277/2006-5) of these studies.

This thesis is dedicated with love
to my parents and my brother.

Nomenclature

$_b$	backward
$_f$	forward
$_{i,j,k}$	coordinate indices
$_d$	droplet
$_g$	gas phase
$_l$	liquid phase
$_s$	droplet surface
α_h	enthalpy diffusion coefficient
α_p	volume fraction
$\bar{\Gamma}$	Gamma function
$\delta(d)$	Delta dirac function of a distance d
δ_{ik}	Kronecker symbol
ℓ_0	length scale
ϵ	turbulent energy dissipation rate
η	Kolmogorov length scale
Γ	diffusion coefficient of a general variable Ω)
κ	interfacial curvature

μ_k dynamic viscosity of phase k

μ dynamic viscosity

μ_f mean value of f

ν kinematic viscosity

Ω general variable

ω_α chemical source term of species α

ω_{rad} heat loss rate due to radiation

ω_T chemical reaction source term

ϕ level set function

ρ density

ρ_k density of phase k

σ surface tension

σ_f variance of f

σ_{ik} viscous stress tensor

σ_{sgs} sub-grid standard deviation

τ fictitious time

τ_0 time scale

τ_η Kolmogorov time scale

τ_c chemical time scale

τ_t turbulent time scale

τ_{ij} stress tensor

θ_k indicator of phase k

$\upsilon''_{\alpha,R}$ stoichiometric coefficients in backward reaction

$\upsilon'_{\alpha,R}$ stoichiometric coefficients in forward reaction

υ_0 velocity scale

υ_η Kolmogorov velocity

ξ^n_α continuous stochastic field n for specie α

ζ interface thickness

$\bar{T}$ domain filtered temperature

$\dot{m}_d$ droplet evaporation rate

ℓ integral length scale

$\hat{V}_{k,\alpha}$ volumetric diffusion velocity of species α across the interface

Π_k mass source term of phase k

$\rho_{cell,CF}$ density of the controlled phase in the cell

ρ_{CF} density of the controlled phase

A_j pre-exponential factor j-th reaction

A_{eq} equivalent area

B_k mass transfer number

B_q heat transfer number

c droplet spacing

c_p specific heat at constant pressure

$c_{p\alpha}$ specific heat at constant pressure of species α

c_{pp} specific heat at constant pressure of particle p

D mass diffusivity

d diameter

d_0 droplet initial diameter

D_α diffusivity of species α

$D_{k,\alpha}$ diffusion coefficient of species α in phase k

$D_{k,h}$ enthalpy diffusion coefficient of phase k

Da Damkhöler number

f mixture fraction

f_d mixture fraction inside the droplet

F_g graviational force

$F_{ext,k}$ external forces in k-direction

f_{max} maximum value of mixture fraction

f_{stoich} stoichiometric coefficient

F_{st} surface tension force

g_i gravitational acceleration in i-direction

H Heaviside step function

h enthalpy

h^0_α enthalpy of formation of species α

h_k enthalpy of phase k

h_{fg} latent heat of evaporation

H_{st} surface tension force factor

I impact number

J diffusion component of the evaporation rate

J_p pressure jump condition

$J_{\alpha,i}$ diffusional flux of species α

J_ρ density jump condition

k thermal conductivity

k_j rate coefficient of j-th reaction

$k_{b,R}$ rate coefficient for backward reactions

$K_{C,R}$ equilibrium constant

$k_{f,R}$ rate coefficient for forward reactions

L characteristic lengthscale

l axial distance

Le Lewis number

M_α molecular weight of species α

M_m molecular weight of the mixture

m_{CF} mass of the controlled phase

m_d droplet mass

m_{teor} theoretical mass of the controlled phase

N scalar dissipation

N_α number of species

N_f conditioned (on f) scalar dissipation

N_R number of reactions

N_s number of scalars

Nu Nusselt number

Oh	Ohnesorge number
p	thermodynamic pressure
P_f	probability density function of f
p_{pv}	partial pressure
Pr	Prandtl number
q	heat
R	gas constant of the mixture
r	radius
r_d	droplet radius
R_u	universal gas constant $R_u = 8.315(kJ/kgmolK)$
$r_{b,R}$	reaction rates of the backward direction
$r_{f,R}$	reaction rates of the forward direction
Re	Reynolds number
Re_η	Kolmogorov Reynolds number
Re_p	Reynolds number of particle p
S_k	momentum exchanged between the phases
$S_{k,h}$	enthalpy source in phase k
S_{Y_α}	source term of species α
Sc	Schmidt number
Sh	Sherwood number
St	Stokes number
T	temperature

t time

t_c characteristic timescale

t_I integral time scale

T_r reference temperature

T_∞ inflow temperature

T_{air} air temperature

T_{boil} boiling temperature

T_d interface temperature

U mean velocity

u velocity

U_c convective velocity

u_c convective interface velocity

u_i velocity in i-direction

u_∞ inflow velocity

u_{evap} interface velocity due to evaporation

u_{iI} interface velocity

$u_{k,i}$ velocity of phase k in i-direction

u_{mean} mean velocity

u_{rel} relative velovity

$V_{cell,CF}$ volume of the controlled phase in the cell

$v_{correct}$ correcting velocity

$V_{k,\alpha,i}$ component of the mass diffusion velocity in i direction of species α in phase k

W_α molar mass of specie α

$W_{k,\alpha}$ rate of production of species α

We Weber number

x_i coordinate in i-direction

Y_α mass fraction of species α

Y_r reference mass fraction

$Y_{k,\alpha}$ mass fraction of species α in phase k

$'$ forward reaction

$''$ backward reaction

Contents

List of Figures

List of Tables

Chapter 1

Introduction

1.1 Background and Motivation

The energy consumption in the world increases around 3% per year and projections show an expected growth of 49% from 2007 to 2035 (EIA, 2010). In 2007, the total world energy use was 495 quadrillion Btu, including generation by liquid fuels, coal, natural gas, renewables and nuclear as shown in Fig. 1.1. Responsible for almost 35% of the consumption, liquid fuels are used in combustion systems such as engines, furnaces and propulsion devices. Although the projections show that the percentage of liquid fuels tend to decrease, it must remain as the main source of energy for the next decades (see Fig. 1.1).

In this context, liquid fuel sprays have been studied extensively (Imaoka and Sirignano, 2005; Tanguy et al., 2006; Reveillon and Vervisch, 2005) because of their importance for many combustion systems. The present thesis addresses some important issues on liquid sprays modelling using Computational Fluid Dynamics (CFD). CFD has become an important tool for design and optimisation in the last years, however, improvements in the modelling are still necessary in order to be able to capture the spray dynamics and guarantee accuracy of the numerical predictions.

Theoretical and numerical studies provide an alternative to experimental investigations, but the modelling of the physical processes involved is difficult, especially in turbulent environments due to the range of associated length and time scales

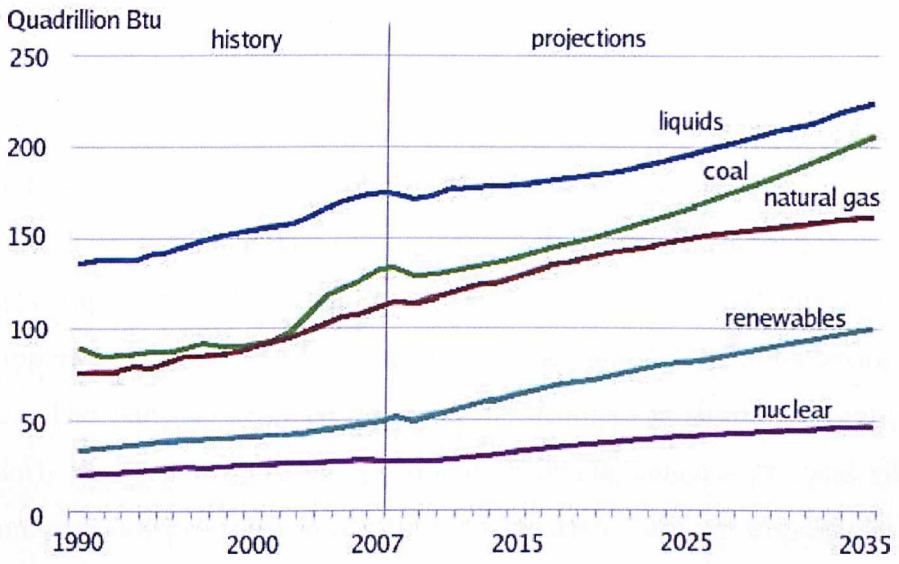

Figure 1.1: World energy consumption (EIA, 2010).

which may spread over several orders of magnitude. The interactions of the physico-chemical processes such as heat and mass transfer across interfaces, turbulence and chemical reactions make the problem more complex and difficult to model. To the knowledge of the author, only few numerical works exist (Imaoka and Sirignano, 2005; Stauch and Maas, 2007; Stauch and Maas, 2008), for example, that are capable of directly quantifying the effect of droplets interactions on evaporation rate and subsequent ignition and combustion.

In reacting sprays, where chemical reactions occur, the fuel is injected into a combustion chamber where the spray develops, evaporates and mixes with air to form an ignitable mixture. The development of the sprays includes atomisation of the liquid phase and the turbulent interactions between the phases. The liquid breakup and evaporation determine key characteristics of the energy conversion processes as they govern the mixture formation process, determining combustion efficiency and pollutant formation. Commonly, the breakup and evaporation are numerically described by empirical correlations derived from global balances under steady-state conditions. It is questionable whether this approach is valid for different fuels and also for transient processes. In order to gain better understanding of

the evaporation and mixture formation processes, the interactions of the governing phenomena have to be considered.

Experimental investigations on single droplet evaporation have been performed in order to quantify the effects of turbulence on the evaporation rate of different fuels (Birouk et al., 2000; Wu et al., 2001). However, conventional spray studies are very complex and do not allow to easily quantify crucial quantities such as local temperature gradients at the droplet surface and interactions between various droplets. The parameter space between the droplets is simply too large, studies of regularly ordered droplet arrays would facilitate analysis of local effects that determine evaporation rates and mixture formation, but are impossible to realise experimentally.

The present work addresses the modelling for droplet arrays as an idealisation of sprays. The relative simplicity of using droplets instead of the complexity of real spray flows, allows a detailed studied of the physics and chemistry of the complex interaction mechanisms between the liquid and the gas phases. The knowledge gained from these investigations may be used to advance and improve the efficiency of liquid-fuelled combustion systems.

1.2 Present Contribution

Most studies of reacting sprays do not resolve the liquid phase nor the near field and the liquid phase is represented by droplets that are treated as point sources of mass, momentum and energy. These investigations neglect the conditions in the immediate neighbourhood of the individual droplet. However, evaporation and, to some degree combustion, are directly dependent on the local conditions close to the individual droplets.

In the present work, a novel model using a hybrid one- and two-fluid formulation coupled with an interface tracking method (a mass conservative Level Set approach) with the Ghost Fluid method, is implemented and tested to simulate evaporating and burning droplet arrays in stagnant and convective environments. The liquid and gas phases are fully represented, capturing the interface location and resolving

all the scales of turbulence through Direct Numerical Simulations (DNS).

This work assesses the effects of droplet density and turbulence on evaporation rates in inert and reactive turbulent environments. Evaporation rates obtained with the new model are compared to experimental investigations on single droplet evaporation (Birouk et al., 2000; Wu et al., 2001) and are also compared to existing models of droplet evaporation. The differences are quantified and analysed. Improvements in the present models are proposed in order to increase the accuracy of the numerical predictions.

Furthermore, the accuracy of mixture fraction based combustion models rely on accurate closures of the mixture fraction probability density function (PDF) and the scalar dissipation. However, the local mixture fraction field in inter-droplet regions is fundamentally different from cell averaged values commonly used in the CFD context. This difference can have profound effects on the accuracy of the numerical results. The model implemented is used to simulate several droplet loadings and the sensitivity of the local gas-phase mixing field is analysed and quantified. Investigations are performed in two and three-dimensional test cases and new closures to the combustion models are proposed.

1.3 Thesis Outline

This thesis is divided in six chapters. The next chapter introduces the two-phase flow characteristics and modelling. The fundamentals of spray dynamics are reviewed and the main modelling issues are discussed. A review on the breakup, combustion and interface tracking methods is also presented.

Chapter 3 presents a detailed description of the novel model developed in this work. The discretisation of the governing equations as well as the Level Set and Ghost Fluid methods are described. The various test cases performed in order to validate the model and quantification of the errors are also presented.

In Chapter 4, a review of the evaporation models is shown. The predictions of evaporation rates for *n*-heptane and kerosene droplets using these models are compared to the results obtained in the DNS using the methodology described in

Chapter 3. The results of the simulations are also compared to experimental data in order to be validated. The influence of the definition of thermophysical properties of the gas phase in the predictions of the evaporation rates is analysed and quantified. A new concept of properties definition is proposed.

Chapter 5 presents the results of gas-phase mixing in inert environments. Two and three-dimensional evaporating droplet arrays of methanol in stagnant, laminar and turbulent environments are assessed. Local mixing inhomogeneities, mixture fraction PDFs and scalar dissipation are investigated. New models for scalar dissipation are proposed.

Finally, Chapter 6 presents the conclusions of the thesis and discusses possible future works.

Chapter 2

Two-phase Flows

2.1 Introduction

Multi-phase flows occur in systems composed of mixtures of gas, liquids or solids. When only two phases are present, the flow is named two-phase. The gas-liquid flow, investigated in this work, is the most common of the two-phase cases. It combines the characteristics of a deformable interface with significant jumps in properties between the phases. Different regimes, depending on the local flow conditions and structures, can be identified. Gas-liquid flows in a pipe are defined as bubble, slug, churn, annular or wispy flows (Hewitt, 1982). Similarly, flow regimes in horizontal flows can be stratified, stratified-wavy, bubble, annular or intermittent.

Sprays are a particular type of two-phase flow where, typically, the liquid is injected through an injector at high velocity in a gaseous environment. The liquid is atomised, breaking into ligaments and droplets and possibly evaporating. Sprays can be non-reacting - when the liquid does not undergo any chemical reaction such as a paint or insecticide spray - or reacting - when fuel is injected and reaches the conditions to undergo combustion.

The present chapter reviews important works on sprays, describing the fundamentals of spray dynamics and presenting the modelling approaches found in the literature. The main focus is on reacting sprays which are used in liquid-fuelled devices for example those found in turbines and engines. The dynamics of these sprays

involve the interactions between the liquid and gas phases and, more especifically, the liquid breakup, evaporation and combustion.

The following section presents the physics involved in sprays dynamics with special attention to the liquid and gas interactions. The processes of atomisation, evaporation and combustion are described. Section 2.3 describes the flow field governing equations followed by the chemical reactions in Section 2.4. Section 2.5 presents an overview on the modelling involving two-phase flows covering aspects of one and two-fluid formulations, interface tracking methods, jump conditions such as surface forces, compressibility and combustion.

2.2 Sprays Dynamics

In reacting sprays the fuel is injected into a combustion chamber where the spray develops, evaporates and mixes with air to form a combustible mixture. Separation of these phenomena and the interactions between them is essential for the complete understanding on the dynamics of sprays. In this section, the atomisation, evaporation and combustion of sprays are presented as well as the interactions between them.

2.2.1 Atomisation

In most of the spray devices, it is desired to enhance mass transfer rates by increasing the liquid surface area. This is the main goal of atomisation which is the process of breaking the larger liquid structures into smaller and smaller structures. The atomisation plays an important role and strongly influences the combustion efficiency. An efficient atomisation reduces the size of the fuel droplets, leading to higher volumetric heat transfer rates, shorter evaporation time resulting in easier ignition and wider burning ranges (Lefebvre, 1989).

Liquid sprays are basically composed of a dense region where instabilities grow followed by primary atomisation and a dispersed region where primary and mostly secondary breakup take place (as shown in Fig. 2.1). In the dense region, the liquid structures have a length scale of the order of milli-metres while in the dispersed

phase, the droplets are of the order of micro-metres. The dense-spray zone close to the injector, denoted liquid core, is characterised by mean liquid volume fraction near unity. In this zone, the interface surface relative to the liquid volume is very small because the liquid core is not composed of arrays of droplets but regions of large liquid fractions.

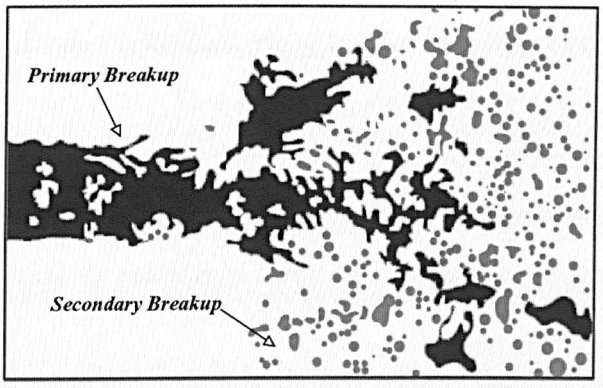

Figure 2.1: Spray atomisation.

The dispersed region that follows the liquid core consists of large, irregular, ligament-like elements resulting from this primary breakup. Following this region, ligaments break and form smaller round drops near the edge of the flow (shear layer), resulting from the effect of this secondary breakup.

As described, the primary breakup initiates atomisation of the jet, controlling the extent of the liquid core and yielding the unstable ligaments that are intrinsically prone to deformation and secondary breakup. Different breakup regimes exist and are discussed later. In addition, the high-pressure combustion processes involve conditions (high pressure and high temperature - near the thermodynamic critical point) in which the surface tension becomes small, facilitating droplet deformation and secondary breakup.

The secondary breakup causes the ligaments and large droplets formed by the primary breakup to break into smaller droplets which characterises the dilute zone. The secondary breakup also defines the spray mixing rates by controlling droplet sizes. Because of the droplet formation, the mean liquid volume fraction in the dispersed region decreases significantly if compared to the liquid core. The liquid

volume fraction of the dispersed region is small and the interface surface relative to the liquid volume is large. The small liquid volume fraction of the dispersed-flow region implies that droplet collisions are improbable (Faeth, 1987).

Near the liquid core, the largest droplets have velocities close to the mean liquid velocities at the jet exit. However, the droplet velocities decrease with decreasing droplet size and increasing radial distance from the jet centreline. Across the multiphase mixing layer, the gas velocities, close to the velocities of the smallest droplets, are small and nearly constant. This behavior shows the relatively ineffective mechanism of momentum exchange in the dilute multiphase mixing layer because the flow is dilute and large droplets that contain most of the momentum respond slowly to drag forces due to their relatively large inertia and high droplet response time (Faeth, 1996).

The different breakup regimes for various liquids are presented in Fig. 2.2 as function of the Weber ($We = \rho U^2 d/\sigma$) and the Ohnesorge ($Oh = \mu/\sqrt{\rho\sigma d}$) numbers. The Weber number indicates the relative importance of the droplet inertia compared to the surface tension while the Ohnesorge number relates the viscous forces to the droplet inertia and surface tension.

The deformation regime occurs when surface tension is relatively higher than the inertial force (low We) or when viscous forces are higher than inertial and surface tension forces (high Oh). When inertial forces increase, breakup occurs following different regimes such as bag and shear (stripping) breakups (see Fig. 2.3). Other possible breakup regimes are vibrational and piercing.

The primary and secondary liquid breakup in pressure-atomised sprays are both influenced by the turbulence close to the jet exit. Studies of sprays have shown that especially primary breakup is strongly affected by the flow, by turbulence development at the jet exit and by the profile of the injector contraction (Wu et al., 1995). Current understanding of the physics behind primary breakup is limited and complete data set describing this zone does not exist because of difficulties of observations within dense sprays (Lebas et al., 2009). Secondary breakup and the gas-liquid interactions modify the droplets and ligaments properties before measurements can be made at the region where primary breakup occurs. Furthermore, it is

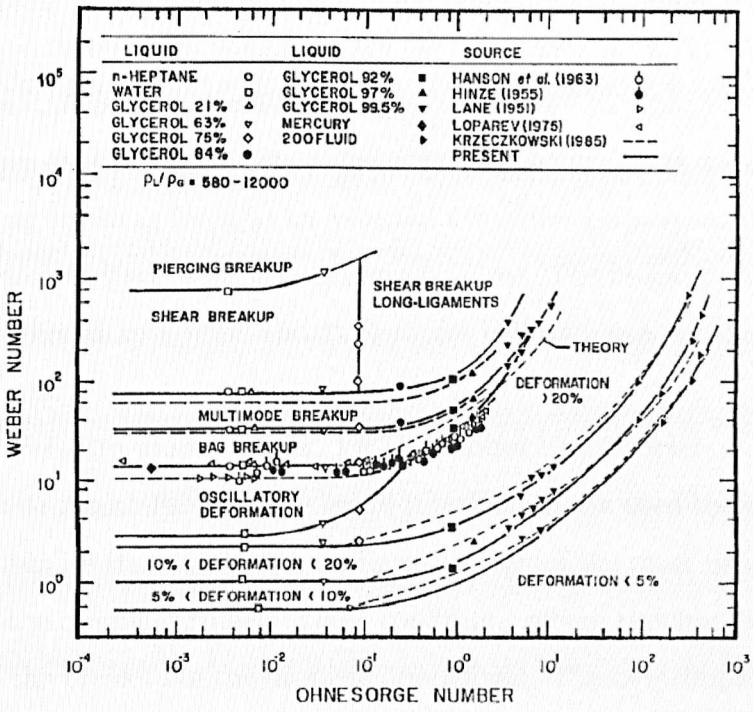

Figure 2.2: Droplet deformation and secondary breakup regimes (Faeth, 1996).

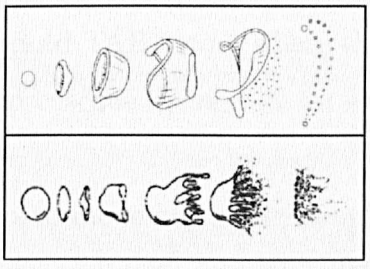

Figure 2.3: Bag (top) and shear (bottom) breakup regimes (Smith, 2002).

a complex task to characterise the flow and turbulence development at the jet exit.

2.2.2 Droplet Breakup Models

Different models for droplet breakup can be found in the literature. The most widely used are the wave breakup models, including the Taylor Analogy Breakup (TAB) used for low Weber numbers and the Wave Breakup model used for high Weber

numbers. These two models are both deterministic, with single scale production of droplets. For turbulent flows, there are also stochastic breakup models where a stochastic breakup contribution is introduced.

The TAB model (Taylor, 1963) analyses droplet distortion as a spring-mass system, considering the drag force as an external force, the surface tension as a spring force and the droplet viscous force as a damping force. The breakup occurs when the distortion is higher than a limit and the droplet children size is defined respecting energy conservation.

The Wave Breakup model (Reitz, 1987) assumes that droplets breakup due to Kelvin-Helmholtz instabilities on the liquid interface. Reitz used the wave equation of Taylor to estimate the wavelength and growth rate of the most unstable wave on the surface of the original droplet. Thus, conditions where the amplification of the waves leads to the breakup of the droplets are defined. The new droplets are formed based on the growth rate of the wave instability.

In practical combustion applications, the formation of droplets with different sizes occurs. This is mainly because of the high relative velocity between droplets and the gas phase. However, the TAB and Wave models do not take into account this characteristic. An enhanced TAB model where the parameters of the product droplet size follow a breakup cascade defined by an exponential law was proposed by Tanner, 1997.

Several works have proposed modelling of the droplet size distributions and the most simple and common approach is to impose a droplet size distribution to the breakup such as a gaussian or log-normal distribution. A review of the available methods is presented in Babinsky and Sojka, 2002.

More recently, stochastic models have been developed for turbulent flows in the context of Large Eddy Simulations (LES). The Stochastic model proposed by Apte et al., 2003, calculates the breakup frequency and critical radius from aerodynamic effects and surface tension forces. It uses the Fokker-Planck equation for the PDF of diameters to determine the sizes of the new droplets. Other stochastic approaches have been proposed by Liu et al., 2006 and Jones and Lettieri, 2010.

2.2.3 Turbulence Interactions

The turbulence development depends on the liquid and gas injection conditions and on the interactions between the phases. As mentioned before, the atomisation is strongly dependent on the turbulence interactions. Shear, due to velocity gradients at the jet inflow, causes the formation of a turbulent layer. The effects of this turbulent boundary layer added to the effects of the turbulence of each phase generate instabilities and cause primary and secondary breakup. The turbulence effects are also important in the evaporation and combustion of sprays (discussed later in this section). However, quantifying the effects of turbulence experimentally is always a difficult task.

The liquid and gas phases affect one another and define a resulting flow field. The flow field governing equations are described in detail later. The main interactions between the droplets and the gas phase turbulence in sprays are: dispersion of the droplets because of turbulence, modification of turbulence by the motion of the droplets and modification of the transport rates between the phases because of turbulence fluctuations.

Two turbulence modification mechanisms are particularly important: the exchange of kinetic energy between a particle and an eddy as the particle accommodates to the eddy velocity (turbulence modulation decreasing turbulent fluctuations) and the direct disturbance of the continuous-phase velocity field by particle wakes (turbulence generation increasing turbulent fluctuations). Turbulence generation tends to dominate turbulence modification in sprays because they are dilute dispersed flows with large separated flow effects and thus strong particle wakes (Faeth, 1996). Advance in understanding the properties of the wakes in turbulent environment is needed to better understand turbulent mixing phenomena.

2.2.4 Evaporation and Combustion

When a liquid droplet or ligament is exposed to a hot environment, the temperature of the liquid rises and evaporation occurs. Depending on the ambient conditions, the liquid temperature may increase until it reaches the boiling temperature. Once this

temperature is reached, a quasi-steady regime is established and the heat transfer to the liquid results only in evaporation. Furthermore, if the conditions for flamability are reached, combustion takes place.

Spray evaporation is defined by exchanges of mass, species, momentum and energy at the interface between the liquid and the gas-phase. The mixing between the fuel vapour and the oxidizer, which controls the combustion process, is then affected by these interface exchanges. The overall behaviour of reacting sprays may be very different. Chiu et al., 1982, proposed a spray combustion regime classification based on the number of droplets and the separation space between them (Fig. 2.4). According to this classification, combustion can occur as a single droplet or as group phenomena (internal, external or external sheath).

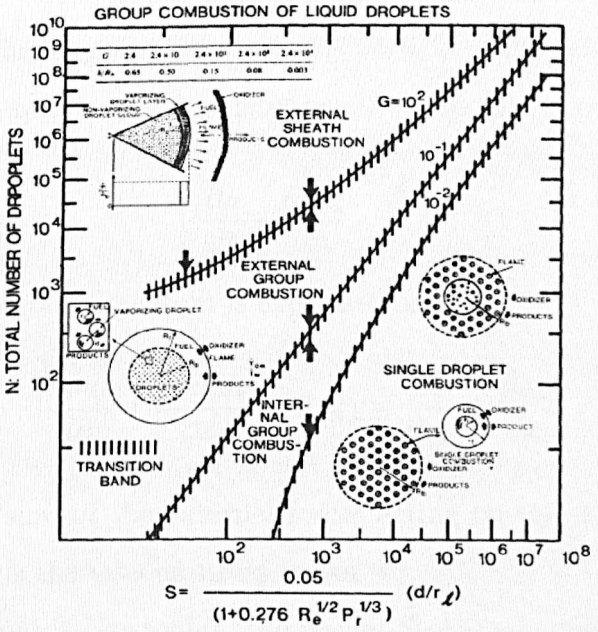

Figure 2.4: Droplet combustion regimes (Chiu et al., 1982).

The single droplet combustion occurs if the distance between the droplets is large enough so the effects of other droplets are negligible. In this regime, the droplet flame does not merge with neighbour flames but remains isolated. This direct combustion of droplets may occur when droplets reach the combustion zone

of sprays. In most applications, however, combustion occurs around a group of droplets and the droplets are local sources of fuel. Internal combustion occurs when an inner zone of the sprays reaches the conditions for the chemical reactions to occur and then the flame is sustained within the region.

2.3 Flow Field Governing Equations

The fluid flow can be described by the governing equations derived from the principles of mass, momentum and energy conservation in a continuum fluid. The derivation of these equations can be found in Versteeg and Malalasekera, 1995; Potter and Wiggert, 2002. In two-phase flows, these equations must take into account the interactions between the phases and the exchanges through the interfaces. Particular numerical issues of the discretisation of these equations for two-phase flows are presented later in this chapter.

The continuity equation, which describes the principle of conservation of mass, is written as

$$\frac{\partial \rho}{\partial t} + \frac{\partial \rho u_i}{\partial x_i} = 0 \tag{2.1}$$

The conservation of momentum is expressed as

$$\frac{\partial \rho u_k}{\partial t} + \frac{\partial \rho u_i u_k}{\partial x_i} = F_{ext,k} - \frac{\partial p}{\partial x_k} + \frac{\partial \sigma_{ik}}{\partial x_i} \tag{2.2}$$

where $F_{ext,k}$ is the sum of the external forces acting on the fluid (gravity, etc) in k-direction and σ_{ik} is the viscous stress tensor.

Assuming the fluid is Newtonian, the Navier-Stokes equations are written as

$$\frac{\partial \rho u_k}{\partial t} + \frac{\partial \rho u_i u_k}{\partial x_i} = -\frac{\partial p}{\partial x_k} + \frac{\partial}{\partial x_i}\left(\mu\left(\frac{\partial u_k}{\partial x_i} + \frac{\partial u_i}{\partial x_k} - \frac{2}{3}\delta_{ik}\frac{\partial u_j}{\partial x_j}\right)\right) + F_{ext,k} \tag{2.3}$$

where δ_{ik} is the Kronecker delta and μ is the viscosity of the fluid.

The species conservation, based on the continuity equation, is given by

$$\frac{\partial \rho Y_\alpha}{\partial t} + \frac{\partial \rho Y_\alpha u_i}{\partial x_i} = \omega_\alpha - \frac{\partial J_{\alpha,i}}{\partial x_i} \tag{2.4}$$

where Y_α is the mass fraction of the specie α in the fluid, ω_α is the mass source term and $J_{\alpha,i}$ is the diffusional flux with contribution of concentration gradients, mass diffusion due to temperature, external forces and pressure gradients.

If diffusion is described by Fick's law, valid for binary diffusion, then

$$J_{\alpha,i} = -\rho D_\alpha \frac{\partial Y_\alpha}{\partial x_i} \tag{2.5}$$

where D_α is the diffusion coefficient of species α.

The enthalpy of the gas mixture, h, is a function of species mass fractions and temperature.

$$h = h(Y_1, Y_2, ..., Y_n, T) = \sum Y_\alpha (h_\alpha^0 + \int_{T_0}^{T} c_{p\alpha} dT) \tag{2.6}$$

where h_α^0 is the enthalpy of formation and $c_{p\alpha}$ is the heat capacity of species α.

At low Mach number, the conservation equation is

$$\frac{\partial \rho h}{\partial t} + \frac{\partial \rho h u_i}{\partial x_i} = \frac{\partial p}{\partial t} + u_i \frac{\partial p}{\partial x_i} + \frac{\partial}{\partial x_i}\left(\rho \alpha_h \frac{\partial h}{\partial x_i}\right) + \frac{\partial}{\partial x_i}\left(\rho D_\alpha \sum h_\alpha \frac{\partial Y_\alpha}{\partial x_i}\right) - \rho \omega_{rad} \tag{2.7}$$

where α_h is the enthalpy diffusion coefficient ($\rho \alpha_h = k$), ω_{rad} is the heat loss rate due to radiation.

If variations of pressure in time and space and radiation are negligible, the temperature equation, derived from the energy conservation equation, can be written as

$$\frac{\partial \rho c_p T}{\partial t} + \frac{\partial \rho c_p T u_i}{\partial x_i} = \frac{\partial}{\partial x_i}\left(k \frac{\partial c_p T}{\partial x_i}\right) + \rho D_\alpha \frac{\partial T}{\partial x_i}\left(\sum c_{p\alpha} \frac{\partial Y_\alpha}{\partial x_i}\right) + \omega_T \tag{2.8}$$

where c_p is the heat capacity of the fluid, T is the temperature and ω_T is the chemical reaction source term.

In this work, the ideal gas equation of state is used for the gas phase. Therefore, the pressure, density and temperature are related through

$$p = \rho R T \tag{2.9}$$

where R is the gas constant for the gas mixture ($R = \frac{R_u}{M_m}$).

For the liquid phase, the temperature is assumed constant and at saturation value so the physical properties are constant.

2.3.1 Governing Equations Resolution

Turbulence is often generated by velocity gradients and can be considered as a combination of eddies of different sizes. The large scale eddies breakup producing eddies of smaller size. Following the same mechanism, the eddies of smaller size breakup into smaller and smaller eddies. This is referred to as the energy cascade (Tennekes and Lumley, 1972). The rate of dissipation, ϵ, is determined by the transfer of energy from the largest eddies. The cascade continues until the Reynolds number, $Re = \frac{u\ell}{\nu}$, is sufficiently small and the kinetic energy dissipates by molecular viscosity. The isotropy hypothesis states that at sufficient high Re numbers, the small scales are isotropic.

According to the Kolmogorov equilibrium theory (Tennekes and Lumley, 1972), the rate of transfer of kinetic energy from the large scales to the dissipative scales, ϵ, is balanced by the rate at which the energy is dissipated in the small scales. The Kolmogorov scales can then be defined by the energy dissipation rate, ϵ, and the kinetic viscosity, ν, as

$$\eta \equiv (\nu^3/\epsilon)^{\frac{1}{4}}, \quad \tau_\eta \equiv (\nu/\epsilon)^{\frac{1}{2}}, \quad \upsilon_\eta \equiv (\nu\epsilon)^{\frac{1}{4}}.$$

It is noted that the Kolmogorov Reynolds number is Re_η is equal to one. Furthermore, at these scales, the viscous forces are significant and lead to the dissipation of the turbulent fluctuations to heat. As a result, the Kolmogorov scale is considered the smallest scale of a turbulent flow field. The ratio of the Kolmogorov scales to the large scales expresses the extent of the turbulent problem and are related to Re by

$$\frac{\eta}{\ell_0} \sim Re^{-\frac{3}{4}}, \quad \frac{\upsilon_\eta}{\upsilon_0} \sim Re^{-\frac{1}{4}}, \quad \frac{\tau_\eta}{\tau_0} \sim Re^{-\frac{1}{2}}.$$

The mesh size and the time step define the length and time scales resolved by the discretisation of the governing equations. Direct Numerical Simulations (DNS) resolve all the scales involved. In this case, the mesh resolution must be smaller than the Kolmogorov length scale and the number of grid points is of the order of $Re^{\frac{9}{4}}$. Despite of the accuracy, DNS becomes unfeasible for large domains and/or high Reynolds numbers because of the high computational costs. Reynolds-averaged Navier-Stokes (RANS) methods, on the other hand, solve for the mean quantities of the large scales and all the turbulence scales are modelled. Intermediate to DNS and RANS, Large Eddy Simulations (LES) solve for the large scales of turbulence and only the small scales are modelled. Detailed description of these methods can be found in Versteeg and Malalasekera, 1995; Pope, 2000.

2.4 Chemical Reactions

The chemical source term in Eq. (2.8) depends on the reactions that occur in the system. The elementary chemical reactions are equations as

$$\sum_{\alpha=1}^{N_\alpha} \nu'_{\alpha\beta} M_\alpha \rightleftharpoons \sum_{\alpha=1}^{N_\alpha} \nu''_{\alpha\beta} M_\alpha \tag{2.10}$$

$\beta \in \{1, ..., N_R\}$ with N_R being the number of reactions and M_α is the α-th species. $\nu_{\alpha\beta}{}'$ and $\nu_{\alpha\beta}{}''$ denote the stoichiometric coefficients for species α as reactant and product, respectively.

The mass reaction rate for the α-th species can be expressed as

$$\omega_\alpha = M_\alpha \sum_{\beta=1}^{N_R} (\nu''_{\alpha\beta} - \nu'_{\alpha\beta}) \left[k_f \prod_{j=1}^{N_\alpha} [X_j]^{\nu''_{j\beta}} - k_b \prod_{j=1}^{N_\alpha} [X_j]^{\nu'_{j\beta}} \right] \tag{2.11}$$

where k_f is the forward rate of reaction and k_b the backward rate. The reaction rate coefficients cam be expressed by the empirical Arrhenius law:

$$k_f = A_R T^b \exp\left(\frac{E_R}{RT}\right) \tag{2.12}$$

where the pre-exponential reaction rate constant A_R, the temperature exponent b

and the activation energy E_R are empirical coefficients associated with each reaction, and they are prescribed by the chemical mechanism. The units of the reaction rate coefficient depends on the global order of reaction.

The rate coefficient for backward reactions, k_b, are calculated from the rate coefficient for forward reactions through the equilibrium constant, $K_{C,R}$, by

$$k_b = \frac{k_f}{K_{C,R}} \tag{2.13}$$

The ratio between the turbulent time scale, τ_t, and the chemical time scale, τ_c, is the non-dimensional Damköhler number. The Da indicates the relation between the mechanical timescale and the chemistry which affects directly the combustion models

$$Da = \frac{\tau_t}{\tau_c}. \tag{2.14}$$

In the present work, the combustion of kerosene and n-heptane droplets is investigated. Detailed hydrocarbon mechanisms are composed of hundreds of chemical reactions and the costs of using complete mechanisms would make the computational simulations unfeasible. Therefore, reduced chemical mechanisms are used in order to represent the main reactions involved. The mechanisms used in the simulations are presented in Appendix A.

2.5 Two-phase Flows Modelling

In this section, a review of two-phase flows and combustion models is presented. Two-phase flows require more complex modelling than single-phase flows because of the existence of discontinuities of fluid properties, velocity and pressure jumps across the interfaces. Furthermore, the interfaces can be moving, deforming and breaking.

Eulerian or Lagrangian approaches can be used to model two-phase flows. Eulerian approaches observe the evolution of the fluid motion from a fixed reference frame. Lagrangian approaches look at the fluid motion following an individual fluid

parcel as it moves through space in time. A fully Eulerian approach is usually assumed when studying primary atomisation and tracking the interfaces between the phases. The most common approach involves an Eulerian formulation for the continuous phase, a discrete Lagrangian formulation to track representative droplet or liquid groups through the flow and terms in both formulations to treat interface exchanges. For the dispersed flow treated in the Lagrangian formulation, there can be two main ways of modelling: Deterministic Separated Flow (DSF) and Stochastic Separated Flow (SSF) approaches (Faeth, 1996). In the DSF formulation, droplet motion is limited to deterministic trajectories prescribed by their initial conditions and mean gas properties. This is a simplified approach and generally not very accurate. The SSF formulation considers droplet and small scale turbulence interactions and has been used in the most recent studies because it is more general and better represents realistic problems. In the present work an Eulerian approach is used in a Direct Numerical Simulations (DNS) context where the turbulence scales are fully resolved. In this section, the resolution of the governing equations is discussed and the different approaches applied are presented.

A reacting flow is governed by the transport equations of the mass, momentum, species and energy previously described in Equations (2.1), (2.2), (2.4) and (2.7). Considering the solution of the governing equations for two-phase flows, apart from the resolution in terms of mesh size and time step, there are two commonly used concepts: one-fluid and two-fluid formulations. In the one-fluid formulation one set of governing equations for the variables (velocities and scalars) is valid in the entire flow field including the interface. The two-fluid formulation uses a set of equations for each phase in the flow field and source and sink terms appear to couple the phases. A phase indicator is normally used in both formulations to indicate interfaces and phases.

In this section, an overview of the one and two-fluid formulations as well as the interface tracking methods, jump conditions and combustion modelling are presented; the modelling of evaporation is not described here as it is presented in detail in Chapter 4.

2.5.1 One-fluid and Two-fluid Formulations

In the one-fluid formulation the governing equations presented in the previous section are solved considering the mixture as a whole. The differences in the fluid properties and surface tension are explicitly accounted for using a phase indicator ($\theta_k = 1$ in phase k and $\theta_k = 0$ otherwise). Smoothing of the properties across the interface may be necessary because of the steep gradients (jumps) at the interface. It is the simplest approach because of the reduced number of equations.

In the two-fluid formulation, the two phases are separated by thin and massless interfaces and the two sets of equations are coupled by sink and sources terms. This approach is more complex than the one-fluid formulation as it also needs equations to define these terms. However, it can predict more detailed changes and phase interactions than the two-fluid formulation (Ishii and Hibiki, 2006).

The continuity equation, in the two-fluid formulation context, can be rewritten as

$$\frac{\partial \rho_k}{\partial t} + \frac{\partial \rho_k u_{k,i}}{\partial x_i} = \rho_k \Pi_k \tag{2.15}$$

where Π_k is the volumetric source/sink rate of phase k.

The Navier-Stokes equation considering the effect of surface tension is

$$\frac{\partial \rho_k u_{k,k}}{\partial t} + \frac{\partial \rho_k u_{k,i} u_{k,k}}{\partial x_i} = \frac{\partial}{\partial x_i}\left(\mu_k \frac{\partial u_{k,k}}{\partial x_i}\right) - \frac{\partial p}{\partial x_k} - \sigma \kappa \delta(d) + S_k \tag{2.16}$$

where $u_{a,b}$ is the velocity in phase a and direction b, σ is the surface tension in the liquid, δ is the Dirac delta function, d is the normal distance to the interface, κ is the interfacial curvature and S_k is the sum of the external forces acting on phase k.

Including the phase indicator, the species conservation equation (Mortensen and Bilger, 2009) becomes

$$\frac{\partial \theta_k \rho_k Y_{k,\alpha}}{\partial t} + \frac{\partial \theta_k \rho_k Y_{k,\alpha}(u_{k,i} + V_{k,\alpha,i})}{\partial x_i} = \rho_k Y_{k,\alpha}(\Pi_k + \hat{V}_{k,\alpha}) + \theta_k \rho_k W_{k,\alpha} \tag{2.17}$$

where $W_{k,\alpha}$ is the rate of production of species α and $\hat{V}_{k,\alpha}$ is the volumetric diffusion

velocity across the interface given by

$$\hat{V}_{k,\alpha} = V_{k,\alpha,i}\frac{\partial \theta_k}{\partial x_i} \tag{2.18}$$

The component of the mass diffusion velocity, $V_{k,\alpha,i}$, for cases where Fickian diffusion can be assumed, is given by

$$V_{k,\alpha,i} = -\frac{D_{k,\alpha}}{Y_{k,\alpha}}\frac{\partial Y_{k,\alpha}}{\partial x_i} \tag{2.19}$$

In order to guarantee mass conservation at the interface, in a two-phase flow,

$$\sum_{k=1}^{2} \rho_k \Pi_k = 0, \qquad \sum_{k=1}^{2} \rho_k Y_{k,\alpha}(\Pi_k + \hat{V}_{k,\alpha}) = 0 \tag{2.20}$$

The energy conservation, similar to the species conservation, is

$$\frac{\partial \theta_k \rho_k h_k}{\partial t} + \frac{\partial \theta_k \rho_k u_{k,i} h_k}{\partial x_i} = \frac{\partial p}{\partial t} + \frac{\partial}{\partial x_i}\left(\theta_k D_{k,h}\frac{\partial h_k}{\partial x_i}\right) + S_{k,h}, \tag{2.21}$$

satisfying

$$\sum_{k=1}^{2} S_{k,h} = 0. \tag{2.22}$$

2.5.1.1 Source Terms

In the two-fluid formulation, source terms appear in the equations of species and energy. The influx heat per volume is defined as

$$S_{k,h} = \frac{1}{v}\int_I k\frac{\partial T}{\partial x_i}\mathrm{d}S \tag{2.23}$$

where v is the volume of the cell, and the integral is over the interface surface in the cell. The evaporation rate, which is a source term in the fuel vapour equation, is calculated at the interface as

$$\rho_k Y_{k,\alpha}(\Pi_k + \hat{V}_{k,\alpha}) = \frac{S_{k,h}}{h_{fg}} \tag{2.24}$$

where h_{fg} is the liquid enthalpy of evaporation per mass of fuel and is a function of temperature.

2.5.2 Interface Tracking Methods

Interface tracking and reconstruction can be performed by explicit (front-tracking) or implicit (front-capturing) approaches. Front-tracking methods are based on a Lagrangian tracking of massless marker particles linked to the interface and its motion (Unverdy and Tryggvason, 1992) as shown in Fig. 2.5. The local velocities are used to advect these particles. The resolution of the interface is strongly dependent on the distance between the particles and this is the main limitation of the method. As the interfaces move, the particles do not keep their spacing throughout the calculation. Then, addition or deletion of the particles must be done dynamically. This limitation restricts the use of the method in complex geometries or interface motions where the implementation can become relatively complex and expensive.

Common implicit numerical methods for interface tracking are Moving Grids (Cristini et al., 2001), Volume of Fluids (Gueyffier et al., 1999) and Level Sets (Osher and Sethian, 1988), (Sussman et al., 1994). In Moving Grids methods, the interface is represented by grid nodes that move by Lagrangian transport (see Fig. 2.5). The interface is represented by moving grid points that follow the interface motion. This can result in large grid deformation and re-griding may be necessary. It is mostly used for small interface deformations and can become very complex in other cases.

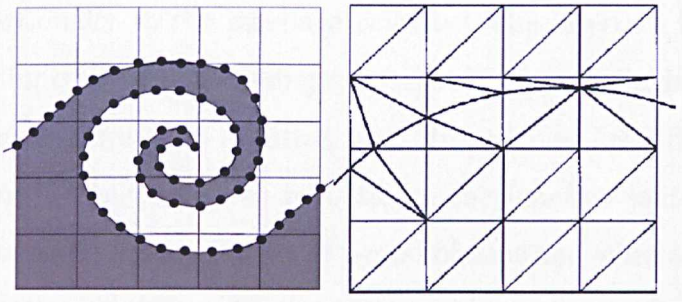

Figure 2.5: Interface representation by the Marker Particles (left) and Moving Grid (right) methods (Scardovelli and Zaleski, 1999).

In the Volume of Fluid method (VOF), the interface is represented on a fixed grid by a marker function that indicates the fractional volume of one of the fluids in each cell of the domain. The location of the interface is not explicitly defined and geometric reconstruction has to be performed. Some reconstruction procedures have been advanced from Simple Linear Reconstruction to Piecewise Linear Interface Construction and parabolic approximations (Renardy and Renardy, 2002). These procedures have improved the computation of the interface curvature but normal movement is still not straightforward and the procedures need elaborated implementations. The main advantage of the VOF method is that it is inherently volume and mass conserving. Figure 2.6 shows an interface being represented by a the marker function of VOF and of the Level Set method.

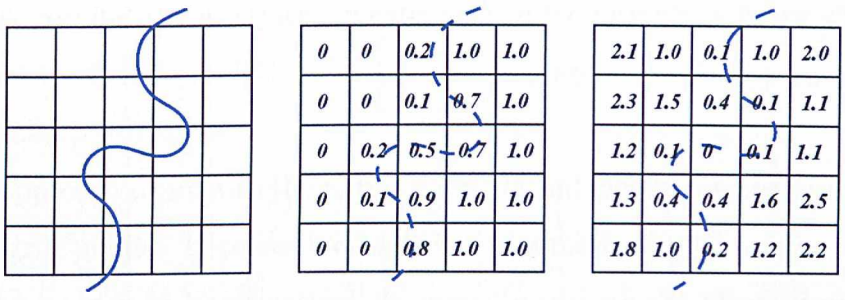

Figure 2.6: Interface represented by its original shape (left), VOF (middle) and Level Set (right) methods in a cartesian grid.

The Level Set method tracks interfaces by choosing a smooth function, generally defined as the signed minimum distance of the point to an interface, and advancing it in time proportionally to the interface velocity. The interface is defined as the zero level of the function and to distinguish between the two fluids, one side of the interface has the distance with negative sign. In order to keep the level set as a distance function, it is necessary to reiniatialise the function periodically because the function becomes irregular after some period of time and when surfaces merge or breakup. The interface is then easily reconstructed by the iso-surface of the level set function and normal movements are handled automatically. However, the method is not inherently volume or mass conserving.

Some recent works combine VOF and Level set methods to overcome the prob-

lems of both methods (Coyajee et al., 2004). The reconstruction of the interface is not needed because the information is given by the level set funtion and, on the other hand, the use of VOF guarantees mass conservation. In these works, the Level Set methodology is used for the representation of the interfaces while VOF is used for volume preserving advection. The Level Set method is used in the present work in a new simple mass conserving approach described in detail in Section 3.2.4.

2.5.3 Jump Conditions

Independently of the interface tracking method chosen, an appropriate phase transition must be applied across interfaces in order to account for jumps in velocities, pressure and fluid properties. There are two approaches commonly used: to smooth the jumps around the interface, smearing out discountinuities (normally associated with the one-fluid formulation) or to take into account effective jump conditions allowing sharp interfaces.

The approach to smooth the jumps is simple and distributes the jump over neighbouring grid points. It consists of defining a number of cells around the interface where the jump is to be smoothed. In order to smooth the physical properties, for example, it is common to use a smoothed Heaviside step function, H. Sussman et al., 1994, proposed

$$H = \begin{cases} 0, & \text{if } \phi < -\zeta \\ 0.5 + 0.5\frac{\phi}{\zeta} + \dfrac{sin(\frac{\pi\phi}{\zeta})}{2\pi}, & \text{if } |\phi| \leq \zeta \\ 1, & \text{if } \phi > \zeta \end{cases} \tag{2.25}$$

where ζ is the interface thickness. A field, f, is calculated then by

$$f = f_1 + (f_2 - f_1)H. \tag{2.26}$$

Some other methods, such as the Continuum Surface models, also applies the idea of smoothing a discontinuity. The Ghost Fluid method (Fedkiw et al., 1999), however, defines an extension of the field of each phase without smearing across the

interfaces (see next subsection).

2.5.3.1 Surface Tension Models

Intermolecular forces such as Van der Waals forces that play an important role in interface physics are modelled by their most important effect which is capillarity or a surface tension force. The surface tension term in the Navier-Stokes equation is a singular term and might create numerical instabilities and noise as well as result in poor accuracy of capillary effects. Different models have been proposed for surface tension effects in Eulerian approaches.

Introduced by Brackbill et al., 1992, the Continuum Surface Force model (CSF) treats the surface tension as a continuous and three-dimensional effect across an interface rather than as a boundary condition at the interface. This model avoids interface reconstruction and proved to be simple and robust. The CSF defines the surface tension force, F_{st}, as a volume force smoothed in a transition region defined as interface thickness, ζ. Defining a smooth characteristic function, $\tilde{c}$, of a variable, c, that changes discontinuously at the interface such as density, the force is

$$F_{st} = \sigma\kappa\frac{\nabla\tilde{c}}{c} \tag{2.27}$$

A 'colour' function is defined as follows.

$$\tilde{c} = \begin{cases} c_1, & \text{if } \phi < -\zeta \\ (c_1 + c_2)/2, & \text{if } |\phi| \leq \zeta \\ c_2, & \text{if } \phi > \zeta \end{cases} \tag{2.28}$$

with

$$\lim_{\zeta \to 0} \tilde{c} = c \tag{2.29}$$

As can be seen from Eq. (2.27), the determination of the curvature, κ, is essential for the CSF-based models. Errors in the calculation of the curvature may cause the surface tension force to be inaccurate, therefore, it is essential to evaluate these errors in order to quantify the uncertainties. The main problem caused by surface tension calculation errors is the generation of spurious currents. These cur-

rents are unrealistic velocities generated in the vicinity of the interface due to the implementation of surface tension models.

The Continuum Surface Stress (CSS) approach (Scardovelli and Zaleski, 1999) follows the concept of CSF, however, avoiding dealing explicitly with the curvature. The curvature is implicitly calculated from the smoothed colour function, $\tilde{c}$. Parasitic currents, the main issue caused by the surface tension models' implementation, are still generated and the smoothing around the interface reduces accuracy of the methods.

Shirani et al., 2005, have proposed a new method based on the interface location. First, the intersection of an interface with the interface cell faces are determined. The area of a cell face, which is in contact with the heavier fluid, is normalised with the cell face area to obtain a factor H_{st}. Then, the two values of H_{st} obtained from the cells on both sides of each internal cell face are averaged determining the final value of H_{st}. Finally, the surface tension force used in the momentum equation is multiplied by H_{st}. The surface tension force defined for each interface cell is then obtained from

$$F_{st} = H_{st}\sigma\kappa\vec{n}\delta \tag{2.30}$$

where δ is the Dirac delta function.

The Ghost Fluid method (GFM) (Fedkiw et al., 1999) defines an extension of the field of each phase with no smearing in the quantity across the interfaces and applying the known appropriate jump conditions such as surface tension ($J_p = \sigma\kappa$). The spatial derivatives are then calculated using the values extrapolated from the other phase plus the appropriate jump condition. This approach offers more accurate discretisation of discontinuities and spurious currents are reduced when the GFM is used. The GFM is used in the present work and described in detail in Chapter 3.

2.5.4 Compressibility

Considering the interaction of acoustics and combustion adds another level of complexity to reacting flows. The control of thermoacoustic instabilities is crucial, for example, for the safe operation of rocket motors and modern gas turbines. More-

over, the design and improvement of high-speed fuel injection systems of Diesel- and Otto-engines is a challenging field of research where the operating conditions contain exceptional high pressure differences (around 100 bar) which result in maximum flow velocities up to 500 m/s (Schmidt et al., 2007). The arising pressure drop typically leads to acoustic and hydrodynamic cavitation.

The simulation of wave dynamics requires a fully compressible treatment of the equations of motion. The thermodynamic properties of liquid and vapour must be expressed by appropriate equations of state. There are few examples in the literature of acoustic two-phase flow and high order schemes used in compressible flows are not suitable for two-phase flow simulations. Some works use a Riemann solver with a stiff equation of state for the liquid, allowing the resolution of wave speeds in the liquid phase. In this case, the Riemann solver can be used to treat the interface as a discontinuity with appropriate Rankine-Hugoniot jump conditions. Examples can be found in Castro and Toro, 2006, and Andrianov and Warnecke, 2004. The wave speed is very high, thus, the time steps become very small and the computations very expensive. The compressibility effect becomes siginificant in cases of liquid explosion. In this work, compressibility effects are not considered.

2.5.5 Combustion

Reacting flows are particularly difficult to model and compute because of the non-linear reaction rates combined with the complexity of turbulence modelling. The combustion processes are classified depending on the reactants mixing as non-premixed, premixed or partially premixed. Spray combustion is non-premixed or partially premixed. Although many approaches have been proposed (see Fig. 2.7), the most frequently used for non-premixed or partially premixed combustion modelling are the Flamelet model (Peters, 2000), the CMC model (Klimenko and Bilger, 1999) and PDF-methods (Pope, 1981) .

The Flamelet and the CMC methods are mixture fraction based models. The mixture fraction, f, gives the ratio between the mass of fuel over the total mass of the mixture and it is normalised in order to go from zero (in the oxidizer) to unity

(in the fuel).The mixture fraction follows the balance equation

$$\frac{\partial \rho f}{\partial t} + \frac{\partial \rho u_i f}{\partial x_i} = \frac{\partial}{\partial x_i}\left(\rho D \frac{\partial f}{\partial x_i}\right). \tag{2.31}$$

The scalar dissipation represents the inverse of a diffusion time scale and is a key quantity in premixed and non-premixed systems. In non-premixed systems, the mixing between the fuel and oxidizer is the controlling process of the chemical reactions and the flame. Directly or indirectly, the scalar dissipation appears in most approaches used to model combustion (Veynante and Vervisch, 2002). It is calculated as a function of diffusivity, D, and mixture fraction gradients.

$$N = 2D\left(\frac{\partial f}{\partial x_i}\frac{\partial f}{\partial x_i}\right) \tag{2.32}$$

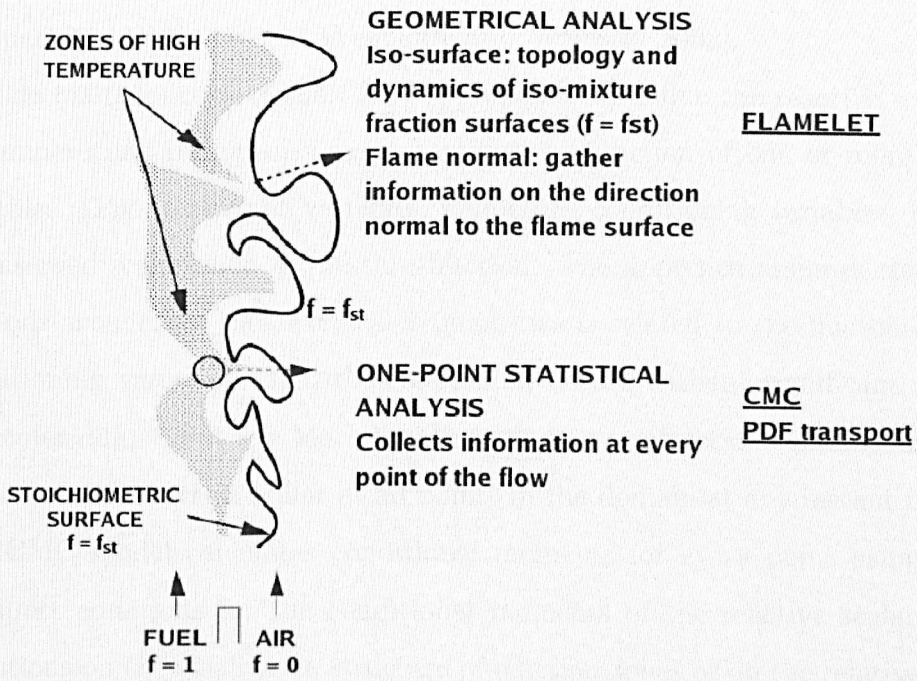

Figure 2.7: Combustion models analysis by (Veynante and Vervisch, 2002).

If the reaction is very fast and the chemical time scale is short compared to the convection-diffusion time scale ($Da \gg 1$), the reaction occurs only in thin layers (smaller than Kolmogorov scale). The Flamelet model is based on the concept of

considering a turbulent flame as a set of thin laminar flames called flamelets. These flamelets are located on the iso-surfaces of stoichiometric mixture fraction, f_{stoic}. Since the mixture fraction can be obtained by the mixture fraction transport equation, the location of the flame is known. The flame is seen as an interface between fuel and oxidizer (non-premixed) or between burnt and unburnt gases (premixed). The structure of the reacting flow is analysed along the direction normal to the flame surface and the density of the flame surface area is used to estimate the burning rate. The flamelet approach to turbulent flames is valid if the thickness of the reaction zone is smaller than the Kolmogorov length scale. In this case, there are no fluctuations of the scalars (species) on the flame surface and it can be regarded as laminar. Thus, the molecular diffusion determines the species transport across the reaction zone. However, the model neglects the influence of spatial variations of the scalar dissipation rate (Bilger, 2000) and does not seem to be valid in the presence of local extinction and re-ignition when significant local variations of scalar dissipation rate are present (Veynante and Vervisch, 2002).

The main concept of the CMC approach is to define the reactive scalars, such as temperature and species mass fractions, as function of one or more important variables. The important variables, defined as conditioning variables, are usually a conserved scalar such as mixture fraction. The approach assumes that the fluctuations around the mean of scalar quantities is related to the fluctuations of the conditioning variables. If turbulent mixing occurs without significant differential molecular diffusion at low Mach number, the mixture fraction contains all the information on the reactive scalar at all points in the domain at any instant in the flow. The CMC model calculates conditional moments for every point using modelled transport equations for the conditional moments of the reactive scalars. No assumptions on the small scale structure of reaction zones or on the relative timescale of chemistry and the turbulence are made. The equations for any level of moments have terms involving higher levels. Thus, unclosed terms appear and need modelling. The correlations between the scalar and the conditioning variable are obtained using a pre-defined shape of a joint probability density function (PDF) which is assumed to be of β-shape for the mixture fraction.

The sub-grid PDFs of mixture-fraction and the scalar rate of dissipation have to be predetermined to compute the evolution of the composition space. Although the joint PDFs can be presumed, such as in the CMC model, a more accurate approach is to solve a transport equation for the joint PDF of the reactive scalars itself or to include velocity field statistics into the PDF. The PDF transport equation is usually solved using a Lagrangian stochastic particle method, where an ensemble of particles represents the joint PDF (Dopazo and O'Brien, 1974; Dopazo, 1975; Pope, 1985). An alternative solution method of the PDF transport equation using an Eulerian framework is based on stochastic Eulerian fields, which evolve according to stochastic partial differential equations equivalent to the joint PDF transport equation (Valiño, 1998; Sabel'nikov and Soulard, 2005). These fields are continuous and differentiable in space and continuous though not differentiable in time. The objective of PDF modelling is avoid the assumptions of the shape of the PDFs. The main advantage is that no modelling is required to compute the source term and the chemical state. On the other hand, the micromixing term is not closed and must be modelled. These methods are accurate but computationally very expensive especially if a large number of reactive scalars is solved.

2.6 Summary

This chapter presented a review on two-phase flows dynamics and modelling. The physics behind liquid reacting sprays are reviewed. The spray structure is described and the processes of primary and secondary atomisation are explained along with the different secondary breakup regimes. The evaporation process of sprays is not presented here in detail as it is described in Chapter 4. The spray combustion regimes are described and Section 2.3 describes the flow field governing equations followed by the chemical reactions in Section 2.4.

Section 2.5 presents an overview on the modelling applied to two-phase flows. It presents aspects of flow field resolution, breakup, combustion and surface tension models. First, the turbulence scales and the RANS, LES and DNS approaches are explained. Then, the one and two-fluid formulations are discussed and the govern-

ing equations are reported in a multi-phase flow context. Moreover, the interface tracking methods are explained and the advantages of each method are described as well as the treatment for jump conditions such as surface tension forces. Finally, comments on compressibility in two-phase flows are presented.

In the present work, DNS is used in order to understand and quantify the effects of the droplets, turbulence and evaporation in gas-phase mixing (Chapter 5). The local effects of the flow field in the evaporation and combustion rates of droplets are also investigated and presented in Chapter 4.

Chapter 3

Numerical Method and Validation

3.1 Introduction

The present chapter describes the numerical approaches used in this work. The implemented model simulates two-phase reacting flows with low Mach number by resolving liquid and gas phases. In the cases run in this work, DNS are performed and all the scales involved in both phases are resolved. The domain resolution and the time step capture the smallest length and time scales. The mesh resolution in all the test cases is refined enough in order to capture the Kolmogorov scales.

In the next section, the solution procedure is presented. The discretisation of the governing equations and the total variation diminishing (TVD) scheme are described. The solution method is then presented with the description of the pressure correction.

The third section focuses on the interface tracking and gives a detailed description of the Level Set and the Ghost Fluid methods. The extension of the interface velocities and the reinitialisation procedure for the level set function are also explained. As the Level Set method is not mass conserving, a new approach is developed to guarantee mass conservation and it is here described followed by the calculation of geometric characteristics (surface and curvature) which used directly the level set function information.

Validation of models is essential to guarantee that the results obtained are valid

and various test cases are performed in order to validate the implemented model. First, the calculation of the curvature and the surface tension model are tested. Then, the errors in the interface surface calculation are also quantified as the surface area is essential for the heat transfer computation. The coupling and interactions between the phases and the mass conservation are also investigated and validated. Finally, the heat transfer process and the reaction zones are evaluated. The main results are presented in details and compared to other models or experimental data.

3.2 Numerical Approach

The governing equations are solved for the liquid and gas phases, as mentioned before. The energy transport equation is solved using a one-fluid formulation. However, the species, velocities and pressure are solved using a two-fluid formulation.

In order to track the interface between the liquid and gas phases, the Level Set method is combined with the Ghost Fluid method to account for pressure jumps in a mass conserving approach. The introduction of interface thickness and the smoothing of fluid properties (density, diffusivity, specific heat, conductivity and surface tension) in variable density flows are avoided because of the two-fluid formulation and the use of the Ghost Fluid method. A detailed description of this implementation is presented in this section.

The model is implemented in the in-house low-Mach number CFD code BOFFIN (Jones et al., 2002). The paralellisation of the code is briefly explained in Appendix C. The code is second order accurate in time (Crank and Nicolson, 1947) and in space away from discontinuities, and first order accurate near them.

In this work, DNS are performed where the turbulent and chemical scales are resolved.

3.2.1 Solution Procedure

The transport equations are solved in the following order: energy, species, velocities and pressure correction. The velocities are calculated using the momentum equations and are updated by the pressure correction. As shown in Fig. 3.1, the code

follows a predictive-corrective procedure with two iterations. The level set function, however, is advanced and reinitialised only once, at the end of each step (end of second iteration). The reinitialisation is then followed by the mass conservation check and correction (when necessary). If a mass correction is applied, the level set function is updated and reinitialised once more.

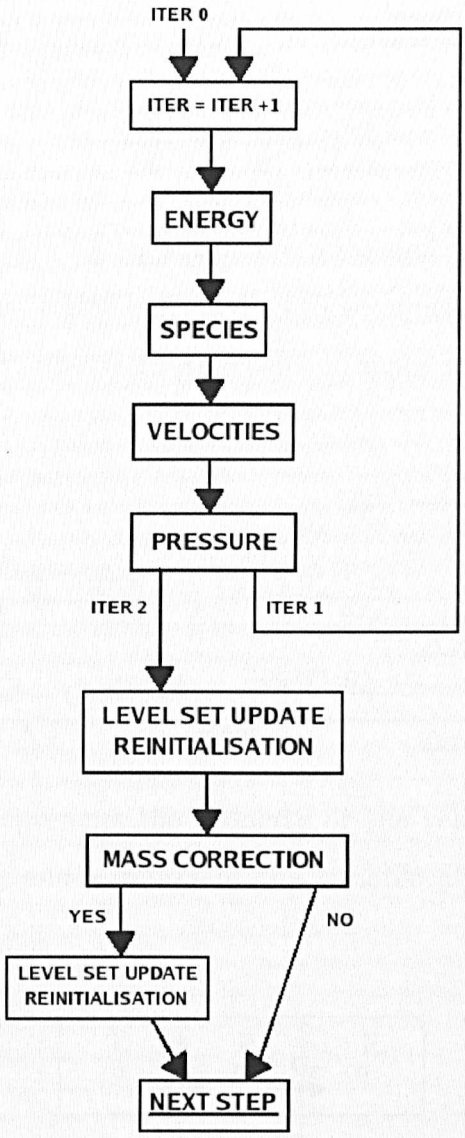

Figure 3.1: Solution procedure chart.

3.2.1.1 Discretised Equations

The general transport equation of a variable Ω can be written as

$$\frac{\partial \rho\Omega}{\partial t} + \frac{\partial \rho\Omega u_i}{\partial x_i} = \frac{\partial}{\partial x_i}\left(\Gamma \frac{\partial \Omega}{\partial x_i}\right) + S \tag{3.1}$$

where Ω can be a scalar (energy or species) or any velocity component, Γ is the diffusivity of Ω and S is the source term. The transient term is given by

$$\frac{\partial \rho\Omega}{\partial t} = \rho\frac{\partial \Omega}{\partial t} + \Omega\frac{\partial \rho}{\partial t} \tag{3.2}$$

For simplicity, all following equations are presented for a one-dimensional case (see Fig. 3.2) but can be easily extended to three-dimensional cases. A transport equation, using a second order accurate scheme in space and Crank-Nicolson scheme in time is discretised as

$$\begin{aligned} \rho_P^* \frac{\Omega_P^{n+1} - \Omega_P^n}{\Delta t} - \Omega_P^{n+1}\frac{G_R - G_L}{\Delta x_i} \\ + \frac{1}{2}\frac{G_R\frac{\Omega_P^{n+1}+\Omega_R^{n+1}}{2} - G_L\frac{\Omega_P^{n+1}+\Omega_L^{n+1}}{2}}{\Delta x_i} - \frac{1}{2}\frac{\frac{\Gamma_R^*+\Gamma_P^*}{2}\frac{\Omega_R^{n+1}-\Omega_P^{n+1}}{\Delta x_R} - \frac{\Gamma_L^*+\Gamma_P^*}{2}\frac{\Omega_P^{n+1}-\Omega_L^{n+1}}{\Delta x_L}}{\Delta x_i} = \\ -\frac{1}{2}\frac{G_R\frac{\Omega_P^{n}+\Omega_R^{n}}{2} - G_L\frac{\Omega_P^{n}+\Omega_L^{n}}{2}}{\Delta x_i} + \frac{1}{2}\frac{\frac{\Gamma_R^*+\Gamma_P^*}{2}\frac{\Omega_R^{n}-\Omega_P^{n}}{\Delta x_R} - \frac{\Gamma_L^*+\Gamma_P^*}{2}\frac{\Omega_P^{n}-\Omega_L^{n}}{\Delta x_L}}{\Delta x_i} + S_P \end{aligned} \tag{3.3}$$

where the index * represents the property or the velocity at the intermediate stage $(n + \frac{1}{2})$ and $_P$, $_L$ and $_R$ represent the variable at the points P, L and R, respectively.

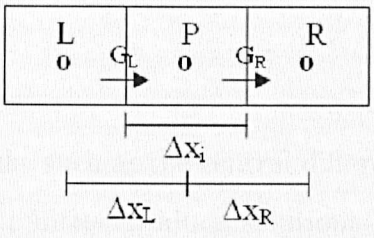

Figure 3.2: Discretisation scheme in a one-dimensional case.

Away from the interface, the fluxes G_R and G_L are calculated at the faces of the

cells by

$$G_R = \frac{\rho_R^* + \rho_P^*}{2} \frac{u_R^* + u_P^*}{2} \tag{3.4}$$

$$G_L = \frac{\rho_L^* + \rho_P^*}{2} \frac{u_L^* + u_P^*}{2} \tag{3.5}$$

At the interface cells the fluxes are calculated using the Ghost Fluid method as indicated in Section 3.2.3.

Collecting the terms from Equations (3.3), (3.4) and (3.5), the transport equations can be rewritten in a matrix form as

$$A_P \Omega_P^{n+1} = A_L \Omega_L^{n+1} + A_R \Omega_R^{n+1} + B_P \tag{3.6}$$

with

$$A_L = \frac{G_L}{4\Delta x_i} + \frac{\Gamma_L^* + \Gamma_P^*}{4\Delta x_L \Delta x_i}, \tag{3.7}$$

$$A_R = -\frac{G_R}{4\Delta x_i} + \frac{\Gamma_R^* + \Gamma_P^*}{4\Delta x_R \Delta x_i} \tag{3.8}$$

and

$$A_P = \frac{\rho_P^*}{\Delta t} - \frac{G_R - G_L}{\Delta x_i} + \frac{G_R - G_L}{4\Delta x_i} + \frac{\Gamma_R^* + \Gamma_P^*}{4\Delta x_R \Delta x_i} + \frac{\Gamma_L^* + \Gamma_P^*}{4\Delta x_L \Delta x_i} \tag{3.9}$$

so

$$A_P = \frac{\rho_P^*}{\Delta t} - \frac{G_R - G_L}{\Delta x_i} + A_L + A_R. \tag{3.10}$$

$$B_P = \frac{\rho_P^* \Omega_P^n}{\Delta t} - \frac{1}{2} \frac{G_R \frac{\Omega_P^n + \Omega_R^n}{2} - G_L \frac{\Omega_P^n + \Omega_L^n}{2}}{\Delta x_i} + \frac{1}{2} \frac{\frac{\Gamma_R^* + \Gamma_P^*}{2} \frac{\Omega_R^n - \Omega_P^n}{\Delta x_R} - \frac{\Gamma_L^* + \Gamma_P^*}{2} \frac{\Omega_P^n - \Omega_L^n}{\Delta x_L}}{\Delta x_i} + S_P \tag{3.11}$$

3.2.1.2 TVD Scheme

Linear discretisation methods, such as the central difference scheme, in the presence of rapid changes or discontinuities produce solutions with oscillations or wiggles (Godunov, 1959). In order to overcome this problem, some non-linear schemes have been proposed (Ferziger and Peric, 2002). The total variation diminishing (TVD) schemes, such as the one used here, make use of limiters to provide non-oscillatory

solutions. The concept is to limit the flux of the conserved scalar to a level that will not produce a local maximum or minimum of the profile of the scalar. In this work, the Sweby Upper Bound (SUB) limiter is used to the convective terms in the scalars' transport equations. Keays, 2006, showed that this limiter maintains sharpness and integrity of a scalar distribution with small numerical diffusion. The TVD scheme is applied only for the scalars (species and enthalpy) while a central difference scheme is used for the velocities.

The limiter is applied to the convective flux term and is given by

$$\frac{\partial f(x,t)}{\partial x} = \frac{\hat{f}^n_{i+1/2} - \hat{f}^n_{i-1/2}}{\Delta x_i} \tag{3.12}$$

Thus, the scalar at the intermediate stage is

$$\hat{f}^n_{i+1/2} = \hat{f}_{i+1/2,l} + \Psi_{SUB}.(\hat{f}^n_{i+1/2,h} - \hat{f}^n_{i+1/2,l}) \tag{3.13}$$

where the subscripts $_h$ and $_l$ indicate higher and lower order fluxes here. The idea is to limit the amount of a high order flux (central difference - oscillatory) which is added to a basic first order flux (diffusive) to ensure that the scheme remains high order. A ratio of derivatives is calculated as

$$r = \frac{\frac{\phi_i - \phi_{i-1}}{\Delta x_R}}{\frac{\phi_{i+1} - \phi_i}{\Delta x_L}} \tag{3.14}$$

And the SUB limiter, using the ratio, r, is defined by

$$\Psi_{SUB} = \max(\min(2r, 2), 0) \tag{3.15}$$

3.2.1.3 Pressure Correction

The solution of the Navier-Stokes equations is complicated because of the lack of an independent equation for the pressure and the pressure gradient is needed for the velocity calculation. In compressible flows, the continuity equation can be used to define the density and an equation of state proposes an expression for the pressure. This approach is not feasible for incompressible or low Mach number flows (Ferziger

and Peric, 2002) as used in the present work. In order to solve this problem, a pressure field can be constructed where the absolute value of pressure is not important but the gradient of pressure. In the present work, the continuity equation is used in order to calculate this pressure field in combination with the momentum equations.

The algorithm used in the code is of a predictive-corrective SIMPLE-type. Concerning the velocity calculations, the sequence of calculations is described as follows.

A starting estimation for the velocity u^{n+1} and the pressure p^{n+1} at the new time t^{n+1} is made using the latest solution of velocity u^n and pressure p^n (or with the initial conditions in the first step). Thus, the momentum equations are solved, solving each component of velocity $\breve{u}_k^{n+1}$ separately.

$$\frac{\partial \rho \breve{u}_k}{\partial t} + \frac{\partial \rho \breve{u}_k u_i}{\partial x_i} = F_{ext,k} - \frac{\partial p}{\partial x_k} + \frac{\partial \sigma_{ik}}{\partial x_i} \tag{3.16}$$

The pressure correction, δp^{n+1}, equation is

$$-\frac{\partial \rho}{\partial t} = \frac{\partial \rho \breve{u}_i}{\partial x_i} + \frac{\partial}{\partial x_i}\left(\rho\beta \frac{\partial(\delta p)}{\partial x_i}\right) \tag{3.17}$$

where $\beta = \frac{1}{2}\frac{\Delta t}{\rho \Delta x_i}$. The flow is incompressible, however, because of evaporation and temperature variations, the term $\frac{\partial \rho}{\partial t}$ is not zero.

Mass conservation is enforced and corrections to the estimated value can then be found for pressure and velocity. The values for pressure p^{n+1} and velocity u_k^{n+1} are updated by adding the correction to the estimated values,

$$p^{n+1} = p^n + \delta p^{n+1} \tag{3.18}$$

and

$$u^{n+1} = \breve{u}^{n+1} - \beta \delta p^{n+1}. \tag{3.19}$$

Two iterations are performed. In the second iteration, the updated values resulting from the first iteration are used used as initial estimations. Figure 3.1 shows the iterative scheme.

3.2.1.4 Thermophysical Properties and Chemistry

The liquid phase is assumed to be at constant temperature and below the critical point, therefore the properties are fixed. In the gas phase, the properties of each component vary with temperature and pressure, and the density is obtained according to the ideal gas equation of state. The local properties are calculated as function of the local composition (mixture of air and fuel vapour) and temperature using standard kinetic theory and Wilke's rule for viscosity (Wilke, 1950). At the interface cells where liquid and gas are present, the properties of the mixture are weighted with the volume fractions.

The combustion of kerosene and *n*-heptane droplets is investigated and the chemical mechanisms used in the simulations are presented in Appendix A. An implicit scheme with Newton linearisation is employed for the integration of the stiff chemical source term.

The chemistry of kerosene is approximated by a 4-step and 7-species (CO, CO_2, H_2, N_2, H_2O, O_2 and $C_{12}H_{23}$) mechanism for hydrocarbon combustion (Jones and Lindstedt, 1988).

The reduced mechanism used for *n*-heptane was proposed by Liu et al., 2004, and uses 21 species (OH, HO_2, H, CO, CO_2, H_2, H_2O_2, H_2O, CH_2O, O_2, *n*-C_7H_{16}, C_3H_6, C_2H_4, C_6H_{12}, CH_3, C_4H_8, C_3H_4, C_2H_2, CH_4, $C_7H_{15}O_2$ and OC_7H_{13}) and 18 steps.

3.2.2 Level Set Method

The Level Set method is a numerical approach for computing the motion of two-phase flows by implicitly capturing the interface (Sussman et al., 1994). It is an Eulerian formulation of the interface evolution. The interface between the two phases (liquid and gas in the present work) is identified as the zero level set of a field variable of a smooth function, ϕ. The use of a smooth function avoids steep gradients and numerical instabilities. The function is defined at every point of the domain and is commonly chosen to be the signed minimum distance from the point to the interface. In this work, the function sign is defined as positive in the gas phase and negative

in the liquid phase.

The level set function is time and space dependent. Assuming that the initial interface position is known, the motion of the interface is defined by the advection equation

$$\frac{\partial \phi}{\partial t} + u_{iI} \frac{\partial \phi}{\partial x_i} = 0. \tag{3.20}$$

The variable u_{iI} is the interface velocity and it is commonly defined only at the interface or in a band around the interface. However, stability, accuracy and better sub-grid resolution can be achieved by extrapolating the interface velocities in the entire field as described later in this section. In the present work, Eq. (3.20) is solved explicitly in the entire domain with extended interface velocities. Integration in time is achieved by using a second-order fractional time step method (Yanenko, 1971). The level set gradient is calculated using an upwind finite difference scheme.

The interface velocity, u_{iI}, is decomposed into convective and phase change velocities (Selvam et al., 2006). It is calculated following

$$u_{iI} = u_c - \frac{k}{\rho_l h_{fg}} \frac{\partial T}{\partial x_i}. \tag{3.21}$$

The second term on the right side represents the interface velocity due to phase change, in this evaporation. The temperature gradient is approximated by a fourth-order central difference scheme. The interface convective velocity, u_c, must satisfy the Rankine-Hugoniot conditions and therefore given by

$$u_c = \frac{\rho_l u_l - \rho_g u_g}{\rho_l - \rho_g}. \tag{3.22}$$

The density of the liquid, ρ_l, is commonly much higher than the density of the gas, ρ_g, even if the velocity of the liquid phase, u_l, is lower than the gas phase velocity, u_g,the interface convective velocity is very close to the local liquid phase velocity ($u_c \simeq u_l$). The velocity of the interface is defined at each point of the interface taking into account the local densities and velocities of liquid and gas phases.

Once the level set function is defined as the signed minimum distance, it is important to maintain ϕ as a distance function so the interface can be reconstructed.

Solving Eq. (3.20) can make the function irregular after some time steps and especially when surface merge or breakup occur. Therefore, even with extension of the interface velocities, it is necessary to reinitialise the function ϕ periodically. The following subsections describe the interface velocity extension and reinitialisation procedures.

3.2.2.1 Interface Velocity Extension

Advancing the level set function can be improved by extending the interface velocity to every point in the domain. There are problems in which the speed of the interface changes rapidly or discontinuously as the front moves through the domain and the exact location of the interface determines the speed. In these cases, constructing a velocity from the position of the interface itself rather than from less accurate grid velocities improves subgrid resolution (Adalsteinsson and Sethian, 1999). In addition, the extension of the velocities helps maintain an accurate level set representation and reduces the number of iterations in the reinitialisation procedure, making this procedure more efficient and less time demanding.

The extension velocity is defined so that the level set function which is initialised with the signed minimum distance from the interface to the center of the cell, evolves accurately in the entire domain as the front moves. However, it is noted that some correction is still necessary and the reinitialisation procedure cannot be avoided in order to guarantee that the minimum distance is well preserved. The advantages of the velocity extension algorithm is that it both reduces the need of reinitialisation (number of timesteps in this procedure), which can cause some distortion on the interface, and avoids the bunching and stretching of neighbouring level set lines. The perturbations of the level set lines close to the interface lead to mass conservation issues so the extension of the velocities also improve mass conservation.

In this work, the extension is performed following the idea that each cell of the domain takes the interface velocity of the closest interface point. The main issue is to design an efficient algorithm to track the closest interface point for each cell. If not efficient, the procedure might increase significantly the computational cost.

In order to optimise the algorithm, the value of the level set function at the cell

is used to define a region of the domain where the closest points are tracked, as shown by the yellow region in Fig. 3.3. The region is defined with a width of $4\Delta x$. Only the cells inside the region are tracked, making the algorithm more efficient. Then, for each interface point found in this region, the distance from the interface to the cell center is verified and the velocity of the closest one is set to the cell.

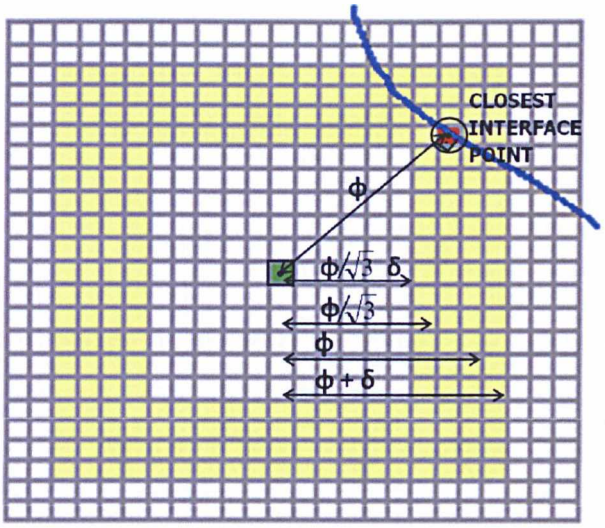

Figure 3.3: Extension of the interface velocity scheme.

Even though the extension of the velocities reduces the computational time of the reinitialisation procedure, it increases the stability and improves accuracy, the method increases the total time of the whole Level Set method procedure. Therefore, in cases where the interface is not moving outside a certain band or region, the extension of the velocities can be done only in the neighbourhood of this region and not necessarily in the entire domain.

3.2.2.2 Reinitialisation Procedure

The reinitialisation procedure (Sussman et al., 1994) propagates the information from the interface to the rest of the domain in the direction normal to the interface. Furthermore, reinitialisation must conserve the value of the level set as the signed minimum distance at all grid points.

The reinitialisation is achieved by recalculating the level set function in the entire

domain following

$$\frac{\partial \phi}{\partial \tau} + sign(\phi)(|\nabla \phi| - 1) = 0. \tag{3.23}$$

The sign function $sign(\phi)$ can be obtained in different ways. However, it must have a zero value at the cells adjacent to the interface and give the sign of the level set away from the interface, guaranteeing that the values at the grid points adjacent to the interface are preserved and used as boundary conditions. This procedure ensures that $|\nabla \phi| = 1$ away from the interface. In this work, the sign function is obtained as proposed by (Sussman et al., 1994)

$$sign(\phi) = \frac{\phi}{\sqrt{\phi^2 + \Delta x^2}}. \tag{3.24}$$

An alternative formulation is proposed by Peng et al., 1999, and postulates that

$$sign(\phi) = \frac{\phi}{\sqrt{\phi^2 + |\nabla \phi|^2 + \Delta x^2}} \tag{3.25}$$

is a better choice for the sign function. No significant difference in the results of the circular test case is found so Eq. (3.25) is chosen.

The absolute partial derivatives of the level set function gradient are approximated by a fifth-order weighted essentially nonoscillatory (WENO) scheme (Jiang and Peng, 2000) as described in Appendix B. The smoothing indicators proposed by Jiang and Peng, 2007, are also tested but no significant improvement in the number of iterations or the accuracy of the reinitialisation procedure is observed.

The integration in time is achieved by a third-order TVD Runge-Kutta scheme (Shu, 1988) with a fictitious time step equal to $\tau = 0.5\Delta x$ and a defined maximum residual in a band close to the interface. Defining $\frac{\partial \phi}{\partial \tau} = L(\phi)$, the method solves for ϕ according to the following three steps:

$$\phi^{(1)} = \phi^{(0)} + \Delta \tau L(\phi^{(0)}),$$

$$\phi^{(2)} = \phi^{(1)} + \frac{\Delta \tau}{4}(-3L(\phi^{(0)}) + L(\phi^{(1)})),$$

$$\phi^{(3)} = \phi^{(2)} + \frac{\Delta \tau}{12}(-L(\phi^{(0)}) - L(\phi^{(1)}) + 8L(\phi^{(2)})).$$

3.2.3 Ghost Fluid Method

In multiphase flows, the discontinuities in the properties of the fluids and also in pressure occur across the interfaces and must be taken into account most accurately. The Ghost Fluid method was developed in order to treat these jumps in Eulerian schemes maintaining a Heaviside profile of the variable of interest with no numerical smearing (Fedkiw et al., 1999). The main concept behind the method is to create ghost cells (or nodes) in each phase and compute the appropriate properties and scalars for the ghost cells depending on the phase which is being evaluated. These values are then used to calculate derivatives. Jumps conditions, which must be known or defined, are added appropriately to the derivatives.

The classical formulation of a second order central difference derivative for pressure, for example, is

$$\frac{\partial p}{\partial x} = \frac{p_{i+1} - p_{i-1}}{x_{i+1} - x_{i-1}} \tag{3.26}$$

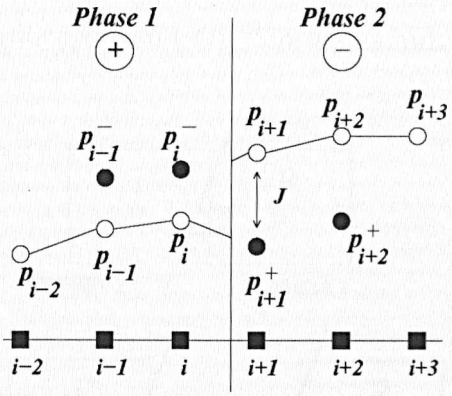

Figure 3.4: Ghost Fluid method - scheme for ghost cells of variable p.

In the Ghost Fluid method, using the notation of Fig. 3.4, the derivatives become

$$\frac{\partial p}{\partial x} = \frac{p^+_{i+1} + J_p - p_{i-1}}{x_{i+1} - x_{i-1}} \tag{3.27}$$

In this work, the Ghost Fluid method is used to account for pressure, velocities and density discontinuities at the interface as the value of the jump is known ($J_p = \sigma\kappa$ and $J_\rho = \rho_l - \rho_g$). As shown later in the validation tests, its use reduces

significantly the spurious currents due to the implementation of surface tension. Table 3.1 shows the transport equations solved in the code (velocities, species and energy) and the terms which are discretised using the Ghost Fluid method.

Table 3.1: Transport Equations and Terms discretised using the Ghost Fluid method

Transport Equation	Terms
$\frac{\partial \rho_k u_{k,k}}{\partial t} + \frac{\partial \rho_k u_{k,i} u_{k,k}}{\partial x_i} = \frac{\partial}{\partial x_i}(\mu_k \frac{\partial u_{k,k}}{\partial x_i}) - \frac{\partial p}{\partial x_k} + \sigma\kappa$	$\sigma\kappa$, $\frac{\partial \rho_k u_{k,i} u_{k,k}}{\partial x_i}$
$\frac{\partial \rho_k Y_{k,\alpha}}{\partial t} + \frac{\partial \rho_k u_{k,i} Y_{k,\alpha}}{\partial x_i} = \frac{S_{k,h}}{h_{fg}} + \rho_k W_{k,\alpha}$	$\frac{\partial \rho_k u_{k,i} Y_{k,\alpha}}{\partial x_i}$
$\frac{\partial \rho_k h_k}{\partial t} + \frac{\partial \rho_k u_{k,i} h_k}{\partial x_i} = \frac{\partial}{\partial x_i}(D_{h,k} \frac{\partial h_k}{\partial x_i}) + S_{h,k}$	–

The convective terms of the momentum and species equations are also treated using the concept of the Ghost Fluid method. The fluxes G_L and G_R are corrected in the cells where the interface is located. Using the information of the level set function, it is known that the interface is located between two cells where the sign of the function changes. Therefore, the fluxes of the face between these two cells must be corrected. Instead of using averages as indicated in Eq. 3.5 and 3.4, the flux is recalculated as $G_L = \rho_k u_{iI}$ and $G_R = \rho_k u_{iI}$ as indicated in Fig. 3.5.

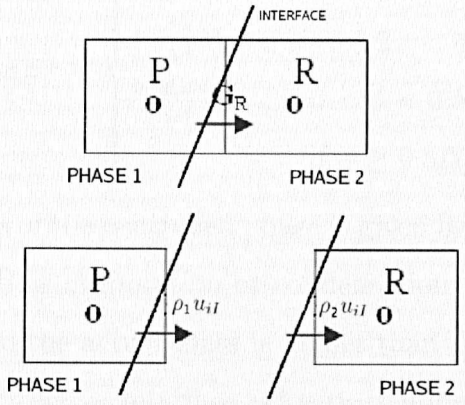

Figure 3.5: Corrected fluxes across the interface.

3.2.4 Mass Conservation Approach

As previously mentioned, the Level Set method is not inherently mass conserving. Depending on the interface movement and also due to the reinitialisation proce-

dure, very high mass losses and gains may occur in some calculations, especially when many time steps are necessary. The reinitialisation procedure often causes some bunching and stretching of the level set lines within the neighbourhood of the interface which causes mass conservation problems.

Many works have been developed coupling the Level Set method and the VOF in order to overcome this issue. In the present work, however, we use a simple and computationally efficient method to guarantee that mass is conserved. The approach assumes that the mass loss or gain is homogeneously distributed over the surface. At the end of each step, the mass of one of the phases defined as the controlled phase (liquid in this work), CF, is compared to the theoretical mass. The mass is calculated in each cell cointaining the controlled phase (including interface cells) using the value of the level set at the cell. This is achieved following

$$m_{CF} = \sum \rho_{cell,CF} V_{cell,CF} \tag{3.28}$$

where

$$V_{cell,CF} = \begin{cases} \Delta x^3, & \text{if } \phi \leq -0.5\Delta x \\ \frac{\phi + 0.5\Delta x}{\Delta x}, & \text{if } -0.5\Delta x < \phi \leq 0 \\ \frac{0.5\Delta x - \phi}{\Delta x}, & \text{if } 0 < \phi < 0.5\Delta x \\ 0, & \text{if } \phi \geq 0.5\Delta x \end{cases} \tag{3.29}$$

The theoretical mass of the controlled phase is given by the initial mass added by any source or sink, such as evaporation or condensation. If the difference between the theoretical mass and the actual mass is higher than a specified tolerance (0.1% in this work) then a corrective interface velocity is imposed all over the interface causing an artificial movement of the interface in order to correct the mass value (see Fig. 3.6).

In order to avoid instabilities, the correcting velocity is limited to half of the maximum velocity of the interface, u_{iI}, and is calculated by

$$v_{correct} = \frac{1}{A_{eq}\Delta t}\left(\frac{m_{CF}}{\rho_{CF}} - \frac{m_{teor}}{\rho_{CF}}\right) \tag{3.30}$$

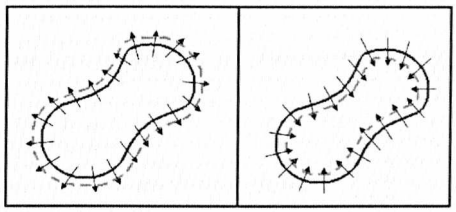

Figure 3.6: Corrective interface velocities due to mass loss (left) or mass gain (right).

The equivalent area, A_{eq}, varies depending on the interface shape. For squared surfaces with size l_s, for example, $A_{eq} = l_s^2$ and for spherical shapes with radius r, $A_{eq} = \frac{4}{3}\pi r^2$. If there are separated volumes of the controlled phase, as in the case of many droplets, the mass check can be done separately for each volume as each experiences different conditions such as evaporation rate, flow field and reinitialisation correction. Therefore, a different correction velocity must be applied to each volume.

3.2.5 Surface and Curvature Calculation

In order to calculate the heat transfer across an interface, the surface of the interface must be defined. Depending on the mesh resolution, the surface can be assumed as a plane in each cell. Assuming that the surface is a plane within the cell, the plane equation can be defined by a point, $\vec{x}_{int}$, and the normal vector, $\vec{N} = (N_x, N_y, N_z)$. The normal components are $N_x = \frac{1}{|\nabla\phi|}\frac{\partial\phi}{\partial x}$, $N_y = \frac{1}{|\nabla\phi|}\frac{\partial\phi}{\partial y}$ and $N_z = \frac{1}{|\nabla\phi|}\frac{\partial\phi}{\partial z}$.

In the present work, the normal in each cell is determined by using the level set function. A fourth order central difference scheme is used to calculate the derivatives. Hence, the components of the normal are given by

$$N_x = \frac{1}{|\nabla\phi|}\frac{-\phi_{i+2} - 8\phi_{i+1} - 8\phi_{i-1} + \phi_{i-2}}{12\Delta x} \tag{3.31}$$

$$N_y = \frac{1}{|\nabla\phi|}\frac{-\phi_{j+2} - 8\phi_{j+1} - 8\phi_{j-1} + \phi_{j-2}}{12\Delta y} \tag{3.32}$$

$$N_z = \frac{1}{|\nabla\phi|}\frac{-\phi_{k+2} - 8\phi_{k+1} - 8\phi_{k-1} + \phi_{k-2}}{12\Delta z} \tag{3.33}$$

The point in the plane is taken as the closest point from the interface to the cell center and is obtained using the position of the center of the cell, $\vec{x}_P$, and the normal, $\vec{N}$, following

$$\vec{x}_{int} = \vec{x}_P + \phi_P \vec{N} \tag{3.34}$$

The absolute value of the gradient, $|\nabla\phi|$, is computed with the fifth order WENO scheme implemented for the reinitialisation procedure.

Knowing a point on the interface and the normal, the surface plane equation can be obtained by

$$ax + by + cz + d = 0 \tag{3.35}$$

with

$$a = N_x, \quad b = N_y, \quad c = N_z \quad and \quad d = -(ax_{int} + by_{int} + cz_{int})$$

In order to define the surface inside the cell, the points where the plane crosses the edges of the cell must be identified. This is achieved by checking the points where the plane equation is equal to the line equation of the edges (12 in total). Then, depending on the number of points, the type of polygon inside the cell (triangle, quadrangle, pentagon or hexagon) is determined as shown in Fig. 3.7. The polygons which have more than 3 vertices are split into triangles. The areas of the triangles are then easily calculated and the surface is the sum of all the areas.

The corners of the polygons must be ordered so they can be correctly split into triangles avoiding overlapping or gap of surface. They are ordered by defining a first point and then finding a consecutive point to the original point. A consecutive point is a point located on the same face as the original point. Once the points are ordered, the surface can be split into triangles following the points' sequence.

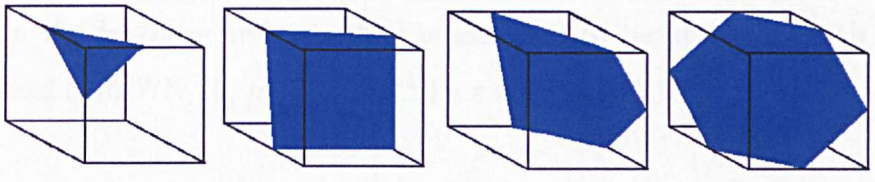

Figure 3.7: Possible configurations of a plane crossing a cube.

As previously mentioned, the curvature can be obtained by using the level set function. The curvature is essential for the surface tension implementation. It can be easily calculated by

$$\kappa = \frac{\partial}{\partial x_i}\left(\frac{\frac{\partial \phi}{\partial x_i}}{|\nabla \phi|}\right) \tag{3.36}$$

The second derivative of the level set function is calculated using a second order central difference scheme. The absolute value of the gradient uses the fifth order WENO scheme.

3.3 Validation test cases

Potential sources of errors in the model must be investigated in order to verify the accuracy and to quantify the uncertainties. The first test case compares the use of the less computationally expensive one-fluid formulation for the solution of the velocity transport equations and the two-fluid formulation. Other important sources of errors are surface tension modelling and spurious currents generated by this modelling. The interface area and curvature calculation can also induce significant deviations in the surface tension modelling and the heat transfer calculation. Furthermore, in order to validate the model, the momentum transfer between phases must also be checked. The interactions between different volumes of liquid must also be validated. The mass conservation approach is also tested to guarantee that the liquid mass gain or loss are within accepted limits. Finally, the heat tranfers and the chemistry are verified.

A number of different test cases are performed in order to quantify these errors and are described in Table 3.2. In the methanol tests, the fuel is assumed to be at 338 K with $\rho_l = 750$ kg/m^3, $\sigma = 1.85\ 10^{-2}$ N/m, $\mu = 3.5\ 10^{-4}$ Pa.s and $h_{fg} = 1.097$ MJ/kg. In the kerosene test, the fuel is assumed to be at 335 K with $\rho_l = 770$ kg/m^3, $\sigma = 2.0\ 10^{-2}$ N/m, $\mu = 8.2\ 10^{-4}$ Pa.s and $h_{fg} = 310$ MJ/kg.

Table 3.2: Validation Test Cases

Section	Test	u_∞ [m/s]	T_∞ [K]	Drops	Fuel	d [μm]	p [atm]
3.3.1	Fluid Formulation	0	2500	2	Methanol	100	1
3.3.2	Surface Tension Model	0	338	1	Methanol	100	1
3.3.3	Surface Area	0	338	1	Methanol	40-400	1
3.3.4	Momentum Coupling	10-30	338	1	Methanol	40	1
3.3.5	Mass Conservation	$u_c = 10$	338	1	Methanol	100	1
3.3.6	Film Heat	0	1500	-	Kerosene	-	1

3.3.1 One- and Two-fluid Formulations

Initially, all the governing equations were implemented following a one-fluid formulation. However, it is observed that following the one-fluid formulation for velocities, it is necessary to smooth the properties across the interfaces in order to maintain the model stability. The smoothing of the properties introduces unrealistic physics into the model and the errors induced must be evaluated.

Figure 3.9 shows the velocity profiles for a test case where two 100 μm droplets are placed in a hot stagnant environment. The hot ambient is characterised by fixed radial temperature gradient that goes from 2500 K away from the droplets to 338 K at the droplet surface (see Fig. 3.8). The droplets are at constant temperature (338 K). Radial velocities are induced by evaporation of the droplets. The profile shown in Fig. 3.9 is along a line passing through the center of the two droplets. The circles indicate the regions where the radial velocity is close to zero i.e. where the droplets reside. Away from the droplets the velocity increases because of the density difference due to the imposed radial temperature gradient.

In the one-fluid formulation, it can be seen that the velocity peaks are not symmetric and the peaks between the droplets are lower than in the outer region. Furthermore, because of the density smoothing around the droplet, the peak is lower than in the two-fluid formulation where the properties are treated as a steep jump. The two-fluid formulation captures well the peak value and represents well the symmetry of the problem.

As the one-fluid formulation fails to accurately treat the immediate neighbourhood of the droplets, the two-fluid formulation is adopted in this work for the velocity and species equations. For the energy equation, because the relative jump in en-

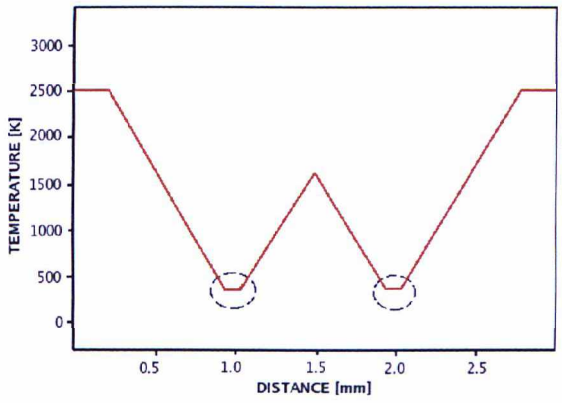

Figure 3.8: Fixed radial temperature profile of a 2-droplet case.

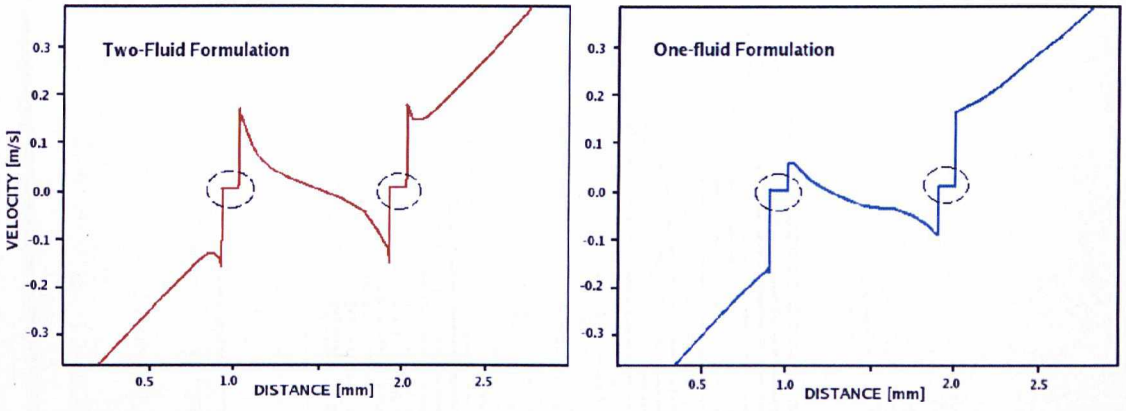

Figure 3.9: Comparison of radial velocity profile induced by Stefan flow in one and two-fluid formulations.

thalpy ($J_h = \frac{h_{fg}}{c_p(T_{max}-T_{min})}$) is much lower and in most of the cases studied the liquid phase remains at constant temperature, the one-fluid formulation is used for the energy equation.

3.3.2 Curvature and Surface Tension

Errors in the curvature calculation directly affect the pressure jump across the surface due to surface tension modelling ($J_p = \sigma\kappa$). The Laplace problem is simulated to investigate the effects of the surface tension modelling. This problem is chosen because the dynamical system is close to equilibrium. Under these conditions it is easier to evaluate the numerical errors. A major consequence is the appearance of

spurious or parasitic currents observed within many calculation where the surface tension effects are dominant. These currents are generated in the vicinity of the interfaces and their magnitudes can be evaluated by the simulation of static droplets surrounded by a different fluid in zero gravity environment.

A 50 μm droplet is placed in a stationary environment and different combinations of surface tension, σ, and viscosity, μ, are investigated in three-dimensional cases. Figure 3.10 shows that these currents can generate vortical flows despite the absence of external forces. The currents depend on the surface tension coefficient, σ, and the viscosity, μ.

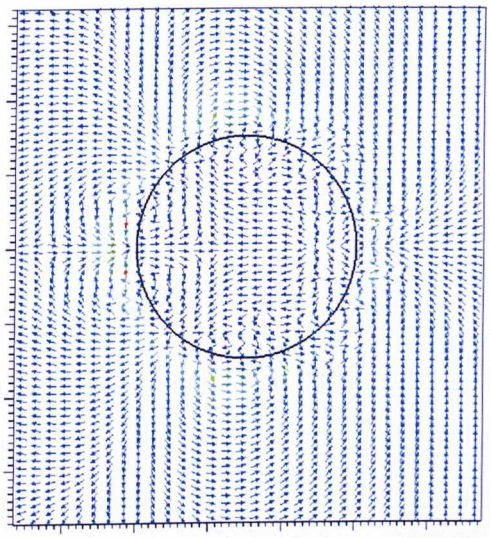

Figure 3.10: Spurious currents generated by surface tension modelling.

Figure 3.11 presents the maximum velocities generated by spurious currents. For the same droplet diameter, these values are correlated to the ratio $\frac{\sigma}{\mu}$ in accordance with Renardy and Renardy, 2002. For the entire range investigated, $0.1 < \frac{\sigma}{\mu} < 100$, the maximum velocities reached are lower than 0.1 m/s. Moreover, the model used in this work (present implementation) presents better results than published in Coyajee et al., 2004, for the pure Level Set method (denoted LS) ($\frac{\sigma}{\mu} > 8$) and for a mass conserving Level Set (denoted MCLS) ($\frac{\sigma}{\mu} > 0.2$).

The errors in curvature increase when the number of cells across the droplet radius decreases. The errors are lower than 2% for droplet with more than 5 cells

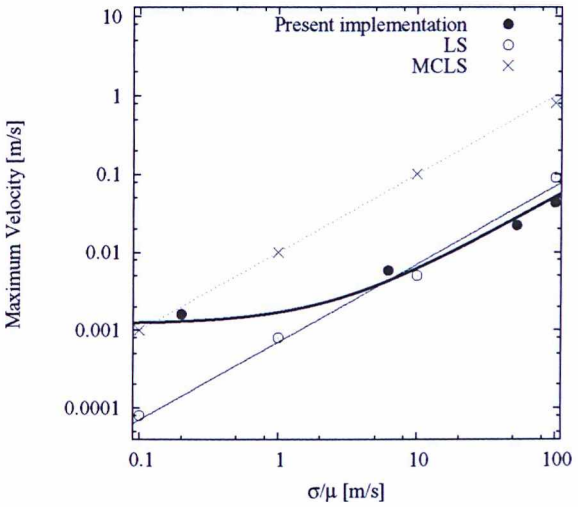

Figure 3.11: Maximum velocity induced by spurious currents for different $\frac{\sigma}{\mu}$.

and are around 10% for droplets with 2 cells across the radius.

3.3.3 Surface Calculation

The interface surface that is used to calculate the heat transfer and mass evaporation rate is computed in each cell using the level set function. Since surfaces are assumed to be planar in each cell, errors strongly depend on mesh resolution and curvature of the surface. The tests performed evaluate the difference between the surface computed by the code and the theoretical surface for droplets with different number of cells across the radius.

The tests show that even for droplets with only 2 cells across the radius, the errors in total droplet surface calculation are lower than 7%. Figure 3.12 shows the effects of the number of cells on droplet surface errors. Increasing the number of cells, the error decreases significantly and for droplets with more than 5 cells across the radius, the errors in the total surface area calculation are lower than 1%.

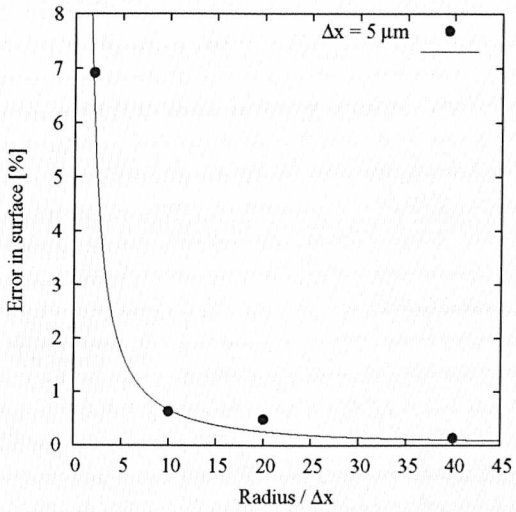

Figure 3.12: Error in surface area calculation as function of number of cells per radius.

3.3.4 Momentum Coupling

An important aspect of multiphase flows is the coupling between the liquid and gas phases. The coupling is responsible for the transfer of momentum, mass and energy. In this subsection we discuss the momentum coupling as mass and energy exchanges are discussed later. The movement of the gas phase directly influences the movement of the liquid phase and vice-versa. Some examples only take into account the effects of the gas on the liquid phase (one way coupling) as they assume that the reverse effect is not significant. This might be true for very small liquid volume fractions, however, it is not a reasonable assumption for two-phase flows in general. A two-way coupling must be used and in this work, both effects are included via the extension of the ghost cells and the pressure correction procedure.

The momentum coupling can be tested by examining the drag force. The test performed consists in calculating the drag coeffient of a liquid cylinder (two-dimensional case) and a droplet (three-dimensional case) under different air flow field conditions. The liquid bodies are placed in laminar flows with different Reynolds numbers. The drag coefficients of the cylinder and droplet are compared to the experimental data (Potter and Wiggert, 2002). The Reynolds number is based on the mean flow velocity and the cylinder or sphere diameter (40 μm with $\Delta x = 5\mu m$).

The range of mean velocities varies from 10 to 30 m/s.

The results in Fig. 3.13 show good agreement of the cylinder test with the experiments. The relative difference is always below 15%. In the sphere test, the agreement is better and the relative error is always lower than 10% (see Fig. 3.13). Therefore, the coupling of momentum is considered effective.

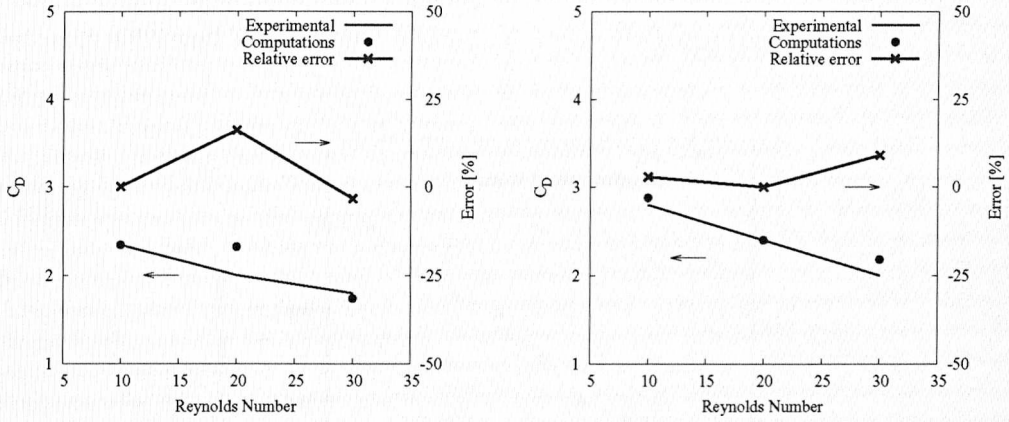

Figure 3.13: Drag coefficient and error in calculation of 40 μm cylinder (left) and sphere (right) under different flows.

3.3.5 Mass Conservation

The mass conservation is ensured by the pressure correction procedure. However, at the interface cells, the displacement of the level set might induce mass errors. The potential violation of mass conservation by the Level Set method is an important issue that must be evaluated. In order to overcome this issue, a special mass conserving approach, described in Section 3.2.4, is implemented.

The gain or loss of mass due to the Level Set method occurs when the liquid volume moves through the domain. The new mass conserving approach is a geometric reconstruction. The approach checks at the end of each step how much the mass of the liquid volume differs from the theoretical mass it should have. If the difference is higher than a specified tolerance (0.1%), the correction is applied to the level set function in order to correct the liquid volume.

The test performed consists of a single droplet ($d = 100\mu m$) placed in a laminar

environment moving with relative velocity of 10 m/s. This condition is chosen because as the liquid phase moves faster, the loss or gain of mass becomes more evident. Figure 3.14 shows that within about 1000 steps ($t \approx 10$ ms), the Level Set method without the mass conserving approach leads to a mass loss of around 0.35%. On the other hand, the mass conserving approach guarantees that the mass variation remains within the specified tolerance (0.1%). The results prove that mass correction is achieved when using the mass conserving approach.

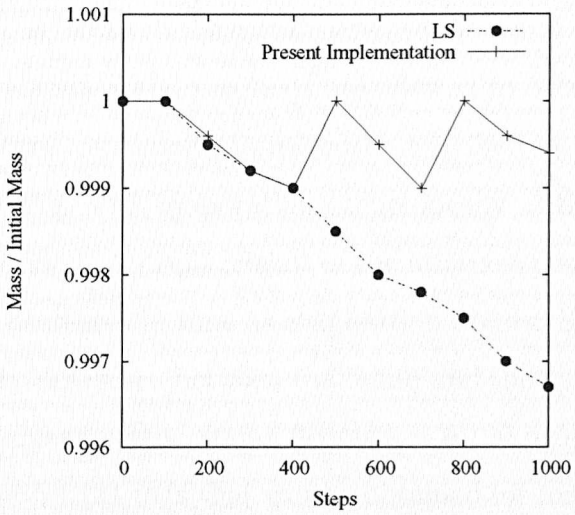

Figure 3.14: Evolution of the relative mass of a methanol droplet moving in a laminar air environment with relative velocity of 10 m/s.

The same test is performed in a hot environment ($T_{air} = 1500$ K) where evaporation of the droplet occurs. However, as the velocity of contraction of the surface due to evaporation ($u_{evap} \approx 10^{-3}$ m/s) is much lower than the convective velocity ($u_c = 10$ m/s), the effect of this component is not significant and the results are very similar to the non-evaporating case.

3.3.6 Heat Transfer and Reactions

Modelling of heat transfer is a difficult task because it depends on the accuracy of the computation of the temperature gradients, transfer surface area and on the appropriate definition of gas phase physical properties. A detailed comparison of

evaporation rates in droplets against experimental results and commonly used numerical models is the scope of Chapter 4. The main issues with respect to the properties definitions are also discussed there and are not discussed in the present chapter.

The test case presented in this section consists of a domain where a film of kerosene at low temperature (335 K) is located in a hot air environment (1500 K). The boundary conditions are symmetry on the sides in contact with the film and outflow otherwise. The temperature of the film is assumed to remain constant (e.g. at saturation conditions) so all the heat transfered to the liquid phase results in evaporation. Vapour is generated and reactions are allowed to occur. The temperature gradient and surface are calculated as previously described in this chapter.

As can be seen in Fig. 3.15, evaporation occurs locally at the cells where the interface surface is identified. A displacement of the interface position is observed and the volume of liquid decreases in time as evaporation occurs. Stefan flow is induced because of the density difference between the liquid and the generated vapour. The maximum velocity induced by the Stefan flow is $v = 0.120$ m/s and agrees with the theoretical value of $v = 0.121$ m/s that can be obtained for mass conservation.

The reactions occur in a region distant from the interface where the mixture fraction is close to the stoichiometric value. Figure 3.15 shows the consumption of oxygen and kerosene and the generation of water and carbon dioxide. The flame is non-premixed and the flame zone moves in the direction of the Stefan flow toward the oxidizer since locally the concentration of oxygen decays due to the reactions. The reactions are sustained until there is no more oxygen to react and the flame disappears. The evaporation rate is then reduced and approaches zero when in the absence of a source of heat - thermal equilibrium between gas and liquid phase is reached. The computation therefore correctly represents the physics.

The validation of the chemical mechanisms are not presented here as they are beyond the scope of this thesis. They were validated in other works such as Jones and Lindstedt, 1988 and Liu et al., 2004.

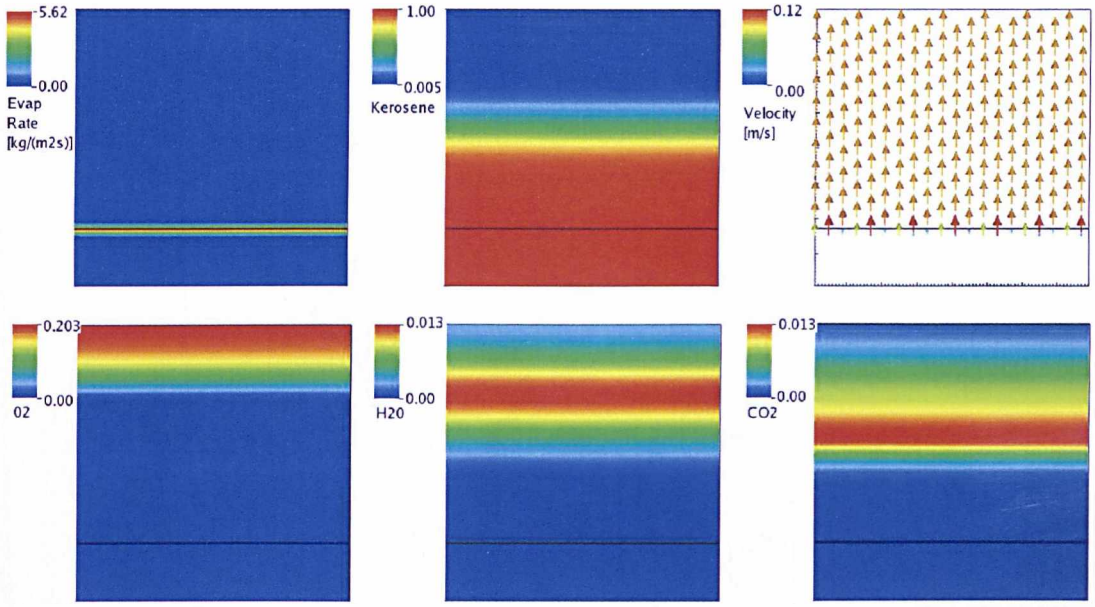

Figure 3.15: Evaporation rate, kerosene fraction, velocities, oxygen concentration, water concentration and carbon dioxide concentration of a kerosene film in a 1500 K ambient.

3.3.7 Liquid Interactions

Interface interactions occur frequently in two-phase flows. In terms of modelling, merging and separation of interfaces can be critical for interface tracking methods as they may cause numerical instabilities, fake interface deformation and loss or gain of mass. In this section, a qualitative comparison of experimental data with the results obtained with the implemented model is presented for completeness. However, the detailed assessment of droplet interactions is beyond the scope of this thesis.

It is known that aqueous and non-aqueous liquids have different behaviours because of the difference in the ratio between viscosity and surface tension. Water is a relatively low viscosity liquid with a relatively high surface tension. Ethanol, for example, has viscosity approximately 10% higher and surface tensions around 60% lower than water. As this work concerns fuel sprays, only non aqueous fuels were tested. However, it is expected that the results with water are similarly accurate.

The interaction conditions vary with the angle and intensity of the impact. Fol-

lowing the scheme in Fig. 3.16, the impact velocity is defined as

$$U = (V_1 + V_2) \sin\left(\frac{\theta}{2}\right) \tag{3.37}$$

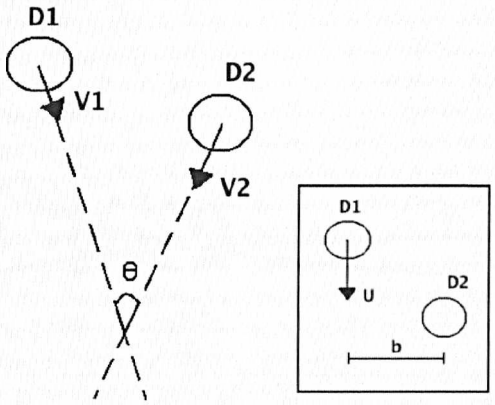

Figure 3.16: Droplet collision scheme.

Different droplet collision regimes can be identified such as coalescence, separation and bouncing. Figure 3.17 indicates the interaction regimes of methanol droplets as function of the impact velocity, $I = \frac{2b}{D_1+D_2}$, and the Weber number, $We = \frac{\rho U^2(D_1+D_2)}{\sigma}$. The points represent different experiments realised by Estrade et al., 1999. In the coalescence regime the gaseous interface between the droplets is lost and a single droplet is formed. The separation regime occurs with unstable coalescence where the big droplet breaks into new droplets. If a droplet formed is smaller than the initial droplets, it is called satellite. Different from the two previous regimes, in the bouncing regime a thin gaseous film remains between the interfaces.

In this work, two tests are performed in order to verify the ability of the model to handle droplet interface interactions appropriately. Two ethanol droplets are placed in an inert environment with relative impact velocity of 4.5 m/s and $We = 100$. The impact parameter, I, is different so the regimes of coalescence and bouncing occur. Pergamalis, 2002, presented experimental results of ethanol droplet collisions and these results are used to validate the model as follows.

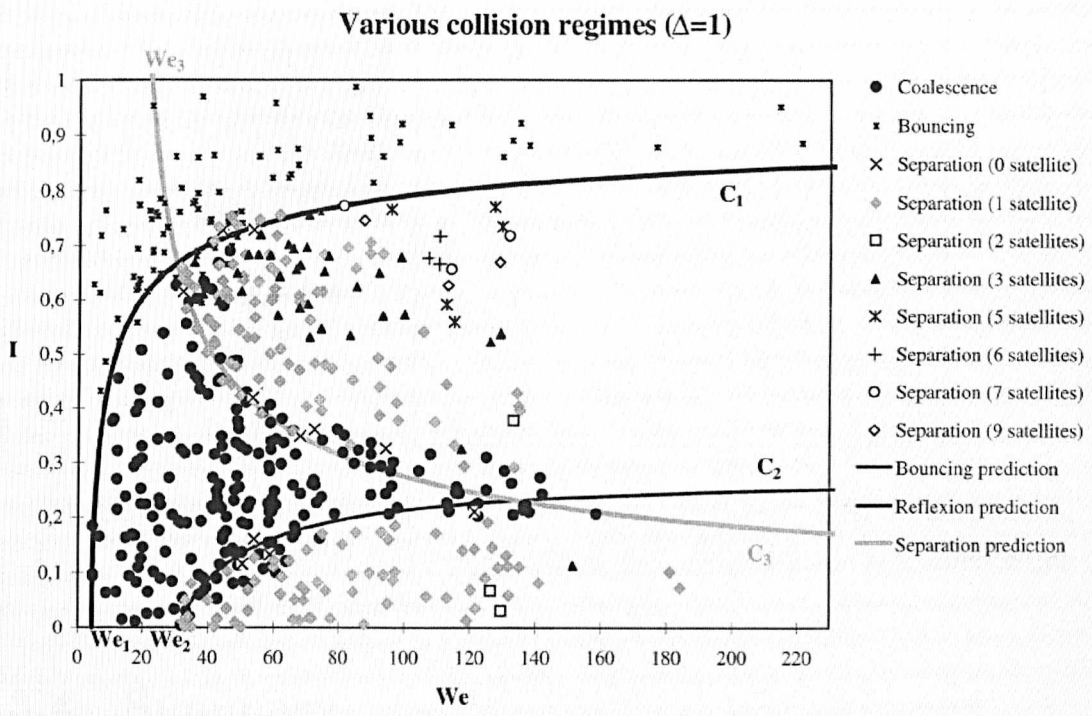

Figure 3.17: Ethanol droplet collision regimes for $\Delta = \frac{D_1}{D_2} = 1$ (Estrade et al., 1999).

3.3.7.1 Coalescence

This test case is performed with impact parameter $I = 0$. The droplets suffer frontal collision and merge. No significant stretching or separation is observed. The droplets collide and form a single droplet that oscillates for some time and then reaches stability in the spherical shape. The mass conserving level set approach seems to capture well the behaviour observed in the experiments as shown in Fig. 3.18.

3.3.7.2 Bouncing

The bouncing regime is observed with $I = 0.9$. The collision occurs laterally and the surfaces seem to merge locally, however, the link is not sustained and a gaseous film remains between the two droplets. Comparing the numerical results with the experiments, it can be noted that the droplets dynamics seem to be very well captured and a good qualitative agreement is found (see Fig. 3.19).

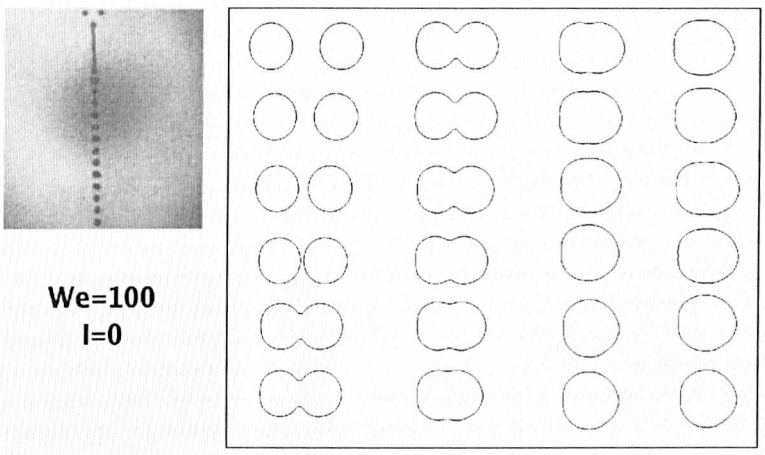

Figure 3.18: Evolution of binary collisions between ethanol droplets at We=100 and I=0 - Coalescence. Experiments (left) and simulations (right).

3.4 Summary

The present chapter describes in detail the novel numerical model used in this work. The model uses a hybrid one and two-fluid formulation. The interface tracking is explained through the description of the mass conserving Level Set approach implemented and the Ghost Fluid method applied for surface tension modelling.

In order to validate the model, different test cases are performed. The tests verify the accuracy of the model and the results are compared to known solutions or to experimental data. The tests performed are: curvature, surface tension and interface surface calculation, momentum coupling, mass conservation, liquid interactions, heat transfer and reactions evaluation. The assessment of evaporation rates and modelling is presented in Chapter 4 and the application of the model to investigate gas-phase mixing is discussed in Chapter 5.

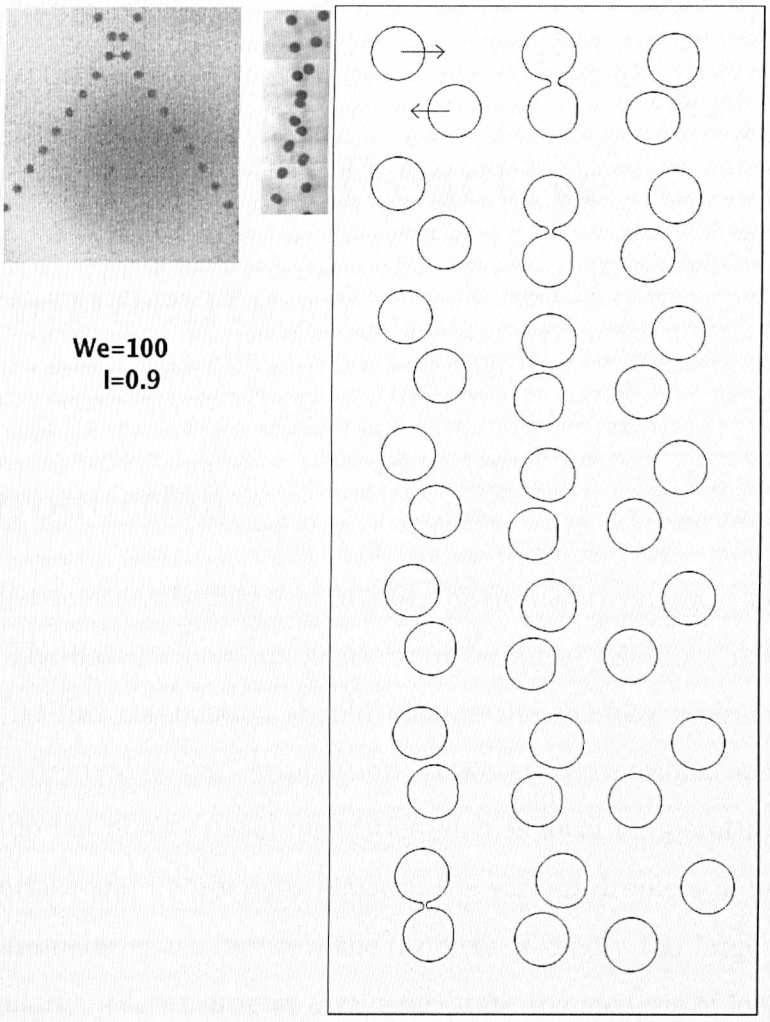

Figure 3.19: Evolution of binary collisions between ethanol droplets at We=100 and I=0.9 - Bouncing. Experiments (left) and simulations (right).

Chapter 4

Evaporation in Reactive Environments

4.1 Introduction

In liquid fuelled devices, the fuel is atomised, the droplets evaporate and combustion takes place. The flow in most applications of technical relevance is turbulent and studies of liquid fuel combustion should include the complex interactions between turbulence, spray breakup and evaporation. However, conventional spray studies are complex and do not allow crucial quantities such as local temperature gradients at the droplet surface and interactions between the various droplets to be easily quantified. The parameter space between the droplets is simply too large and although studies of regularly ordered droplet arrays facilitate the analysis of local effects that determine evaporation rates, these are impossible to realise experimentally.

Theoretical and numerical studies provide an alternative to the experiments, but the modelling of the physical processes involved is difficult, especially in turbulent environments due to the range of associated length and time scales which may spread over several orders of magnitude. To the author's knowledge, only few numerical works exist (Imaoka and Sirignano, 2005) that are capable of directly quantifying the effect of droplet interactions on evaporation rate and subsequent combustion.

Modelling of droplet evaporation normally assumes that the process is quasi-

steady, uniform temperature of the droplet (infinite conductivity of the liquid) and constant properties of gas around the droplet. These are all significant simplifications but allow a simple closed-form solution. The evaporation models and the definition of the gas properties are discussed in detail in this chapter.

The present work assesses the effects of droplet density and turbulence on evaporation rates in inert and reactive turbulent environments using Direct Numerical Simulations (DNS) of *n*-heptane and kerosene droplet arrays as described later. The two phases are fully represented, capturing the interface location and resolving all the scales of turbulence as described in Chapter 3. First, the evaporation rates obtained with the DNS of *n*-heptane droplets are compared to experimental investigations on single droplet evaporation (Birouk et al., 2000; Wu et al., 2001). Then, the DNS results of *n*-heptane and kerosene are compared to existing models of droplet evaporation (see (Kuo, 1986; Sazhin, 2006)) where the differences are quantified and analysed.

This chapter is divided in six sections. The next section describes the derivation of the evaporation models used in the literature through the species and energy balances. The third section presents the test cases performed. The fourth and fifth sections present the results and analysis for the DNS of *n*-heptane and kerosene, respectively. Finally, the last section presents a summary of the chapter.

4.2 Evaporation Modelling

When a liquid droplet is exposed to a hot environment, evaporation occurs and the temperature of the droplet rises until it evaporates completely or the temperature reaches the boiling value. If the droplet reaches the boiling temperature, then the process can be assumed quasi-steady and all the heat transferred to the droplet effectively results only in liquid vaporisation. Under this condition, heat and mass transfer are energetically equivalent.

Vapour is generated at the surface of the droplet when evaporation occurs. The vapour concentration at the interface is important and is used in many evaporation models. It is a balance of production on one side and diffusion and convection

on the other side. In local thermodynamic equilibrium, this concentration can be calculated if the partial pressure, p_{pv}, at the surface, which is directly conditioned on the surface temperature, T_d, is assumed to be the saturation pressure. Thus, the partial pressure at the surface can be calculated from the Clausius-Clapeyron equation:

$$\ln \frac{p_{pv}}{p_{amb}} = \frac{h_{fg}}{R} \left(\frac{1}{T_d} - \frac{1}{T_{boil}} \right) \tag{4.1}$$

where T_{boil} is the fuel boiling temperature at the ambient pressure p_{amb}. Then, the vapour concentration at the surface, Y_s, is obtained by

$$Y_s = \frac{p_{pv} W_{fuel}}{p_{amb} W_{mix}} = \frac{p_{pv} W_{fuel}}{p_{pv} W_{fuel} - (p_{amb} - p_{pv}) W_{air}} \tag{4.2}$$

The evaporation process is directly affected by the flow field and vice-versa. The heat and mass transfer to the droplet results from these interactions. Because of evaporation, the temperature and the composition surrounding the droplet are different from the free stream values. The droplet evaporation also changes the flow field in the vicinity of the droplet because of the velocities induced by the difference between the density of liquid and vapour (Stefan Flow). Moreover, variations of the inflow boundary conditions such as velocity and temperature, strongly affect the evaporation process. Accounting for these interactions can be complex and accurate modelling is not straight forward without making further assumptions.

In order to obtain models for the evaporation rate of droplets, different derivations have been proposed. The derivations are not based on the same assumptions and therefore the equations obtained are not the same. However, the main assumptions used by all the models is that the thermophysical properties are constant in the gas phase and that the droplets have uniform temperature (infinite conductivity). Although properties vary greatly with temperature and composition through the domain, constant properties simplify the problem and allow simple closed-form solutions. Equations for the evaporation rate can be obtained through the species and energy governing equations.

4.2.1 Species balance in the gas phase

The evaporation rate can be calculated from the species balance equation for the gas phase. The derivation presented here assumes that the droplet temperature is at a fixed value below the boiling temperature. The vapour fraction at the surface can be obtained assuming thermodynamic equilibrium through the Clausius-Clapeyron equation, as previously explained. A driving potential for mass transfer, the mass transfer number, B_k, is defined as

$$B_k = \frac{Y_S - Y_\infty}{1 - Y_S} \tag{4.3}$$

Neglecting convective effects and assuming quiescent environment, the vapour conservation equation can be written as

$$\frac{\dot{m}_d}{4\pi r_d^2} = -\frac{\rho D}{1-Y}\frac{dY}{dr}. \tag{4.4}$$

Integrating Eq. (4.4) and applying the known boundary condition $Y(r_d) = Y_S$, the equation for the vapour concentration in radial direction is

$$Y(r) = \frac{(1 - Y_S)\exp(-\frac{\dot{m}_d}{4\pi\rho D r})}{\exp(-\frac{\dot{m}_d}{4\pi\rho D r_d})}. \tag{4.5}$$

Then, knowing $Y(\infty) = Y_\infty$ and solving Eq. (4.5) when $r \to \infty$, the droplet evaporation rate, $\dot{m}_d$, can be expressed as

$$\dot{m}_d = 4\pi\rho D r_d \ln\left(\frac{1 - Y_\infty}{1 - Y_s}\right) = 4\pi\rho D r_d \ln(B_k + 1). \tag{4.6}$$

4.2.2 Energy balance in the gas phase

Starting from the energy balance in the gas phase, an alternative equation for the evaporation rate can be derived. The main assumption of this derivation is that the droplet is at boiling temperature. This assumption seems appropriate for very hot environments such as reacting flows where the droplets reach saturation temperature in a short time compared to the droplet lifetime.

In a stagnant environment for pure evaporation cases with $Le = 1$, the Shvab-Zeldovich energy equation in spherical coordinates (Turns, 1996) is

$$\frac{d}{dr}\left(r_d^2 \frac{dT}{dr}\right) = \frac{\dot{m}_d c_{pg}}{4\pi k_g} \frac{dT}{dr}. \tag{4.7}$$

Knowing the boundary conditions $T(\infty) = T_g$ and $T(r_d) = T_{boil}$, Eq. (4.7) can be integrated and the temperature's radial distribution is obtained for

$$T(r) = \frac{T_{boil} + (T_g - T_{boil}) \exp\left(-\frac{Z\dot{m}_d}{r}\right) - T_g \exp\left(-\frac{Z\dot{m}_d}{r_d}\right)}{1 - \exp\left(-\frac{Z\dot{m}_d}{r_d}\right)} \tag{4.8}$$

where $Z = c_{pg}/(4\pi k_g)$.

Assuming $T_d = T_{boil}$, all the heat conducted to the droplet goes to evaporation of the liquid phase. As heat is conducted to the droplet interface from the hot gas, the temperature gradient at the surface is given by

$$4\pi k_g r_d^2 \left.\frac{dT}{dr}\right|_g = \dot{m}_d h_{fg} \tag{4.9}$$

where the enthalpy of evaporation is $h_{fg} = h_v - h_l$.

Deriving Eq. (4.8) and solving for $\dot{m}_d$

$$\dot{m}_d = \frac{4\pi k_g r_d}{c_{pg}} \ln(B_q + 1) \tag{4.10}$$

where the heat transfer number, B_q, is the driving potential and is expressed as

$$B_q = \frac{c_{pg}(T_g - T_d)}{h_{fg}} \tag{4.11}$$

A different definition of the heat transfer number is proposed when combustion occurs, including the enthalpy of combustion, Δh_c, and the stoichiometric ratio, f_{stoic}, as follows (Turns, 1996).

$$B_{q,c} = \frac{\Delta h_c / f_{stoic} + c_{pg}(T_\infty - T_d)}{h_{fg}}. \tag{4.12}$$

The enthalpy of combustion is included in this definition because the gas phase temperature is considered as the temperature at infinity and not including the temperature increment due to the reactions. As filtered temperatures are used in the present work, this transfer number does not apply in the present investigations.

4.2.3 Energy balance of a single droplet

The evaporation rate can also be determined through the energy balance in the liquid phase, i.e. the droplet. This derivation introduces the Nusselt number and allows convective environments to be considered. In order to investigate the evaporation of an isolated droplet in a quiescent environment, the energy equation can be written as

$$4\pi k_g r_d^2 \left.\frac{dT}{dr}\right|_g = m_d c_{pd} \left.\frac{dT}{dt}\right|_l + \dot{m}_d h_{fg}. \tag{4.13}$$

Then, the droplet temperature variation in time can be expressed as

$$\left.\frac{dT}{dt}\right|_l = 4\pi k_g r_d^2 \left.\frac{dT}{dr}\right|_g - \frac{\dot{m}_d h_{fg}}{m_d c_{pd}}. \tag{4.14}$$

The Nusselt number, Nu, defined via the normalised heat flux across a surface, is introduced as follows.

$$Nu = \frac{q d_d}{(T_g - T_d) k_g} \tag{4.15}$$

In the case of droplet evaporation the heat, q, is equivalent to the rate of heat conducted from the gas phase to the droplet.

$$q = k_g \left.\frac{dT}{dr}\right|_g \tag{4.16}$$

Therefore, the Nusselt number, Nu, becomes

$$Nu = \frac{k_g \left.\frac{dT}{dr}\right|_g d_d}{(T_g - T_d) k_g}. \tag{4.17}$$

The Nusselt number has been widely investigated under different gas environ-

ments and several correlations have been proposed to take convection into account. Some proposed correlations for the Nu and Sh of convective environments are presented later in this section. For quiescent environments $Nu = 2$ and $Sh = 2$.

Rearraging Eq. (4.13), the droplet temperature variation in time can be rewritten as

$$\left.\frac{dT}{dt}\right|_l = \frac{2\pi k_g r_d Nu}{m_d c_{pd}}(T_g - T_d) - \frac{\dot{m}_d h_{fg}}{m_d c_{pd}}. \tag{4.18}$$

Introducing the Prandtl number,

$$Pr = \frac{c_{pg}\mu_g}{k_g}, \tag{4.19}$$

the droplet temperature variation equation becomes

$$\left.\frac{dT}{dt}\right|_l = \frac{2\pi r_d \mu_g}{m_d}\frac{c_{pd}}{c_{pg}}\frac{Nu}{Pr}(T_g - T_d) - \frac{\dot{m}_d h_{fg}}{m_d c_{pd}}. \tag{4.20}$$

As the droplet mass is $m_d = \frac{\rho_l 4\pi r_d^3}{3}$, the new droplet temperature equation is

$$\left.\frac{dT}{dt}\right|_l = \frac{3\mu_g}{2\rho_l r_d^2}\frac{Nu}{Pr}\frac{c_{pd}}{c_{pg}}(T_g - T_d) - \frac{\dot{m}_d h_{fg}}{m_d c_{pd}} \tag{4.21}$$

and the droplet temperature is given by

$$dT_d = \frac{3\mu_g}{2\rho_l r_d^2}\frac{Nu}{Pr}\frac{c_{pd}}{c_{pg}}(T_g - T_d)dt + \frac{h_{fg}}{c_{pd}}\frac{dm_d}{m_d}. \tag{4.22}$$

With the assumption that the droplet is at saturation temperature, the mass evaporation rate $\dot{m}_d$ is given by

$$\dot{m}_d = 2\pi r_d \frac{Nu}{Pr}\mu_g B_q \tag{4.23}$$

where the heat transfer number, B_q, is defined as in Eq. (4.11). This equation is similar to the equation obtained from the energy balance in the gas phase (Eq. (4.10)), however, here the Nusselt number is introduced.

The process of evaporation is controlled by heat transfer when $T_d = T_{boil}$ and then Eq. (4.23) is appropriate (Lederlin and Pitsch, 2008) and the driving potential is

the heat transfer number. However, when the evaporation rate is controlled by mass transfer ($T_d \leq T_{boil}$), the driving potential is the gradient of vapour concentration. In this case, the normalised heat flux across a surface is replaced by the normalised diffusion accros the interface defined by the Sherwood number, Sh. Assuming unity Lewis number, $Sh = Nu$. Therefore, the the mass evaporation rate $\dot{m}_d$ can be written

$$\dot{m}_d = 2\pi r_d \frac{Sh}{Sc} \mu_g B_k \tag{4.24}$$

where the mass transfer number, B_k, is defined as in Eq. (4.3).

4.2.4 Nusselt and Sherwood numbers correlations

The Nusselt and Sherwood numbers are commonly used in evaporation models because as they can take into account the effects of convection. The Nusselt number represents the thermal interaction between the droplet and the surroundings and defines the normalised heat flux across the interface in Eq. (4.17). The Sherwood number is the analogous number regarding the mass flux across the interface.

The effects of convection are introduced by defining these numbers as functions of the Reynolds number, Re. Some proposed correlations, resulting from experimental studies and describing $Nu = f(Re, Pr, B_q)$ and $Sh = f(Re, Sc, B_k)$ are discussed below. These correlations are also compared in order to evaluate their effects on the evaporation rate modelling. The Prandtl and Schmidt numbers are commonly assumed to be 0.7.

Frossling, 1938, first proposed that

$$Nu = 2 + 0.552 Re_k^{1/2} Pr^{1/3} \tag{4.25}$$

where the Reynolds number is based on the gas properties, the relative velocity and the droplet diameter,

$$Re_k = \frac{\rho_g U_{rel} d}{\mu_g}. \tag{4.26}$$

Analogous results are proposed for the Sherwood number, Sh,

$$Sh = 2 + 0.552 Re_k^{1/2} Sc^{1/3}. \tag{4.27}$$

Faeth, 1977, proposed different correlations for the Nusselt and Sherwood numbers as

$$Nu = 2 + \frac{0.555 Re_k^{1/2} Pr^{1/3}}{(1 + \frac{1.232}{RePr^{4/3}})^{1/2}} \tag{4.28}$$

and

$$Sh = 2 + \frac{0.555 Re_k^{1/2} Sc^{1/3}}{(1 + \frac{1.232}{ReSc^{4/3}})^{1/2}}. \tag{4.29}$$

Clift et al., 1978, identified that for different Reynolds number ranges, the correlations should be distinct. Therefore, they proposed correlations that vary with the Reynolds number.

$$Nu = 1 + (1 + RePr)^{\frac{1}{3}} f(Re) \tag{4.30}$$

$$Sh = 1 + (1 + ReSc)^{\frac{1}{3}} f(Re) \tag{4.31}$$

with

$$f(Re) = \begin{cases} 1, & \text{if } Re \leq 1 \\ Re^{0.077}, & \text{if } 1 < Re \leq 400. \end{cases}$$

According to Eq. (4.23) and (4.24), the evaporation rate is directly related to the Nusselt or Sherwood number. Figure 4.1 shows that the correlations proposed by Frossling, 1938, Faeth, 1977, and Clift et al., 1978, have very similar values for the Reynolds number of interest (10-200) in the present work. This indicates that no significant difference in the evaporation rate is caused by the choice of the Nusselt or Sherwood correlation in this range.

4.2.4.1 Models using modified Nusselt and Sherwood numbers

There are two well known droplet evaporation models commonly used in Reynolds-averaged Navier-Stokes (RANS) methods and Large Eddy Simulations (LES). They

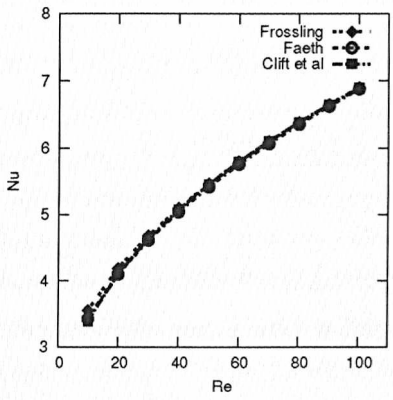

Figure 4.1: Comparison between different correlations for the Nusselt number.

use similar equations to Eq. (4.10) and (4.6) but with modified Nusselt, Nu^*, and Sherwood numbers, Sh^*. These models are used in many works such as (Abramzon and Sirignano, 1989; Bini and Jones, 2009; Castanet and Lemoine, 2007).

The first model, here defined as M1, is based on the energy equation for the gas phases. It assumes that all the heat conducted to the droplet goes to evaporation as the droplet temperature, T_d, is at the boiling value. The evaporation rate is

$$\dot{m}_{evap} = \frac{\pi \mu_g d}{Pr} Nu^* \ln(B_q + 1) \tag{4.32}$$

where the heat transfer number, B_q, based on the gas temperature, T_∞, is given by Eq. (4.11).

The modified Nusselt number, Nu^*, proposed by Abramzon and Sirignano, 1989, using the correlation of Frossling, 1938, is

$$Nu^* = 2 + 0.552 Re_k^{1/2} Pr^{1/3} F(B_q) \tag{4.33}$$

A correction factor through the function $F(B)$ is introduced to account for Stefan flow under combustion environments where the evaporation rates and the Stefan flow are higher than under inert environments.

$$\frac{1}{F(B)} = (1 + B)^{0.7} \frac{\ln(1 + B)}{B} \tag{4.34}$$

Different correlations for the modified Nusselt number are also proposed by Yuen and Chen, 1977, for water and methanol droplets in a range of $200 \leq Re \leq 2000$.

$$Nu^* = \frac{2 + 0.6 Re_k^{1/2} Pr^{1/3}}{1 + B} \tag{4.35}$$

Renksizbulut and Yuen, 1983, proposed a very similar correlation. Their experiments were performed for water, methanol and n-heptane droplets in a Reynolds number range of 25 to 2000.

$$Nu^* = \frac{2 + 0.6 Re_k^{1/2} Pr^{1/3}}{(1 + B)^{0.7}} \tag{4.36}$$

The second model, M2, is derived from the species balance equation for the gas phase and the droplet temperature is assumed below the boiling temperature. The mass fraction of vapour at the droplet interface is uniform and determined by the liquid-vapour equilibrium at the droplet temperature (Turns, 1996). The model assumes that the rate of the droplet evaporation is controlled by the diffusion process. The rate is calculated as

$$\dot{m}_{evap} = \frac{\pi \mu_g d}{Sc} Sh^* \ln(B_k + 1) \tag{4.37}$$

where the mass transfer number, B_k, is defined as in Eq. (4.3). The modified Sherwood number, Sh^*, proposed by (Abramzon and Sirignano, 1989) is

$$Sh^* = 2 + 0.552 Re_k^{1/2} Sc^{1/3} F(B_k) \tag{4.38}$$

Similarly to the Nusselt number, Yuen and Chen, 1977, proposed

$$Sh^* = \frac{2 + 0.6 Re_k^{1/2} Sc^{1/3}}{(1 + B_k)} \tag{4.39}$$

and the correlation proposed by Renksizbulut and Yuen, 1983, as

$$Sh^* = \frac{2 + 0.6 Re_k^{1/2} Sc^{1/3}}{(1 + B_k)^{0.7}}. \tag{4.40}$$

Differently from the correlations proposed for the Nusselt and Sherwood numbers, the correlations for the modified Nusselt and Sherwood differ significantly depending on the heat transfer number (B_q or B_k) and the Reynols number ranges. Differences of up to 120%, for the same transfer number B, are found for the correlations proposed by Abramzon and Sirignano, 1989, and Renksizbulut and Yuen, 1983, as shown in Fig. 4.2. The correlations obtained for n-heptane by Renksizbulut and Yuen, 1983, are used for the n-heptane test cases and the ones proposed by Abramzon and Sirignano, 1989, are used in the kerosene studies.

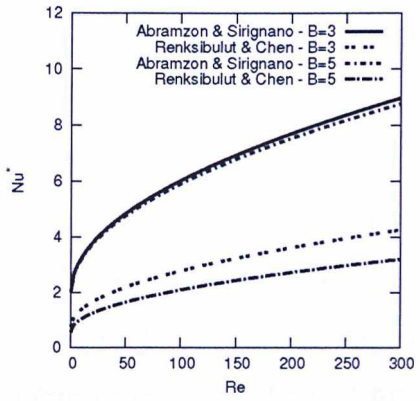

Figure 4.2: Comparison between different correlations for the modified Nusselt number.

Model M1 is appropriate when the evaporation is controlled by heat transfer ($T_d = T_{boil}$) and M2 when it is controlled by mass transfer ($T_d \leq T_{boil}$) (Lederlin and Pitsch, 2008). In reactive environments, the droplets reach saturation temperature in a very short time compared to the droplet lifetime and the assumption that $T_d = T_{boil}$ seems appropriate.

4.2.5 Gas-phase Properties

The evaporation models are strongly dependent on the transport properties of the gas which properties depend on the local temperature and species composition. The assumption of constant gas properties in the gas phase is very unrealistic and significantly affects the calculated evaporation rates. Furthermore, it is not evident which value of temperature and composition should be used.

Mixing rules are often used to calculate a reference value for temperature and mass fraction, T_r and Y_r respectively, in order to compute the transport properties. The most popular mixing rule is a linear combination of gas (T_g, Y_g) and vapour properties at the surface (T_d, Y_d) and is given by

$$T_r = T_d + A(T_g - T_d) \tag{4.41}$$

$$Y_r = Y_d + A(Y_g - Y_d) \tag{4.42}$$

where $0 \leq A \leq 1$. Yuen and Chen, 1976, proposed the value of $A = \frac{1}{3}$ commonly known as the $\frac{1}{3}$-rule and this is widely used. This weighting factor is most often used in modelling studies of droplet evaporation and combustion, however, Miller et al., 1998, found better agreement for $A = 0$ in cases of high temperature environments. A further uncertainty is the determination of T_g and Y_g as the gas distribution around the droplets is not homogeneous. In principle, these should be the conditions at infinity or at the flame front if single droplet combustion occurs, however, determination in practice is not so straight forward.

4.3 Test Cases

The test cases performed for *n*-heptane are summarised in Table 4.1. The first test case, in stagnant environment follows the characteristics of the experiments of (Nomura et al., 1996) and the others follow the computational tests of (Birouk and Al-Sood, 2010). The effects of droplet density on the evaporation rates are investigated and cases with 1 and 64 droplets are performed under laminar and turbulent inert and reactive environments.

Similar test cases are performed for kerosene as presented in Table 4.2. However, droplet density effects are investigated for cases with 1, 8, 27 and 64 droplets.

The droplet distribution inside the domain is as shown in Fig. 4.3. They are located in planes, regularly ordered and equally spaced.

Table 4.1: 3D n-heptane Test Cases

Section	Test	u_∞ [m/s]	T_∞ [K]	Drops	d [μm]	Δx [μm]	p [atm]
5.3	1-drop Stagnant	0	556	1	794	78	5
5.3	1-drop Inert Laminar	2	1350	1	100	8	5
5.3	64-drop Inert Laminar	2	1350	64	100	8	5
5.3	1-drop Inert Turbulent	2	1350	1	100	8	5
5.3	64-drop Inert Turbulent	2	1350	64	100	8	5
5.3	1-drop Reacting Laminar	2	1350	1	100	8	5
5.3	64-drop Reacting Laminar	2	1350	64	100	8	5
5.3	1-drop Reacting Turbulent	2	1350	1	100	8	5
5.3	64-drop Reacting Turbulent	2	1350	64	100	8	5

Table 4.2: 3D Kerosene Test Cases

Section	Test	u_∞ [m/s]	T_∞ [K]	Drops	d [μm]	Δx [μm]	p [atm]
5.4	1-drop Inert Laminar	1	1530	1	60	5	40
5.4	8-drop Inert Laminar	1	1530	8	60	5	40
5.4	27-drop Inert Laminar	1	1530	27	60	5	40
5.4	64-drop Inert Laminar	1	1530	64	60	5	40
5.4	1-drop Inert Turbulent	1	1530	1	60	5	40
5.4	8-drop Inert Turbulent	1	1530	8	60	5	40
5.4	27-drop Inert Turbulent	1	1530	27	60	5	40
5.4	64-drop Inert Turbulent	1	1530	64	60	5	40
5.4	1-drop Reacting Laminar	1	1530	1	60	5	40
5.4	8-drop Reacting Laminar	1	1530	8	60	5	40
5.4	27-drop Reacting Laminar	1	1530	27	60	5	40
5.4	64-drop Reacting Laminar	1	1530	64	60	5	40
5.4	1-drop Reacting Turbulent	1	1530	1	60	5	40
5.4	8-drop Reacting Turbulent	1	1530	8	60	5	40
5.4	27-drop Reacting Turbulent	1	1530	27	60	5	40
5.4	64-drop Reacting Turbulent	1	1530	64	60	5	40

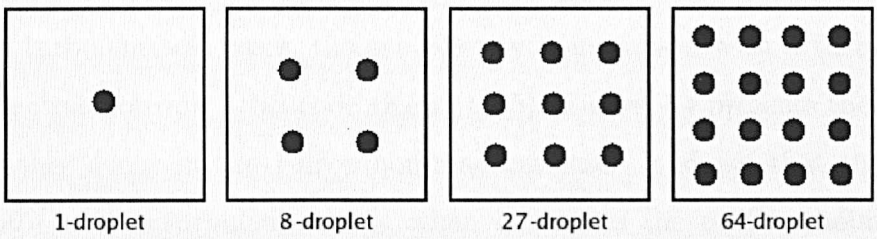

Figure 4.3: Slice of the domain with the droplet arrangements of the evaporation test cases for n-heptane and kerosene.

4.4 n-Heptane

Different test cases involving n-heptane droplet and droplet arrays are performed as described in Table 4.1. In order to evaluate the accuracy of the DNS, the results

for single n-heptane droplets in inert environments are compared to available experimental data (Nomura et al., 1996) and to other computational results (Birouk and Al-Sood, 2010). Further analysis is considered for reactive environments and for droplet arrays. The results of all the test cases are finally compared to the two well known models commonly used in RANS methods and LES, as introduced in Section 5.2.

The first test case is performed in a stagnant and inert environment at 556 K. The boundary conditions used are symmetry in all directions. The domain simulated is discretised by 128^3 nodes with a grid spacing of $\Delta x = 78\mu$m and with one kerosene droplet of initial size $d_0 = 794\mu$m located at the centre of the domain, such as in the experiments of Nomura et al., 1996.

In the laminar and turbulent cases, droplet arrays are simulated in inert and reactive environments with high inflow temperature of 1350 K. The droplet arrays are organised in infinite planar layers with thicknesses of one and four droplets. The droplet mass loading varies from 0.3 to 15.0 $\mathrm{kg}_{fuel}/\mathrm{m}^3$ representing volume fractions from approximately 0.06% to 3.0%. The boundary conditions used are inflow/outflow in one direction and periodic in the other directions. The domain is discretised by 128^3 nodes with a grid spacing of $\Delta x = 8\mu$m and includes 1 or 64 kerosene droplets of initial size $d_0 = 100\mu$m. In all the cases, the droplets are assumed to be at saturation conditions.

In the turbulent test cases, the gas velocity is initialised with a turbulent field from a spectral isotropic DNS code (Kerr, 1985). Figure 4.4 presents the turbulent kinetic energy decay in the 1-drop non-reacting case. It shows that the flow has around 60% of the turbulent energy when it reaches the outflow boundary. In the simulations, the Taylor microscale is 0.17 mm and the associated Kolmogorov microscale is 25 μm, equivalent to approximately $3\Delta x$. Due to the character of the DNS, full scale separation cannot be realised and the computed integral length scale, ℓ, is relatively close to the Taylor length scale. This should not unduly affect computed results since large scale motion is expected to move all particles equally and fuel concentrations and temperature distribution in inter-droplet space should be relatively invariant to the size of ℓ. The ratio between the integral scale and the

droplet diameter is $\ell/d_0 = 2.0$ and thus of the same order as in the experiments of Birouk et al., 2000. In order to sustain turbulence during the droplet lifetime, turbulence is super-imposed to the convective inflow. The mean inflow velocity that represents the relative velocity between droplets and surrounding gas is 2 m/s as in the simulations of Birouk and Al-Sood, 2010, and this value is used for all laminar and turbulent cases. The Reynolds number based on the gas-phase properties and the Taylor length scale is approximately 100.

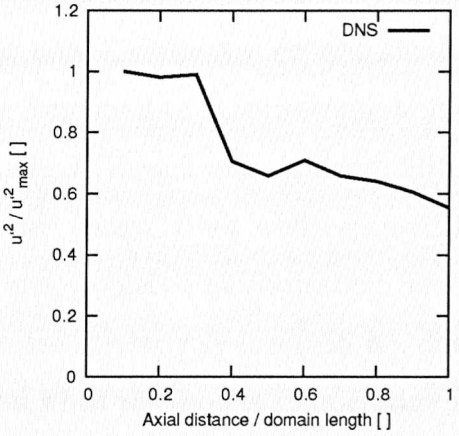

Figure 4.4: Turbulent kinetic energy for the 1-drop turbulent non-reacting case.

The gas phase is initialised with the same conditions as the inflow which consists of pure air at high temperature (556 K in the stagnant case and 1350 K in the convective cases) and high pressure (5 bar). The liquid fuel is assumed at 437 K with $\rho_l = 544$ kg/m^3, $\sigma = 0.6\ 10^{-2}$ N/m, $\mu = 1.4\ 10^{-4}$ Pa.s and $h_{fg} = 263$ kJ/kg. A temperature gradient from the gas temperature to the n-heptane saturation temperature is initially imposed close to the droplets. This initialisation has some effect on the evaporation rates during an initial transient of approximately 3 ms in the convective cases, and the transition needs to be considered when interpreting the results of the DNS.

All computations are carried out for non-reacting, i.e. purely evaporating, and reacting flows. The chemistry is approximated by the 18-step and 21-species mechanism for hydrocarbon combustion of Liu et al., 2004, described in Appendix A. The

hot air injected evaporates the droplets and, in the reactive cases ignition occurs once appropriate conditions (vapour fraction concentration and temperature) are reached. The stoichiometric mixture fraction of n-heptane is $f_{stoic} = 0.0621$.

4.4.1 Evaporation Rates

The evaporation rates of n-heptane are investigated in detail. The results for stagnant and convective cases are compared to available numerical and experimental data and the resuls are compared to the models previously described in Section 4.2.

The stagnant case has been investigated experimentally and numerically. Therefore, the DNS results are compared to experimental data (Nomura et al., 1996) and to another numerical method (Birouk and Al-Sood, 2010). Figure 4.5 shows that the initial droplet diameter decay is not well captured by the DNS. This is due to the assumption that the droplet is at saturation temperature. As the ambient temperature in this test case is relatively low (556 K), different from the convective cases, the transient period when the droplet temperature increases until it reaches a constant value is significant. However, at a later stage when the droplet temperature reaches the maximum value, the results of the DNS accurately represent the decay of the droplet diameter as measured in the experiments. In order to compare the slopes the DNS results have been plot with a shift in the x-axis of 2 s/mm^2. The droplet diameter variation follows the well known d^2-law (Godsave, 1953).

The results of the stagnant test case are also compared to the two models M1 and M2 (see Fig. 4.6) with $Nu^* = Sh^* = 2$. The main assumptions are single-droplet evaporation in equilibrium with constant droplet temperature and uniform properties of the gas phase. The definition of appropriate properties and the gas-phase temperature is essential to guarantee the predictive capabilities of evaporation models. As in RANS and LES, only mean (or filtered) values of the temperature and composition are available, the "ambient" temperature needed as input to B_q is taken to be the mean (or filtered) value $T_\infty = \bar{T}$, and Y_g is used to define the gas properties. Here, it is assumed that a RANS or LES cell is of the size of the computational domain and $\bar{T}$ denotes the averaged DNS gas phase temperature.

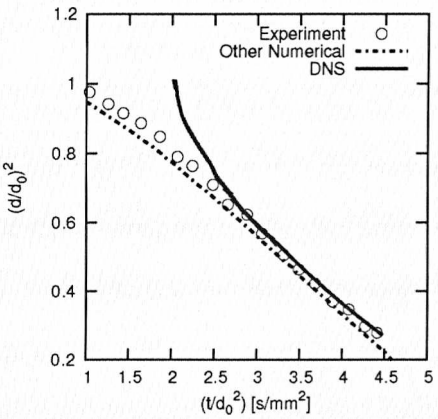

Figure 4.5: Comparison of the individual droplet diameter evolution in time for the 1-droplet stagnant case with other numerical (Birouk and Al-Sood, 2010) and experimental (Nomura et al., 1996) works.

Two different ways of evaluating the models properties are investigated: Firstly, the 1/3-rule, $A = 1/3$, and secondly $A = 0$ which is equivalent to the assumption that the gas is pure vapour at saturation conditions.

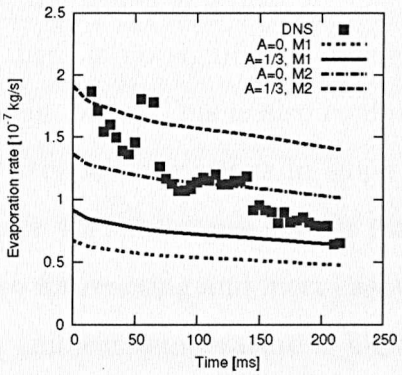

Figure 4.6: Comparison of the DNS results with models M1 and M2 for the stagnant test case using $T_\infty = \bar{T}$.

The DNS results are within the values predicted by the two models for the entire computation. Initially the DNS rates are between the values of M2 for $A = 0$ and $A = 1/3$. Then, the model M2 with $A = 0$ seems to accurately capture the DNS rates, and in the last 50 ms of the simulations, the rates are between the values predicted by model M2 with $A = 0$ and M1 with $A = 1/3$. This comparison shows that no model with gas properties obtained through the mixing rule seems to capture

the rates accurately during the entire droplet lifetime.

As there is no available experimental data for the laminar and turbulent cases under high pressure for n-heptane, the DNS results are compared to the numerical results of Birouk and Al-Sood, 2010. Figure 4.7 shows that in the DNS, the square of the droplet diameter for the 1-droplet cases also follows the d^2-law. This is valid for all the 1-droplet cases and also for the average diameter in the 64-droplet test cases.

Moreover, the DNS results for the laminar case show similar slope to the results of Birouk and Al-Sood, 2010. The present DNS, however, does not simulate the initial period of droplet heat up. The other numerical results show a relatively constant diameter during the initial period of approximately 3 ms (where only droplet heating occurs with no significant evaporation). In the DNS, as the droplet is considered already at saturation temperature, the decrease in the diameter occurs from the begining of the simulations. This initial period is short compared to the droplet lifetime. In order to better compare the evaporation rates, the DNS results have been plotted with a shift in the x-axis of 3 ms.

Fig. 4.7 suggests that there is no significant difference in the diameter variation for laminar and turbulent cases. This is also confirmed by the work of Birouk and Al-Sood, 2010, where very low variations in slope are observed for turbulent intensities up to 60%. Figure 4.8 shows very similar evaporation rates for laminar and turbulent cases and also for reacting and inert cases. This indicates that under these conditions where the ambient temperature is high, neither turbulence or the presence of combustion seem to affect the evaporation rates in the low droplet density cases. However, droplet density affects significantly the rates, and the droplet lifetime in the 64-droplet cases is approximately 20% higher than in the 1-droplet cases. The maximum evaporation rate for the 1-drop reactive laminar case is used as reference to the normalised rates.

The low dependence on turbulence as indicated by Fig. 4.9 implies that no correlation between the evaporation rates and the subgrid kinetic energy is found. The subgrid kinetic energy denotes the average fluctuation within the computational domain. This agrees with the experiments performed by Birouk et al., 2000, where the

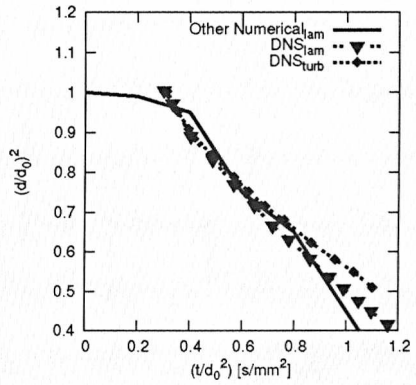

Figure 4.7: Individual droplet diameter squared as function of time for the 1-droplet non reactive case.

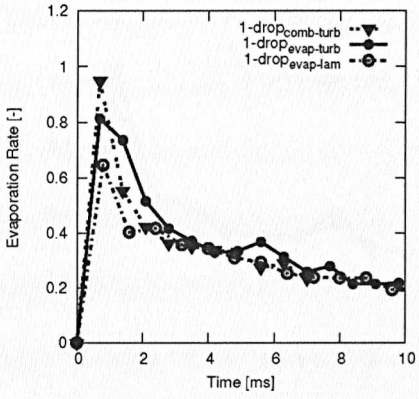

Figure 4.8: Mean evaporation rate for the 1-droplet test cases.

relative effects of turbulence decreased when droplet evaporation became intense. In these cases -as in the present configurations- the Stefan flow is significant and forms a "protective" layer around the droplets and turbulent effects are limited to the dispersion of the fuel vapour away from the droplet surface.

In the 64-droplet cases, no clear differences in the evaporation rates are observed for the droplets located in each row. Droplets located at a lower position present similar evaporation rates to the droplets in the highest positions even in the case of combustion, as shown in Fig. 4.10. This is due to the fact that the flame propagates between the droplet layers and the heat conducted to the droplets is approximately the same in all layers.

In order to assess the evaporation models, the evaporation rates per droplet are

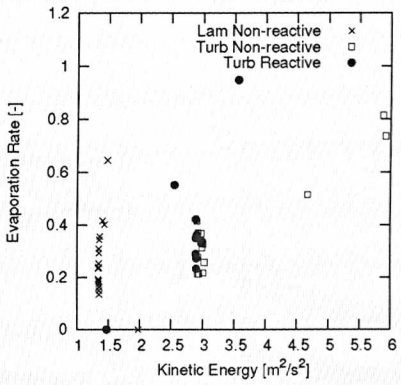

Figure 4.9: Evaporation rate versus the subgrid kinetic energy for the 1-droplet cases.

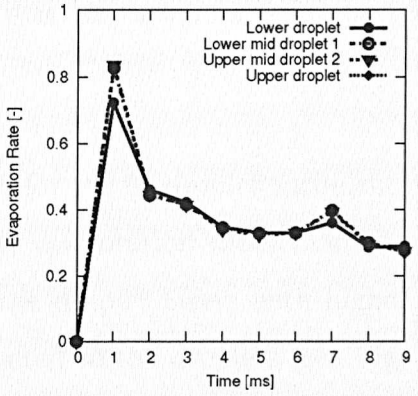

Figure 4.10: Evaporation rate for droplets in different rows for the 64-droplet case with turbulence and reaction.

compared to the two models M1 and M2. These models are assessed here using the correlations for the modified Nusselt and Sherwood number as proposed for n-heptane by Renksizbulut and Yuen, 1983.

As discussed before, an initial transient period is identified. During the first 3 ms, the evaporation rates are strongly affected by the initialisation of the temperature in the domain. Therefore, this transient period should not be considered in the comparison of the DNS rates with the models.

Figure 4.11 shows a comparison between the results of the DNS and the predictions of the models for laminar and turbulent inert cases for the 1-droplet case. The models seem to present very similar results, however, the best results are given

for $A = 0$ in both laminar and turbulent cases. For these approximations, the differences are around 30%.

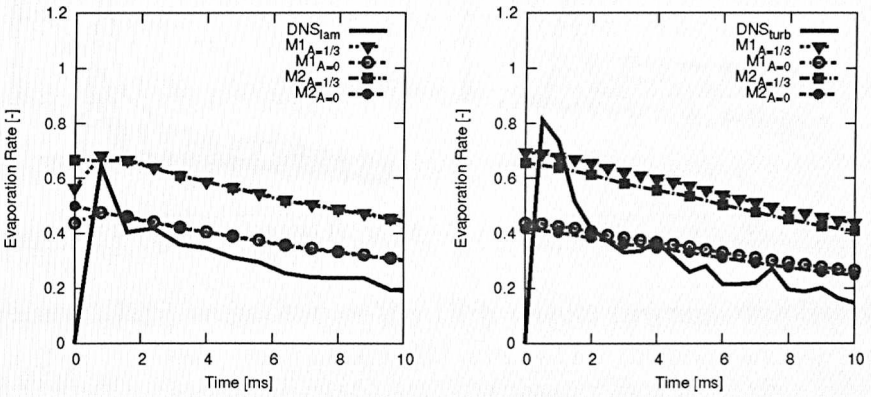

Figure 4.11: Comparison of the DNS results with models M1 and M2 for the non-reactive turbulent 1-droplet test case using $T_\infty = \bar{T}$.

The results of the DNS for the 64-droplet turbulent cases show that the reactive case presents much higher evaporation rates than the inert one. This is due to the flame front between the droplet layers with higher temperature and therefore increasing the heat conducted to the droplets (see Fig. 4.12). As for the 1-droplet cases, the models present very similar values and, especially for $A = 0$, they capture the evaporation rates well. Moreover, because the filtered temperature increases in the reactive case, the models also capture the trend of higher rates for the reacting case. The differences between the models and the DNS results are lower than 5%.

It is expected that a "correct" choice of properties may improve the predictive capabilities of M1 and M2. As the heat transfer to the droplet occurs at the droplet surface, relevant properties should be obtained from close to the droplet. A shell around the droplet ($\delta_0 \approx \Delta x$) is defined, and average temperature and composition within this shell are calculated. Fig. 4.13 demonstrates that M1 gives very good predictions for both 1 and 64-droplet cases in reactive environments and non-reactive cases with errors around 2%. Even the transients are better captured and a "shell" model seems to be very appropriate for modelling droplet evaporation under the conditions considered here. Unfortunately, RANS and LES cannot provide such

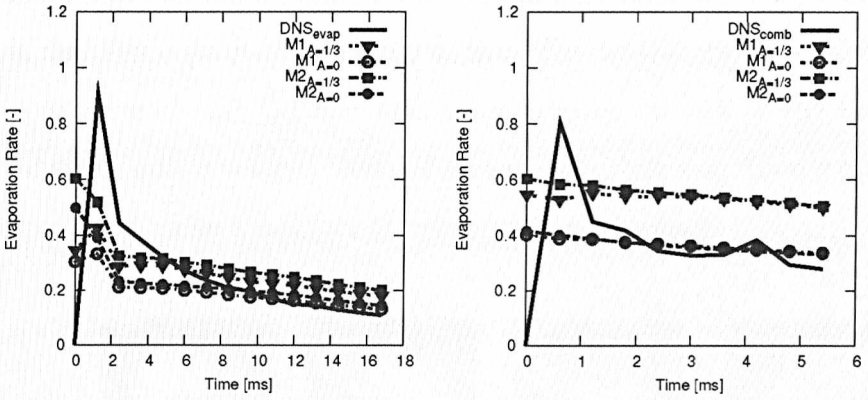

Figure 4.12: Comparison of the DNS results (average droplet evaporation rate) with models M1 and M2 for the non-reactive and reactive turbulent 64-droplet test cases using $T_\infty = \bar{T}$.

detailed information and future efforts will be directed towards a better estimation of reference properties not at, but close to the surface of the droplets.

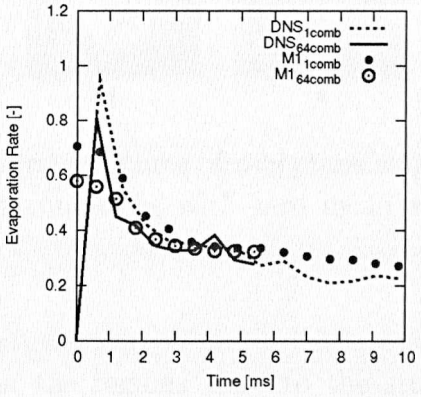

Figure 4.13: Comparison of the DNS results with model M1 using properties averged within a shell around the droplet for the reactive turbulent 1- and 64-droplet test cases.

4.4.2 Reactive cases

Figure 4.14 shows instantaneous flame pictures of an experiment of a single droplet combustion of n-heptane in an isotropic turbulent environment with no mean velocity ($u_\infty = 0$) at ambient conditions. Figure 4.15 shows contourplots of the DNS

of the 1-droplet turbulent case performed in this work with $u_\infty = 2$ m/s. In both figures, the flame position changes in time due to the droplet change in size and mostly because of turbulence. The instantaneous profiles of the flames differ because of mean inflow velocity and differences in turbulence. However, they are quite similar and the flame envelopes the droplet in both cases.

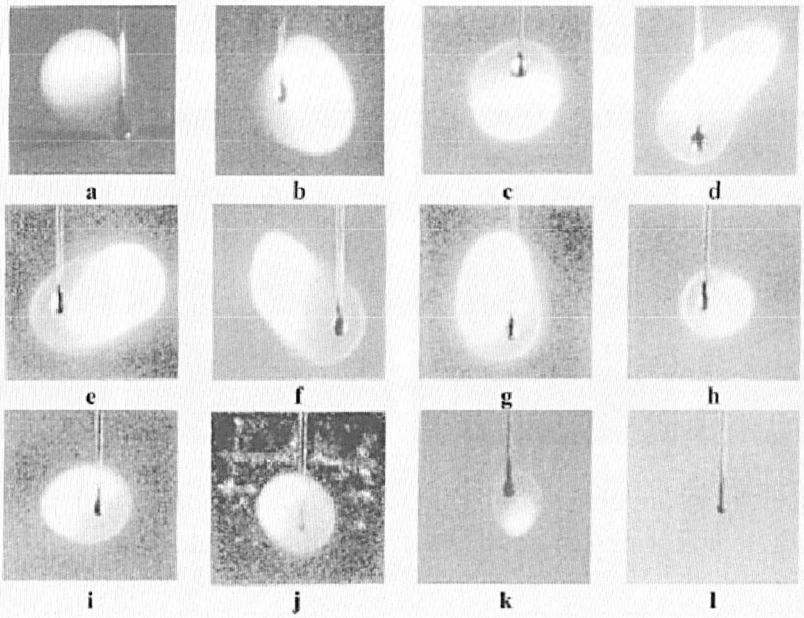

Figure 4.14: Instantaneous pictures of n-heptane single droplet flame under turbulent conditions with zero mean velocity (Birouk et al., 2000).

The reactions occur in the regions close to the stoichiometric value $f_{stoic} = 0.0621$. The flame thickness of a standard hydrocarbon at ambient conditions is $\delta_L^0 \approx 0.5$ mm (Poinsot and Veynante, 2005). In the DNS, the mesh size is $\Delta x = \delta_L^0/60$ so the flame is expected to be well resolved.

Figure 4.16 shows the concentration of CO at an initial burning stage and at a later stage. The highest concentration occurs around the stoichiometric mixture fraction. Moreover, no strong correlation with mixture fraction is observed as local extinction is present.

Figure 4.17 shows the H_2O and OH concentrations of the 64-droplet turbulent case. Single droplet combustion occurs for the 1-droplet case where the distance

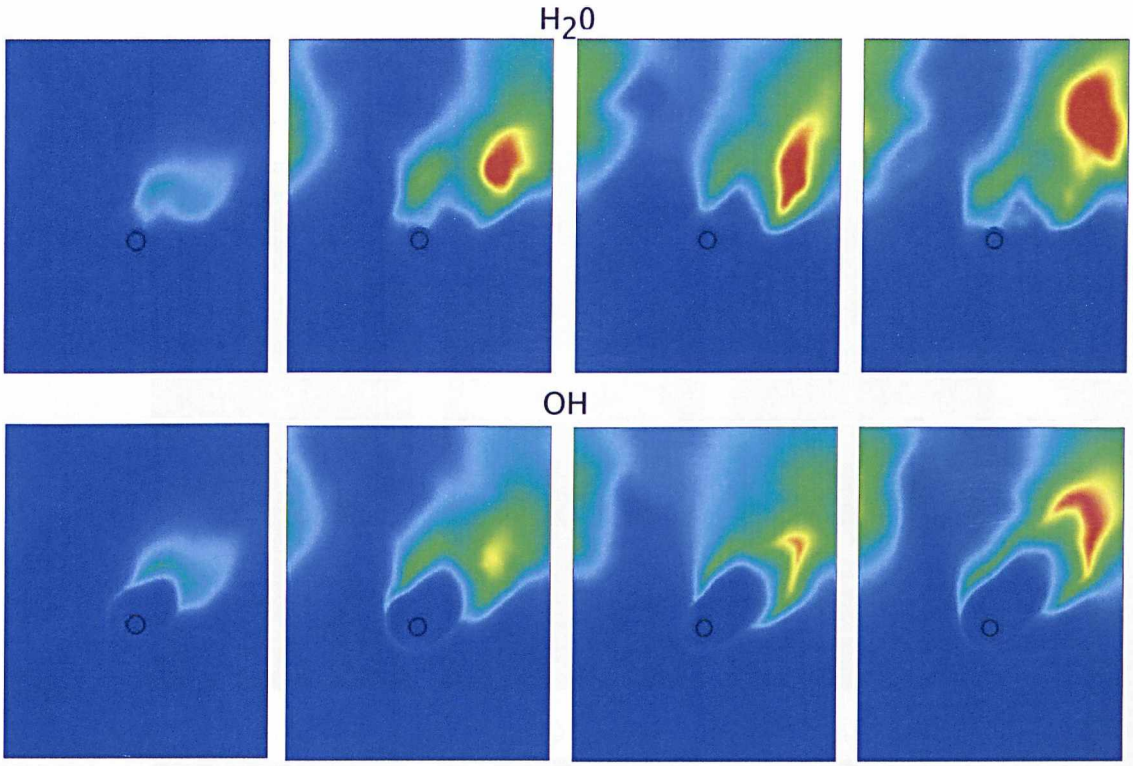

Figure 4.15: Instantaneous H_2O and OH contourplots of the 1-droplet turbulent case at different time steps (mean inflow velocity of 2 m/s).

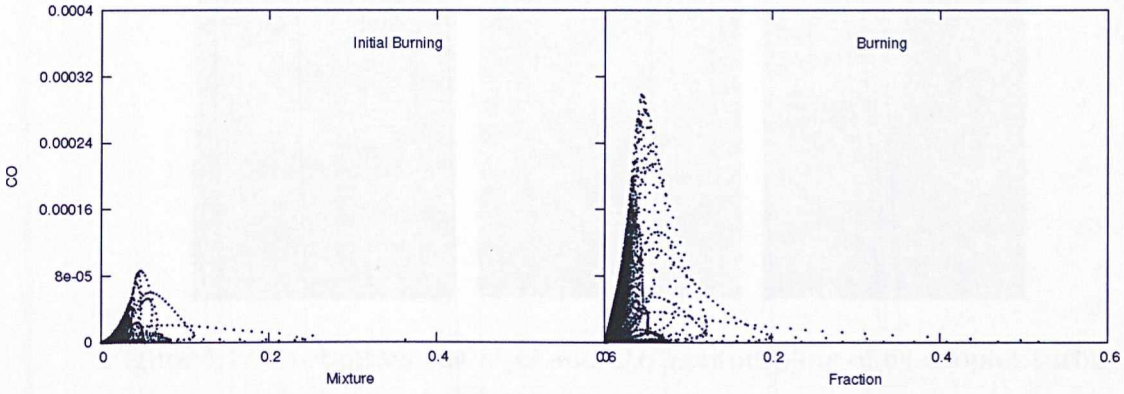

Figure 4.16: Scatter plots of CO concentration at different time steps for the 1-droplet case.

between the droplets is around $10d_0$ (see Fig. 4.15), however, for the 64-droplet case, where the droplet spacing is lower than $3d_0$, group combustion is observed. The individual flames merge and often remain between the droplet layers, especially

the lower layers. The flame does not stabilise and local extinction is frequently observed.

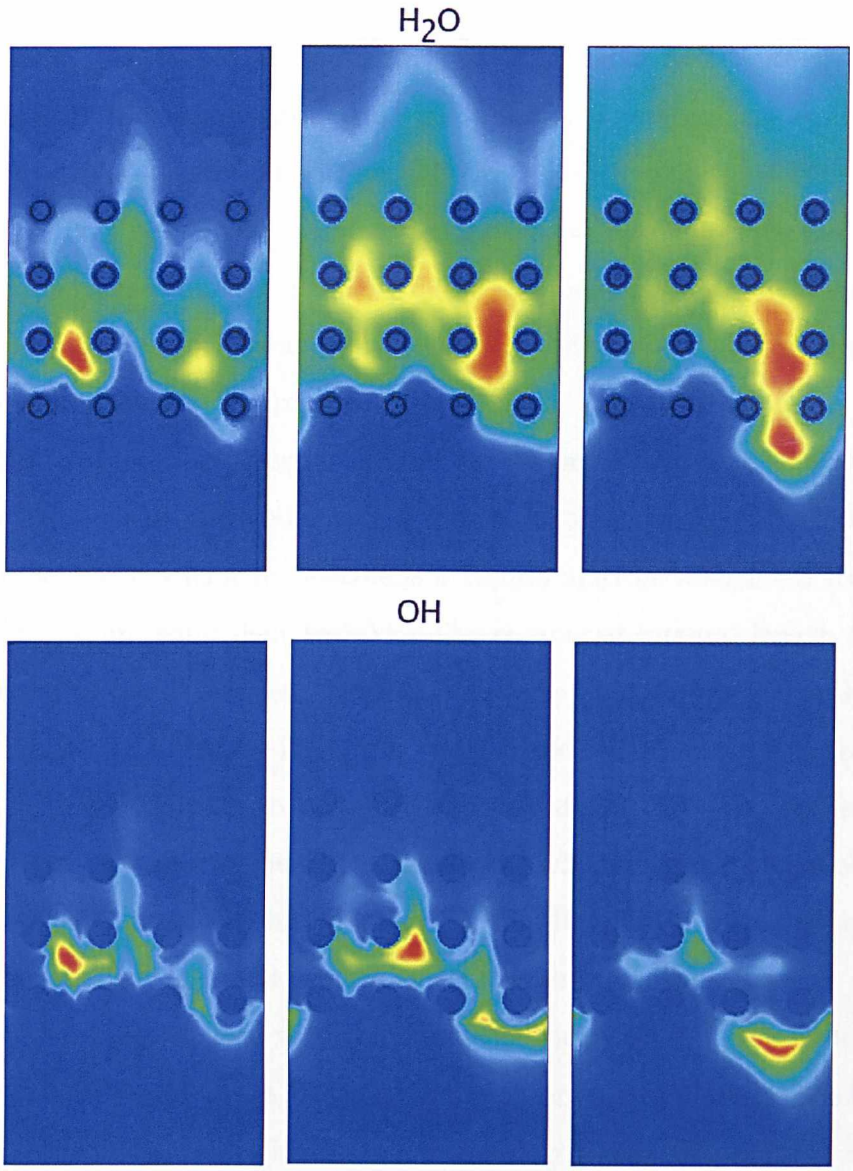

Figure 4.17: Instantaneous H_2O and OH contourplots of 64-droplet turbulent case at different time steps.

4.5 Kerosene

The configuration for the kerosene test cases is similar to the n-heptane test cases. However, as there is no available data to compare with and because of limited

practical application of non-convective environments, no stagnant simulations are performed. Therefore, droplet arrays are simulated in inert and reactive environments as shown in Table 4.2. The droplet arrays consists on one, two, three and four droplets layers. The droplet mass loading varies from 0.3 to 21.3 kg_{fuel}/m^3 resulting in volume fractions from around 0.04% to 3.0%. The boundary conditions are: inflow/outflow in one direction and periodic in the other directions. The domain is discretised by 128^3 nodes with a grid spacing of $\Delta x = 5\mu$m and includes 1, 8, 27 or 64 kerosene droplets of initial size $d_0 = 60\mu$m. As before the droplets are assumed to be at saturation conditions and all the heat transferred to the droplets therefore results in evaporation of the droplets.

Turbulent and laminar cases are simulated. As previously described, the gas velocity is initialised with a turbulent field from a spectral isotropic DNS code in the turbulent cases. The Taylor microscale is 0.12 mm and the associated Kolmogorov microscale is 15 μm, equivalent to $3\Delta x$. The computed integral length scale, ℓ, is relatively close to the Taylor length scale. The ratio between the integral scale and the droplet diameter is $\ell/d_0 = 2.5$ and is of the same order as in the experiments of Birouk et al., 2000. In order to sustain turbulence during the droplet lifetime, turbulence is super-imposed to the convective inflow which has a mean inflow velocity of 1 m/s in both laminar and turbulent cases. The Reynolds number is around 100, based on the gas-phase properties and the Taylor length scale.

The gas phase is initialised with the same conditions as the inflow which consists of pure air at high temperature (1530 K) and high pressure (40 bar). The liquid fuel is assumed to be at 332.8 K with $\rho_l = 770$ kg/m^3, $\sigma = 2.0\ 10^{-2}$ N/m, $\mu = 8.2\ 10^{-4}$ Pa.s and $h_{fg} = 310$ kJ/kg. A temperature gradient from the gas temperature to the kerosene saturation temperature is initially imposed close to the droplets. This initialisation has a strong effect on the initial evaporation rates during an initial transient of approximately 50-100 μs and should be considered when interpreting the results of the DNS.

All computations are carried out for non-reacting and reacting flows. The chemistry of kerosene is approximated by the 4-step and 7-species mechanism for hydrocarbon combustion of Jones and Lindstedt, 1988, described in Appendix A.

4.5.1 Evaporation Rates

The evaporation rates per droplet of kerosene are investigated here by comparing the results from the DNS with the two models, M1 and M2, using the correlations for the modified Nusselt and Sherwood number as proposed by Abramzon and Sirignano, 1989.

Figure 4.18 demonstrates that the square of the average droplet diameter varies linearly with time independent of the droplet loading. The droplet lifetime can now be derived from the well known d^2-law for all cases, independent of the existence of a flame and the flame regime. For the 1 and 8-drop cases, the average droplet lifetime is around 1.25 ms while for the most dense case with 64 droplets, it is approximately 1.60 ms.

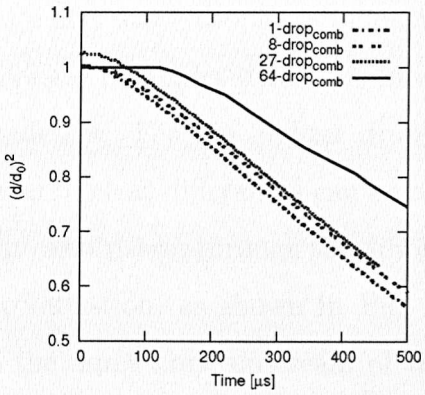

Figure 4.18: Individual droplet diameter squared as function of time.

In contrast, it does not seem that under these high temperature conditions the evaporation rates, and thus the droplet lifetimes, are much affected by the presence of turbulence, neither by the presence of combustion. The evaporation rates for the 8-drop cases are shown in Fig. 4.19, the transients in the laminar case are somewhat different due to differences in initialisation, but general trends and peak rates differ by a mere 20% after approximately 200 μs when ignition of the gas-vapour mixture occurs. As in the n-heptane cases, the maximum evaporation rate for the 1-drop non-reactive laminar case is used as a reference value for normalisation.

The high inflow temperature of 1530 K sustains high evaporation rates even in

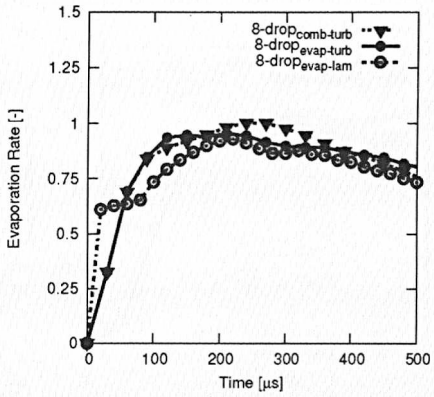

Figure 4.19: Mean evaporation rate per droplet for the 8-droplet test cases.

the inert cases and this leads to the relatively small differences. It is also noticed that there are no significant variations in the evaporation rates of the different droplets, and droplet evaporation rate of a single droplet is independent of its position within the droplet array. This changes if droplet density is increased and droplet spacing falls below 10 droplet diameters. For the highest droplet loading (and a droplet spacing of 5 droplet diameters), clear differences can be observed due to a reduction of the gas phase temperature as it passes through the droplet array. This is somewhat amplified in the case of combustion, as shown in Fig. 4.20, due to the presence of group combustion and the flame zone upstream of the array. This is a highly transient phenomenon, the mixture is fully burning after approximately 240 μs, and this induces a clear acceleration of the evaporation rate especially of droplets in the first row.

As observed in Fig. 4.19, turbulence does not seem to have significant effects on evaporation rates under any of the conditions considered here. As in the convective cases for the *n*-heptane, no correlation between the evaporation rates and the subgrid kinetic energy is noted from Fig. 4.21, where the subgrid kinetic energy denotes the average fluctuation within the computational domain. As mentioned in the *n*-heptane cases, this confirms that the Stefan flow is significant and forms a "protective" layer around the droplets and turbulent effects are limited to the dispersion of the fuel vapour away from the droplet surface. It can therefore be assumed that all further conclusions are equally valid for laminar and turbulent flows.

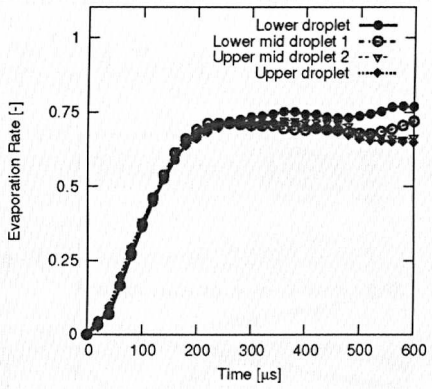

Figure 4.20: Evaporation rate for droplets in different rows for the 64-droplet case with turbulence and reaction.

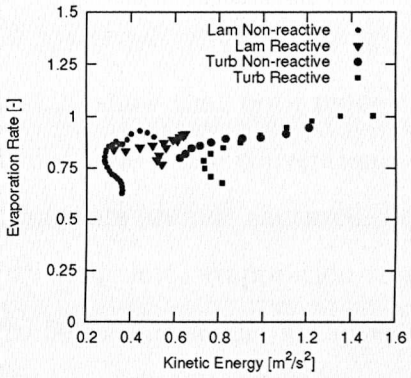

Figure 4.21: Evaporation rate versus the subgrid kinetic energy for the 8-droplet cases.

The DNS results of the 8-droplet and of the 64-droplet cases are compared with results obtained using models M1 and M2. Based on Fig. 4.29, the 8 droplet case may represent single droplet evaporation and combustion and good agreement with standard models can be expected, while the performance of the models for the 64 droplet case is less certain.

In order to compare the DNS results with the models M1 and M2 the "ambient" temperature needed to evaluate B_q and the properties is taken as the mean (or filtered) value $T_\infty = \bar{T}$, and $\bar{Y}_g$ is used to define the gas properties. Here, it is also assumed that a RANS or LES cell is of the size of our computational domain and $\bar{T}$ denotes the averaged DNS gas phase temperature. The temperature evolution in

time is shown in Fig. 4.22. Two different ways of evaluating the model properties are investigated: $A = 1/3$ and $A = 0$.

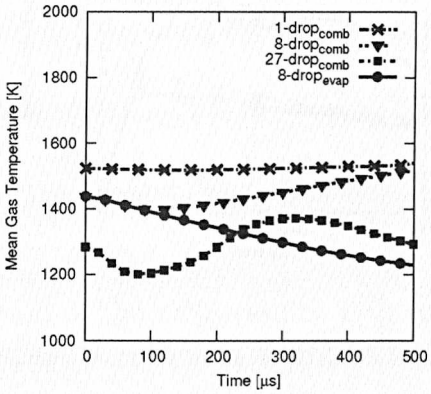

Figure 4.22: Filtered temperature.

The results in Figs. 4.23-4.25 show that both models do not predict the evaporation rate satisfactorily at any time if the conventional 1/3-rule is used. It is not surprising that the initial transients are not captured, however, even at later times during the linear decay of d^2 with time, evaporation rates are considerably underpredicted by between 30% to 50%. The model M1 gives slightly better results, but both models seem unsuited for modelling evaporation under engine like conditions. However, both models perform much better when setting $A = 0$. Now, deviations from DNS are between 1% and 22%, with M1 generally being closer to the DNS data. In addition M2 does not seem to capture the decay of the evaporation with time appropriately for high droplet densities with combustion, as can be seen in Fig. 4.25.

In reacting flows, it can be argued that conditions at infinity should be approximated by conditions in the flame since volume averaging does not capture local conditions correctly. Figures 4.26 and 4.27 compare DNS with modelled evaporation rates, using the 1/3-rule and approximating T_g and Y_g from compositions averaged along the flame contours where mixture fraction is close to stoichiometric. T_∞ is set to the maximum flame temperature. Results for M1 and M2 using filtered values are also included in the figures for better comparison. Due to the assumption of higher temperatures around the droplets, modelled evaporation rates increase,

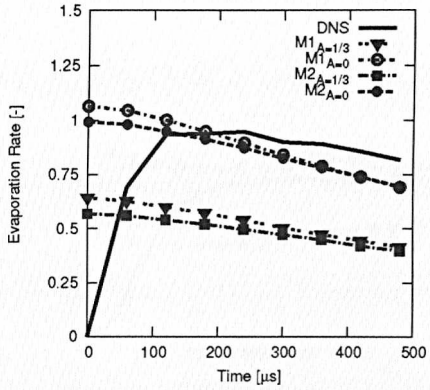

Figure 4.23: Comparison of the DNS results with models M1 and M2 for the non-reactive turbulent 8-droplet test case using $T_\infty = \bar{T}$.

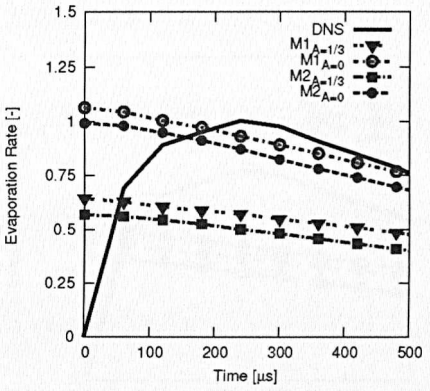

Figure 4.24: Comparison of the DNS results with models M1 and M2 for the reactive turbulent 8-droplet test case using $T_\infty = \bar{T}$.

but evaporation rates are still underpredicted by 20% in the 8 droplet case. Due to the logarithmic dependence of B_q on temperature, the temperature adjustment does not change the results of M1 much and it does not really affect the results of M2. However, the change in reference temperature and composition changes the properties more significantly and leads to the observed differences in M1 and M2. The good agreement in the 64 droplet case is somewhat fortuituous since models for single droplet combustion should overpredict group combustion and the general trend of underprediction is thus counteracted by the existence of group evaporation and combustion.

As for the n-heptane cases, we may conclude that in particular a "correct" choice

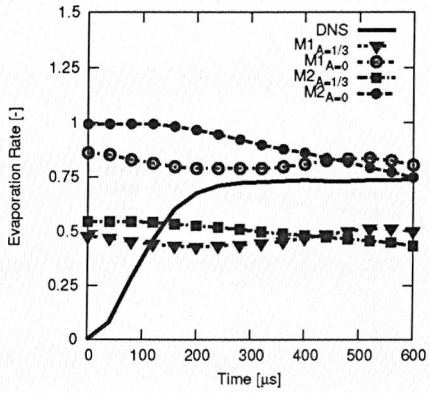

Figure 4.25: Comparison of the DNS results (average droplet evaporation rate) with models M1 and M2 for the reactive turbulent 64-droplet test case using $T_\infty = \tilde{T}$.

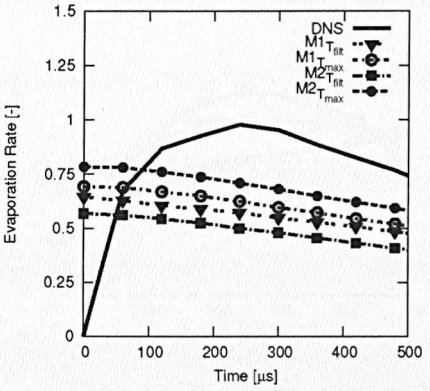

Figure 4.26: Comparison of the DNS results with models M1 and M2 for the reactive turbulent 8-droplet test case using $A = \frac{1}{3}$.

of properties may improve the predictive capabilities of M1 and M2. A shell around the droplet ($\delta_0 \approx \Delta x$) is again defined, and average temperature and composition within this shell are calculated. Fig. 4.28 demonstrates that M1 with reference properties from this shell gives very good predictions independent of reaction and of the combustion regime (errors are around 2%). The transients are also much better captured and this confirms that a "shell" model is appropriate for modelling droplet evaporation under the conditions considered here.

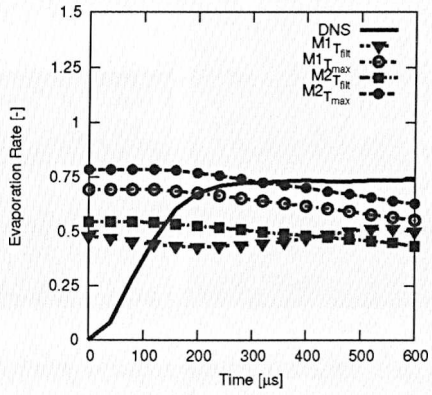

Figure 4.27: Comparison of the DNS results with models M1 and M2 for the reactive turbulent 64-droplet test case using $A = 1/3$.

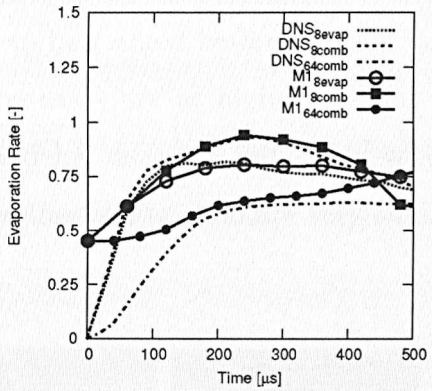

Figure 4.28: Comparison of the DNS results with model M1 using properties averged within a shell around the droplet for the reactive turbulent 8- and 64-droplet test cases.

4.5.2 Reactive cases

Figure 4.29 shows snapshots of the temperature fields for droplet evaporation in turbulent reacting flows with 1, 8, 27 and 64 drops in the domain. It is evident that droplet number density strongly affects the combustion process. Single droplet combustion occurs for larger droplet spacings, however, there is a clear transition to group combustion once the droplet spacing falls below 5 initial droplet diameters. For these rather dense sprays, group combustion can be observed with one leading flame zone upstream of the droplet arrays. The flame zone downstream of the arrays is less pronounced due to the relatively rich mixture in this region.

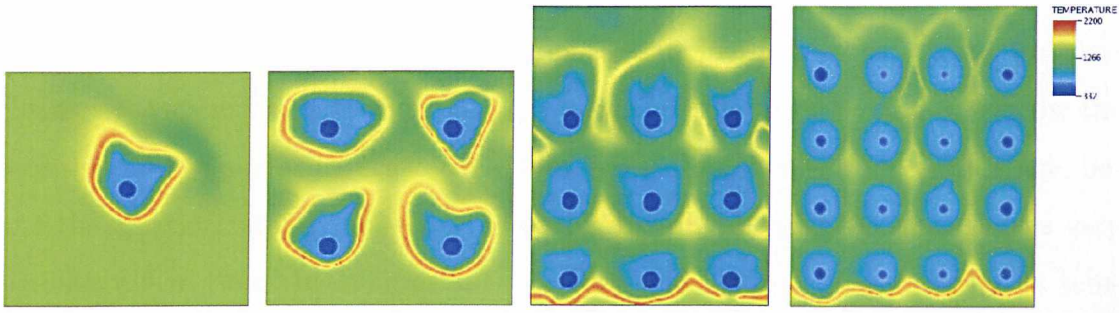

Figure 4.29: Instantaneous temperature profiles for the 1, 8, 27 and 64-droplet cases with turbulent inflow and combustion.

The ignition delay of the kerosene tests is lower than in the n-heptane tests. This can be partially explained by the simplicity of the kerosene mechanism, since no intermediate species need to be formed before ignition occurs. However, the main reason is that the kerosene cases are at higher pressure and higher temperature. As shown in Fig. A.1, the delay decays significantly with increasing pressure and temperature. The flame profiles of Fig. 4.30 are very similar to Fig. 4.14 where the flame surrounds the droplet.

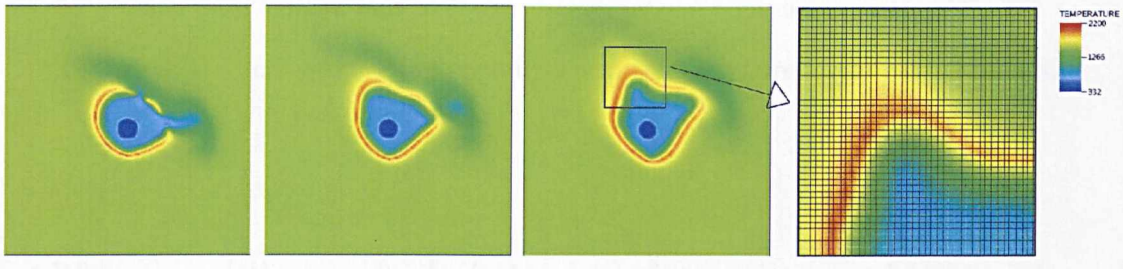

Figure 4.30: Temperature profiles at different time steps for the 1-droplet reacting case.

In the turbulent cases, the flame profiles change significantly in time. As can be observed from Fig. 4.30, the shape of the flame is modified by turbulence and even local extinction occurs (see first left figure). The number of cells across the flame varies in time and space, going from around 4 to 10 as shown in Fig. 4.30. As mentioned before, the flame thickness of a standard hydrocarbon at ambient conditions is $\delta_L^0 \approx 0.5$ mm (Poinsot and Veynante, 2005) and in these simulations,

the mesh size is around $\delta_L^0/100$.

As in the n-heptane cases, the reactions occur in the regions around the stoichiometric vapour fraction which is $f_{stoic} = 0.0676$. Figures 4.31 and 4.32 show the enthalpy and temperature scatter plots for the 1-droplet case at an early stage, before the reactions start, and when the droplet is fully burning. Both variables vary significantly in time. It is important to notice that, as expected, the peak in temperature in the burning stage occurs for the stoichiometric vapour fraction value. Furthermore, the enthalpy profile also changes and becomes linear with mixture fraction at the later stage as commonly observed in combustion cases.

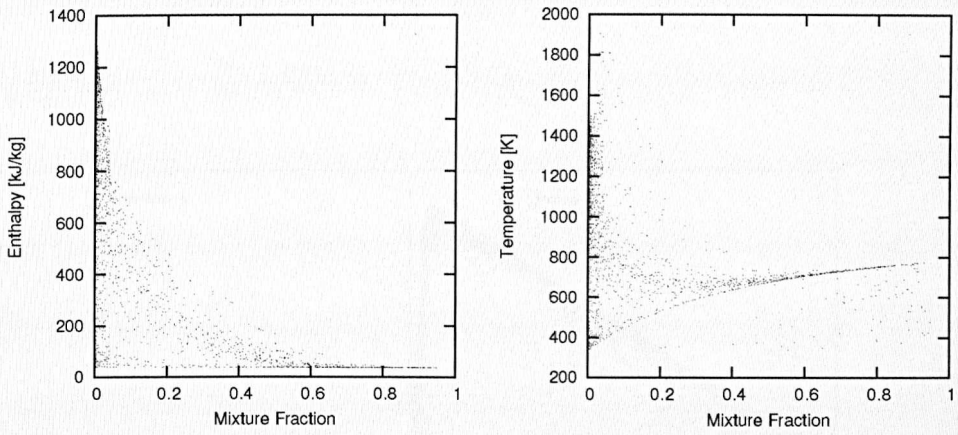

Figure 4.31: Scatter plots of enthalpy and temperature at an early stage for the 1-droplet case.

When the reactions occur, the fuel and oxydiser are consumed and transformed into products. The evolution of the concentration of CO explicitly shows the stages of combustion as presented in Fig. 4.33. In the initial burning stage, no correlation between the CO and mixture fraction is observed. As the reactions evolve, in the initial and especially at the fully burning stage, the correlation is strongly observed. However, in the later stage, when the droplet becomes too small and extinction dominates, CO no longer correlates with mixture fraction.

Figure 4.34 shows the concentrations of CO_2 and H_2O produced, conditioned to mixture fraction. A strong correlation is verified, as expected, with low fluctuations occuring. Figure 4.35 shows the concontrations of O_2 and H_2 which are also well

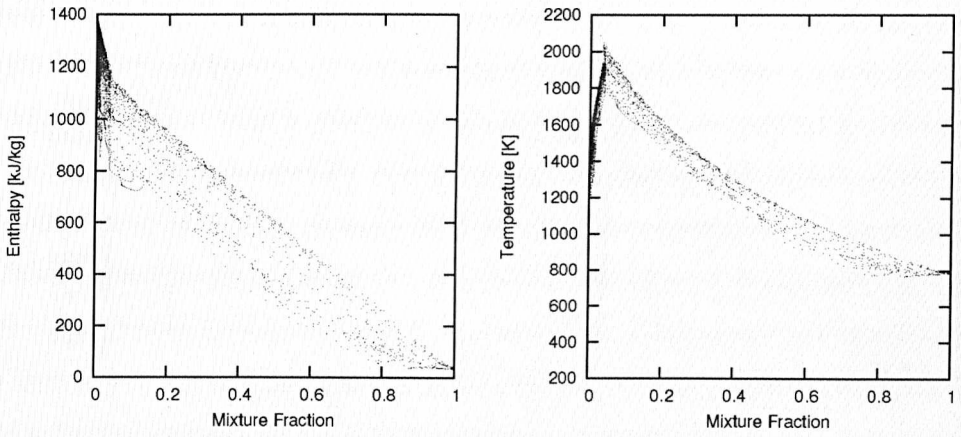

Figure 4.32: Scatter plots of enthalpy and temperature at a fully burning stage for the 1-droplet case.

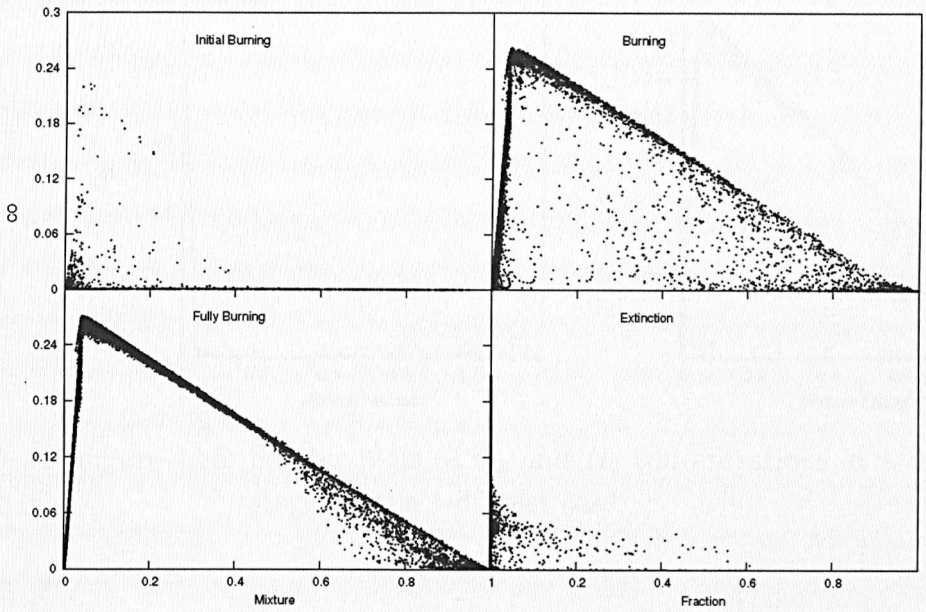

Figure 4.33: Scatter plots of CO concentration at different stages for the 1-droplet case.

correlated to mixture fraction at the fully burning stage.

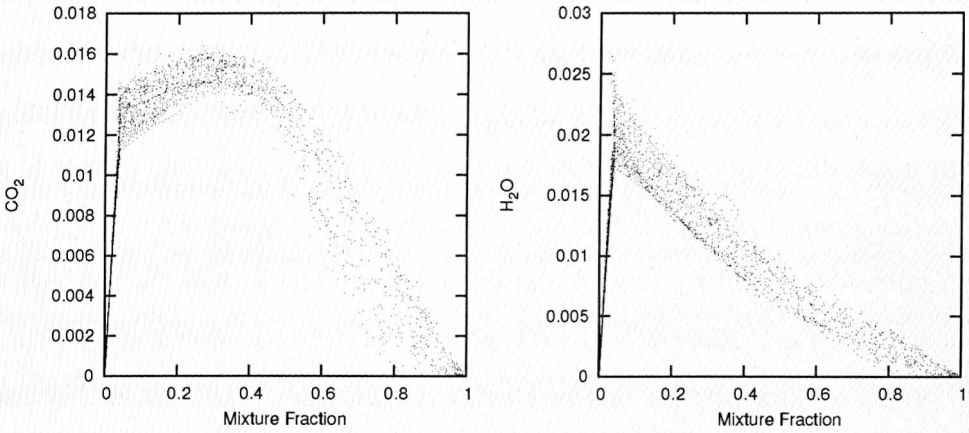

Figure 4.34: Scatter plots of CO_2 and H_2O concentrations at a fully burning stage for the 1-droplet case.

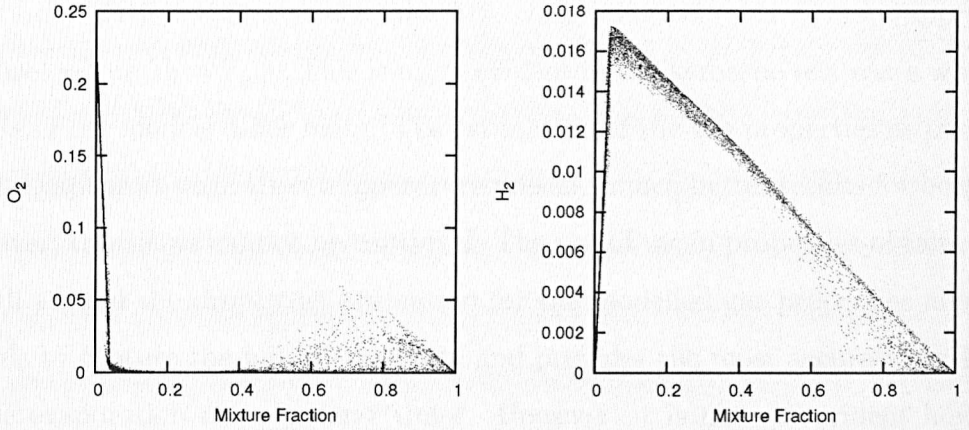

Figure 4.35: Scatter plots of O_2 and H_2 concentrations at a fully burning stage for the 1-droplet case.

4.6 Summary

The present chapter presents a review on the evaporation models derivations. The predictions of evaporation rates using these models are compared to results of DNS performed with the model described in Chapter 3. A brief discussion on the choice of the Nusselt and Sherwood numbers correlations is presented and it is shown that different fuels are better represented by different correlations. The correlations can vary for fuels but also for different Reynolds number ranges. Evaporation rates

are assessed for different droplet densities and flow conditions of n-heptane and kerosene droplet arrays. The results of n-heptane are compared to experimental data and good agreement is obtained.

It is shown that higher droplet densities generate group combustion instead of single droplet combustion. When single droplet combustion occurs, the evaporation rates are independent of the droplet loading. However, when combustion occurs as a group phenomenon, a reduction in the rates is observed. No evident correlation is observed between the evaporation rates and the subgrid kinetic energy and the effects of turbulence are mostly related to vapour dispersion away from the droplet surface.

The evaporation rates of the 1, 8 and 64-droplet cases are compared to two commonly used models for RANS and LES computations. The results show that the model M1 is more accurate than M2, confirming that M1 is more appropriate for cases where $T_d = T_{boil}$. This is more evident in the kerosene test cases where the results of the models differ more. The estimation of the gas properties as properties of pure vapour at saturation temperature presents much better results for both fuels. However, transients cannot be captured. The use of mean properties obtained from a shell around the droplet as estimation for the modelled gas properties allows the models to capture the initial transients and provides the most accurate predictions of the evaporation rates at later times. However, it is not yet evident how these values can be computed between RANS and LES.

Chapter 5

Gas-phase Mixing in Non-reactive Environments

5.1 Introduction

Previous studies of evaporating sprays do not resolve the liquid phase nor the near field and neglect the conditions in the immediate neighbourhood of the individual droplet. However, evaporation and, to some degree combustion, are directly dependent on the local conditions. The local mixture fraction field in inter-droplet regions is fundamentally different from cell averaged values in the RANS and LES context. This difference can have profound effects on the accuracy of mixture fraction based combustion models that rely on accurate closures of the sub-grid distribution of the passive scalar (such as mixture fraction PDF and the conditional scalar dissipation). Schroll et al., 2009, pointed out that satisfactory closures may not be obtained using the source point approximation due to lack of resolution in the near liquid field.

In the present chapter, two- and three-dimensional DNS of methanol droplets are analysed, assessing scalar mixing in terms of mixture fraction PDF and dissipation (Zoby et al., 2009a; Zoby et al., 2009b; Zoby et al., 2010). The mixture fraction PDF is compared to the commonly used β-PDF, defined as

$$P_f = f^{a-1}(1-f)^{b-1}\frac{\bar{\Gamma}(a+b)}{\bar{\Gamma}(a)\bar{\Gamma}(b)} \tag{5.1}$$

with $a = \mu_f \gamma$, $b = (1 - \mu_f)\gamma$ and $\gamma = \frac{\mu_f(1-\mu_f)}{\sigma_f}$. The parameter μ_f is the mean value of f, σ_f is the variance of f and $\bar{\Gamma}$ is the Gamma function.

In the two-dimensional cases, the droplets are represented by infinite cylinders and are presented here for completeness. The physical meaning of these computations must be interpreted with care and the results are surpassed by the three-dimensional computations. Several droplet loadings in static and convective (laminar and turbulent) environments are simulated and the sensitivity of the local gas-phase mixing field to these parameters is quantified. The droplets are organised in infinite, regular, planar layers with thicknesses of one, two, three and four droplets. Droplets and interdroplet spaces, including the near liquid field, are fully resolved using the model described in Chapter 3.

The liquid fuel is assumed to be at 338 K with $\rho_l = 750$ kg/m^3, $\sigma = 1.85\ 10^{-2}$ N/m, $\mu = 3.5\ 10^{-4}$ Pa.s and $h_{fg} = 1.097$ MJ/kg. The droplets are assumed to be at saturation conditions and therefore all heat transferred to the droplets leads to evaporation of the liquid phase. The air surrounding the droplets and at the inflow is at a high temperature of 2530 K. This value of temperature follows the experiments of droplet evaporation rates in combustion products of a flat flame burner performed by Faeth and Lazar, 1971. The local properties are calculated as a function of the local composition (mixture of air and fuel) and temperature using standard kinetic theory as presented in Chapter 3.

The following section describes the two-dimensional test cases followed by the three-dimensional DNS. Finally, a summary of the chapter is presented.

5.2 Direct Numerical Simulations of Droplet Arrays in 2D Cases

In the two-dimensional cases, the domain extends to infinite in x-direction and extends 3 mm in y-direction (see Fig. 5.1). The domain is populated with one, two, three or four infinite rows of equidistant droplets as described in the test list presented in Table 5.1. Inflow/outflow boundary conditions perpendicular to the

droplet layers (y-direction) are used with periodic boundary conditions in the remaining x-direction for the laminar and turbulent cases. In the stagnant cases, the four boundary conditions are outflow. The droplets are initialised with 100 μm diameters and the mesh is Δx=Δy=5 μm. The simulations are carried out until 90% of the droplet mass has evaporated. The ambient pressure is 1 atm for the stagnant and laminar cases and 5 atm for the turbulent cases. Temperature is defined according the the experiments of Faeth and Lazar, 1971.

Table 5.1: 2D Methanol Test Cases

Section	Test	u_∞ [m/s]	T_∞ [K]	Drops	d [μm]	Δx [μm]	p [atm]
4.2.1	1-drop Stagnant	0	2530	1	100	5	1
4.2.1	2-drop Stagnant	0	2530	4	100	5	1
4.2.1	3-drop Stagnant	0	2530	9	100	5	1
4.2.1	4-drop Stagnant	0	2530	16	100	5	1
4.2.2	1-drop Laminar	5	2530	1	100	5	1
4.2.2	2-drop Laminar	5	2530	4	100	5	1
4.2.2	3-drop Laminar	5	2530	9	100	5	1
4.2.2	4-drop Laminar	5	2530	16	100	5	1
4.2.2	1-drop Turbulent	10	2530	1	100	5	5
4.2.2	2-drop Turbulent	10	2530	4	100	5	5
4.2.2	3-drop Turbulent	10	2530	9	100	5	5
4.2.2	4-drop Turbulent	10	2530	16	100	5	5

Different regions need to be defined to allow a zone dependent analysis of the local conditions of the combustible mixture (see Fig. 5.1). Three regions are defined: the global region which comprises all of the computational domain; the inner and outer regions refer to inter-droplet spaces and regions outside the droplet cloud. In addition, in the four-droplet case, different inner regions are identified and analysed. Lines in both directions are also defined as Slice 1 (y-direction) and 2 (x-direction).

5.2.1 Stagnant Environment

The stagnant cases are characterised by the absence of air inflow. However, the gas phase does not remain stagnant as radial velocities relative to the droplets are induced due to the Stefan flow as presented in Fig. 5.2. Experiments have been reported where single droplets are introduced in quiescent hot air environments (Nomura et al., 1996) and also some numerical investigations have been performed (Zhang, 2000; Birouk and Al-Sood, 2010). In these cases, the evaporation rates are

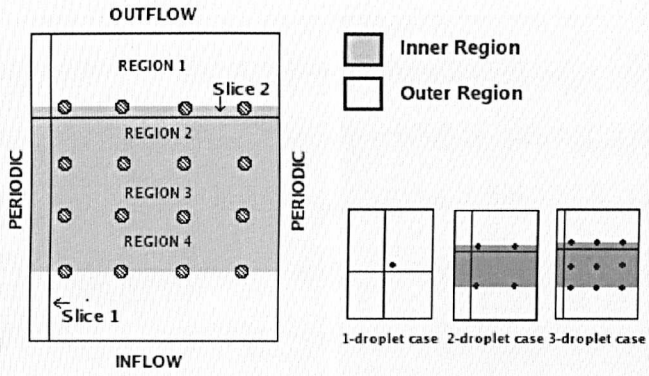

Figure 5.1: Geometry of the 4-droplet layer test case domain and definition of the regions (left figure). The right figure illustrates the droplet configurations for the 1-, 2- and 3-droplet layer test cases.

not affected by the effects of a convective flow.

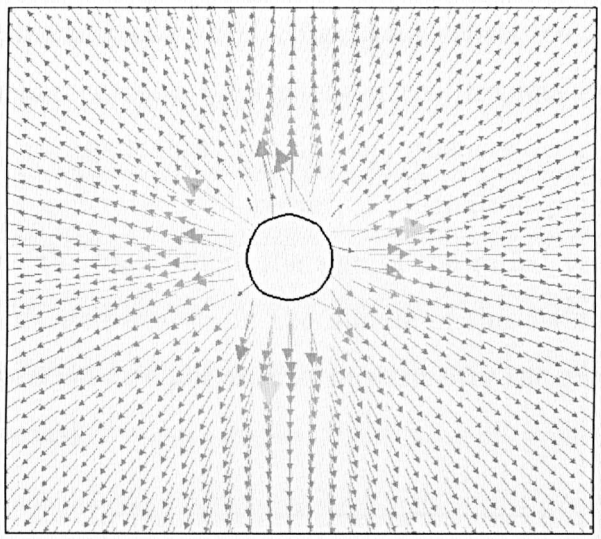

Figure 5.2: Velocities induced by evaporation - Stefan flow - in a stagnant environment.

Instantaneous profiles of the temperature and vapour fraction fields are shown in Fig. 5.3. As can be observed, the temperature is fixed following a radial gradient from the droplet temperature (338 K) at the droplet surface to the maximum temperature (2530 K). The vapour fraction is generated at the droplet surface, then it diffuses and convects radially, mixing with the air. Higher concentrations are found close to the droplet as shown in Fig. 5.3.

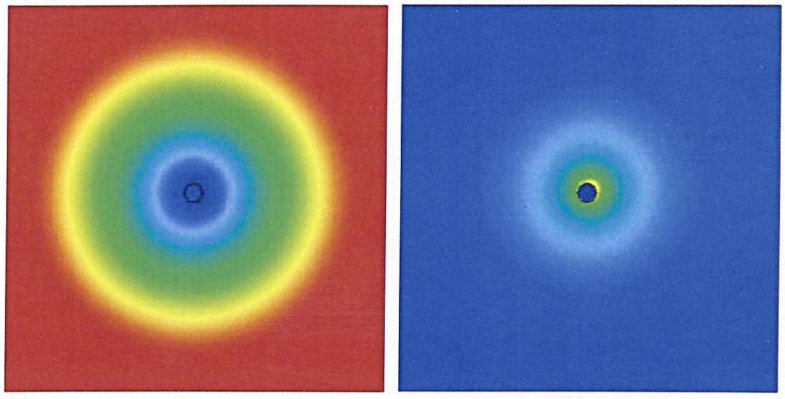

Figure 5.3: Temperature and vapour fraction profiles of the 1-droplet case in a stagnant environment.

The fixed temperature gradient close to the droplet interface induces an interface velocity ($u_i I$) due to evaporation of approximately 1 mm/s, the same as in the experiments of Faeth and Lazar, 1971. Figure 5.4 shows the radial velocity profile along a transversal line crossing the centers of the droplets in the 2-droplet case. It can be observed that the highest velocity disturbances occur close to the droplet where the vapour is generated. Moreover, a stagnation point is found between the droplets defining the limit where the sign of the radial velocity changes. This stagnation point is located exactly in the middle of the distance between the two droplets. The evaporation rate per area is constant over the droplet surface and the round shape is preserved.

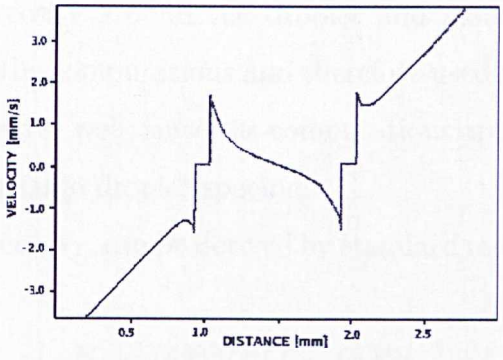

Figure 5.4: Velocity profile along a transversal line passing through the centers of the 2-droplet cases in a stagnant environment.

5.2.1.1 Mixture Fraction

Mixture fraction, f, is equivalent to the vapour fraction in the gas phase in these non-reacting test cases. In the near droplet region for non-inertial droplets (similar to the stagnant case where there is no relative velocity observed between the droplet and the surrounding) the mixture fraction varies with the radial distance, r, as described by Klimenko and Bilger, 1999, as

$$f = f_d - (f_d - f_\infty) \exp\left(\frac{-\dot{m}_d}{4\pi\rho D r}\right) \tag{5.2}$$

where f_d is the value of mixture fraction at the droplet surface, f_∞ is the value of mixture fraction at a large distance from the droplets, $\dot{m}_d$ is the mass evaporation rate of a single droplet, ρ and D are the density and diffusivity in the interdroplet space, respectively. These parameters vary according to the composition and temperature and are not constant in time. The derivation of this equation is presented in Appendix D.

The solution of Eq. 5.2 is compared to the instantaneous data obtained for the one-droplet case. This case is chosen because the space between droplets is large (20 diameters) and the droplet field of one droplet does not affect significantly the others. Figure 5.5 shows the solution calculated for two values of the binary diffusivity, D. The values D=0.00034 m^2/s (at 1 atmosphere and assuming ideal gas behavior for methanol vapour and air) and D=0.00085 m^2/s (average diffusivity calculated from the value for viscosity around the droplet and assuming Sc=0.7) are limit values of diffusivity in the computations and therefore used in the comparisons with Eq. (5.2). The results agree well, since the computations approximate the analytical asymptotic solution for large droplet spacing.

The scalar dissipation, N_f, can be derived by standard means from Equation (5.2) as

$$N_f = (4\pi)^2 D^3 (f - f_\infty)^4 J^{-2} \tag{5.3}$$

where J is the diffusion component of the evaporation rate ($J = \dot{m}_d(f_d - f_\infty)/\rho$).

The results of the one-droplet case for scalar dissipation (see Fig. 5.5) present a

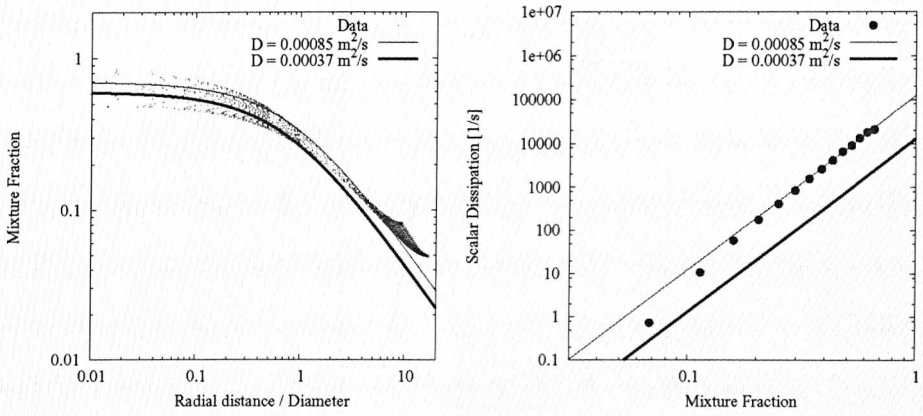

Figure 5.5: Mixture fraction as function of normalised radial distance to the interface and global scalar dissipation for the 1-droplet case in a stagnant environment.

good agreement with Eq. (5.3), also solved for the two values of D. It shows that scalar dissipation is proportional to the fourth power of mixture fraction for the near droplet region in quiescent environments.

The PDF, P_f, of mixture fraction, f, and conditional scalar dissipation, N_f, according to (Klimenko and Bilger, 1999) are correlated by

$$P_f N_f = \frac{\dot{m}_d (f_d - f) c}{\rho} \tag{5.4}$$

where c is the interdroplet spacing.

For the one-droplet case, the global PDF has a single peak and is reasonably well captured by the β-pdf as observed in Fig. 5.6. The large distance between the droplets does not allow one droplet field to affect the other, and the near droplet region modelling can be applied to a large band around each droplet.

In the stagnant cases, scalar dissipation in the interdroplet space depends essentially on the distance between the droplets. As shown in Fig. 5.7, in the interdroplet space along the line that connects the centers of two droplets, mixture fraction agrees very well with the theoretical model given by the following asymptotic solution, derived from Eq. (5.2) for 2 droplets.

$$f = 2f_d - (f_d - f_\infty) \left[\exp\left(\frac{-\dot{m}_d}{4\pi\rho D r}\right) + \exp\left(\frac{-\dot{m}_d}{4\pi\rho D (c - r)}\right) \right] \tag{5.5}$$

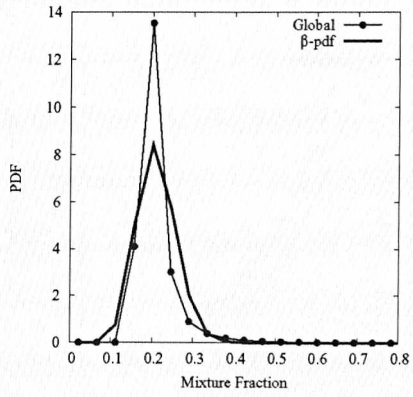

Figure 5.6: Global PDF of the 1-droplet case in a stagnant environment.

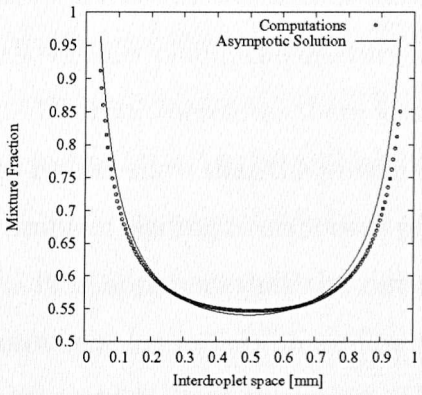

Figure 5.7: Mixture fraction along the line between the droplets centers of the 2-droplet case in a stagnant environment.

5.2.1.2 Scalar Dissipation and Mixture Fraction PDF

In all cases, fuel vapour accumulates in the interdroplet region causing lower mixture fraction gradients and, consequently, lower scalar dissipation. The higher the droplet density, the lower the scalar dissipation, as can be seen in Fig. 5.8. Ignition, an important aspect of sprays first occurs close to the stoichiometric mixture fraction (0.135 for methanol) and scalar dissipation is low. Therefore ignition might occur in interdroplet spaces and not just around droplet clouds in these cases.

Fuel vapour concentrations should be analysed conditioned on different regions of interest. The inner and outer regions are defined in Fig. 5.1. The fuel vapour accumulates in the interdroplet regions leading to a peak in the mixture fraction

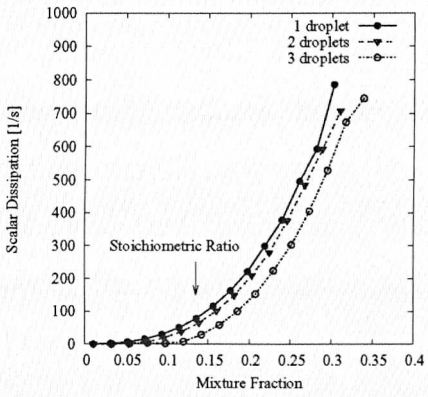

Figure 5.8: Global scalar dissipation for stagnant cases.

PDF at relatively high values of mixture fraction in the two and three-droplet cases (see Fig. 5.9). Outside of the droplet cloud, the mixture fraction PDF peaks at lower values of mixture fraction. Overall, therefore, there is a double peak in the global mixture fraction PDF. The results show that the presumed β-PDF does not capture the bimodal nature of the problem leading to erroneous predictions of the probability of a combustible mixture. It is apparent that the difference of the PDF between the regions needs to be accounted for in two-phase flow modelling where averaging volumes are larger than the droplet cloud thickness. The localised mixing cannot be adequately described by a global PDF and structural information is needed for accurate modelling.

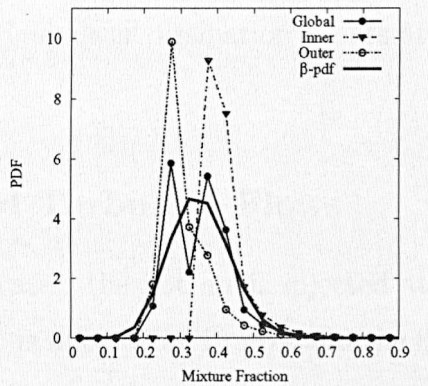

Figure 5.9: PDF of the 3-droplet case in a stagnant environment.

Slices in x and y directions as indicated in Fig. 5.1 aid the evaluaton of direc-

tional behaviour of the PDF and scalar dissipation (see Fig. 5.10) depending on flow velocities and droplet density. As the slices are taken at the same distance from the droplet surface, the results indicate that for the same distance, probability and scalar dissipation differ significantly when they are taken across or along the direction of the flow. It shows that the distance to the droplet cannot be used as unique parameter to specify the mixture fraction field or scalar dissipation and further information is still necessary.

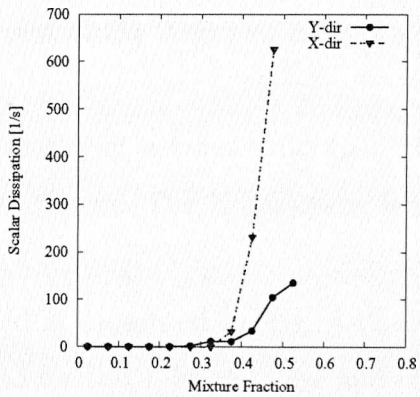

Figure 5.10: Directional scalar dissipation of the 3-droplet case in a stagnant environment.

Figure 5.11 shows that scalar dissipation is not strongly correlated to radial distance. There are two clear branches where lower values of scalar dissipation are found. In the inner region, lower dissipation occurs for smaller radial distances where fuel accumulates while lower dissipation occurs at larger radial distances in the outer region.

5.2.2 Laminar and Turbulent Flows

In the laminar flow test cases, the hot air is injected at 5 m/s. In the turbulent flow test cases, the hot air is injected at 10 m/s and the flow field is initialised with velocities scaled from a 2D isotropic turbulent field. The inflow is given by a 2D isotropic DNS code with maximum fluctuations of 25 m/s. Due to the artificial behaviour of 2D turbulence and in order to sustain the turbulence through out the domain, the Reynolds number is increased from around 100 to 5000. This is achieved

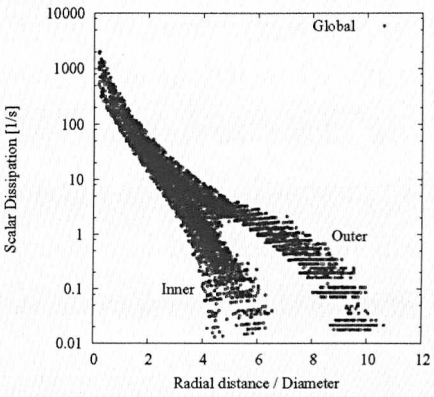

Figure 5.11: Scatter plot of the 2-droplet case in a stagnant environment.

by fixing the gas phase viscosity at a lower value ($\mu = 10^{-6}$ kg/m.s) and increasing the pressure from 1 atm to 5 atm. The Kolmogorov length scale is of the order of the droplet radius.

A typical vorticity field is presented in Fig. 5.12 for the 4-, 2- and 1-droplet cases. The inflow is defined for the 4-droplet case and repeated periodically for the larger domains. It is evident from the figure that the flow is strongly affected by the droplets and develops differently for each of the cases.

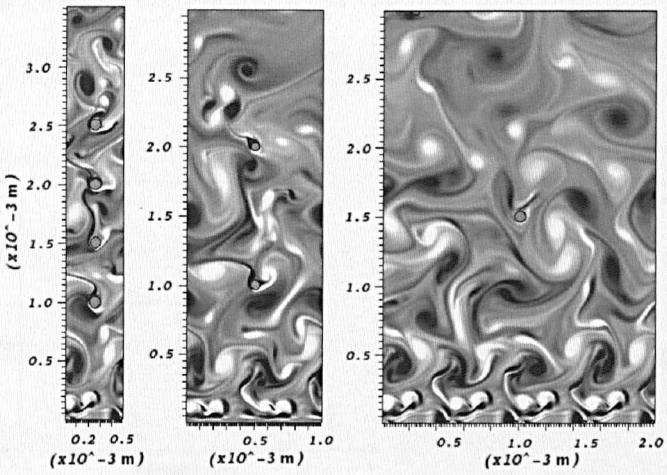

Figure 5.12: Vorticity field after 5 ms for the 4- (left), 2- (centre) and 1-droplet (right) layer turbulent test cases.

5.2.2.1 Mixture Fraction

A first quantitative analysis of the spatial evolution of the mixture fraction field involves a comparison of the computational results with an analytic description of the near droplet field for inertial droplets. Following (Klimenko and Bilger, 1999), mixture fraction along a transversal line (perpendicular to the mean flow field as shown in Fig. 5.13) in the near droplet region is given by the asymptotic solution as follows.

$$f = f_\infty + \frac{\dot{m}_d(f_d - f_\infty)}{4\pi\rho D l} \exp\left(\frac{-r^2}{4Dl/u_\infty}\right) \tag{5.6}$$

The derivation of this equation is presented in Appendix E. f_∞ is the value of mixture fraction far from the droplets, f_d is the value of mixture fraction at the droplet initially centered at (x_d, y_d), r is the transverse distance from the droplet centre, $r = |x - x_d|$, l is the distance from the line to the droplet, $l = y - y_d$, u_∞ is the flow mean velocity, $\dot{m}_d$ is the mass evaporation rate of a single droplet, ρ and D are the density and diffusivity in the interdroplet space, respectively.

Equation (5.6) gives good agreement with the simulations for the laminar case as depicted in Fig. 5.13 where results from the one- and two-droplet layer cases are shown.

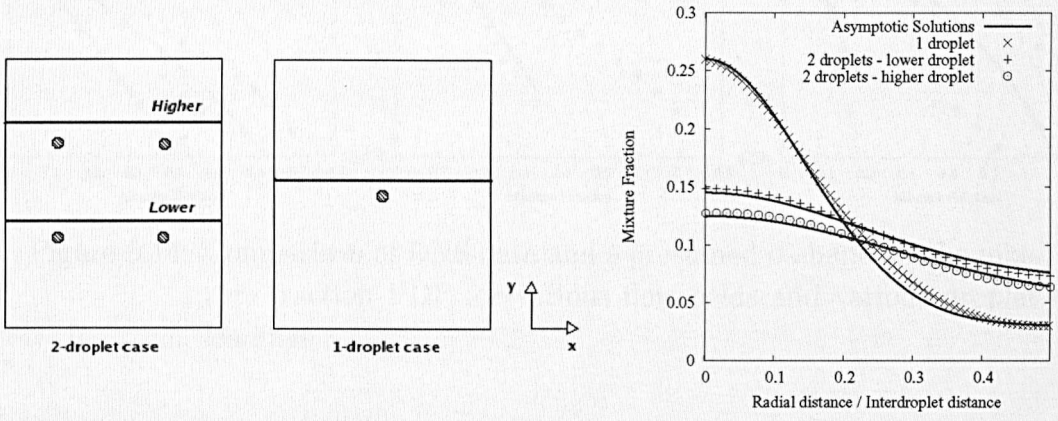

Figure 5.13: Basic scheme of a line perpendicular to the mean flow for the 2- (left) and 1-droplet (middle) cases and mixture fraction along these lines ($l = 500\mu$m) in the laminar test cases.

5.2.3 Gas-phase Mixing

The gas phase mixing is investigated through the mixture fraction PDF and scalar dissipation. With respect to the probability distribution, in stagnant environments where expansion of the gas phase occurs only due to the Stefan flow, the presumed β-PDF does not capture two dominant peaks that develop at two different mixture fraction values in the three-droplet layer case. As shown in Fig. 5.14 the double peak does not occur when the distance between the droplets is large (one-droplet case). However, once the interdroplet distance decreases (two- and three-droplet cases) the bimodal nature of the PDF appears.

For laminar flows, the β-PDF seems to capture better the behaviour. In the turbulent environments, the β-PDF represents reasonably well the probability for the lower droplet density cases but it does not capture the profile for the higher droplet density case (Fig. 5.14). It is clear that structural information must be taken into account when modelling the mixture fraction PDF in two-phase flows, however, defining the appropriate parameters is not evident.

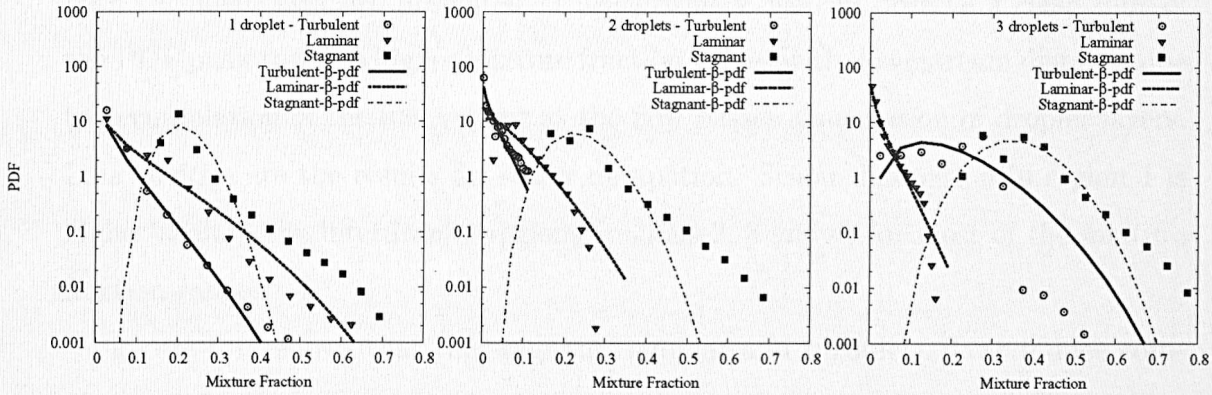

Figure 5.14: Comparison of DNS data and a presumed β-shape for the mixture fraction PDF for various flow fields and various droplet loadings.

Figure 5.15 compares scalar dissipation for the different droplet arrays. It can be seen that the higher the number of droplets (reduced interdroplet space) the lower the scalar dissipation in the laminar cases. However, in turbulent flows, this trend is not repeated, and it cannot be assumed that a higher droplet concentrations

necessarily decrease scalar dissipation over all mixture fraction range.

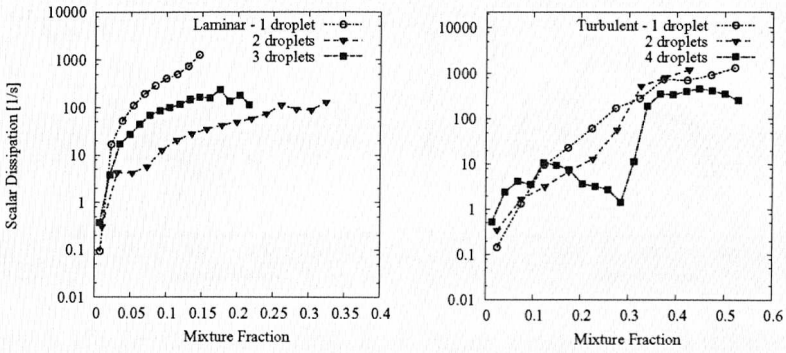

Figure 5.15: Global conditionally averaged scalar dissipation for laminar (left) and turbulent (right) convective environments and various droplet loadings.

Different regimes are identified when the global computational domain is split into different areas depending on their position relative to the droplets (as defined in Fig. 5.1). In Figure 5.16, the PDF and the scalar dissipation of the four-droplet case with turbulent flow are presented. Unsurprisingly, we can observe a clear shift of the PDF peak towards higher mixture fraction values with downstream distance due to accumulation of the fuel vapour as the flow passes a succession of droplet layers. Less obvious are the results for scalar dissipation. Scalar dissipation in region 1 is higher than in the interdroplet regions (regions 2, 3 and 4) for most of the mixture fraction range.

Figure 5.17 shows that the stagnant, laminar and turbulent flows induce completely different magnitude of scalar dissipation in the two-droplet cases. While in the stagnant case the inner and outer region's branches are well defined, in the laminar and especially in the turbulent tests, it is possible to have the same value of scalar dissipation over a wide range of radial locations showing that the scalar dissipation N_f is independent of the radial distance. It is clear that the flow affects significantly the vapour distribution and in terms of scalar dissipation, a clear distinction between inner and outer region is no longer possible once turbulent mixing occurs. Therefore, radial distance does not seem to give sufficient structural

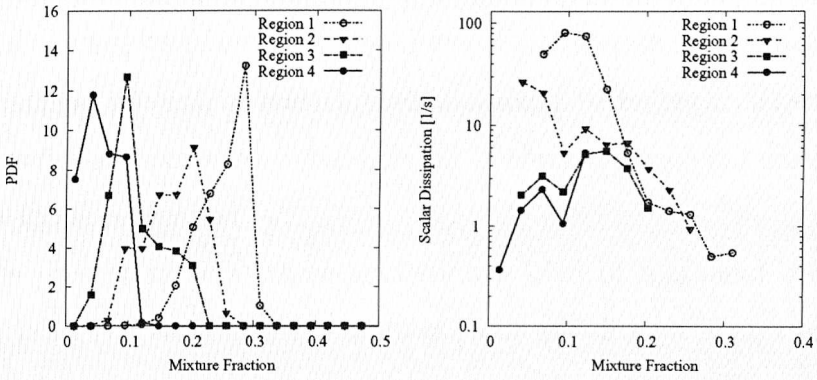

Figure 5.16: Mixture fraction and scalar dissipation in different regions of the 4-droplet turbulent case.

information needed for accurate modelling.

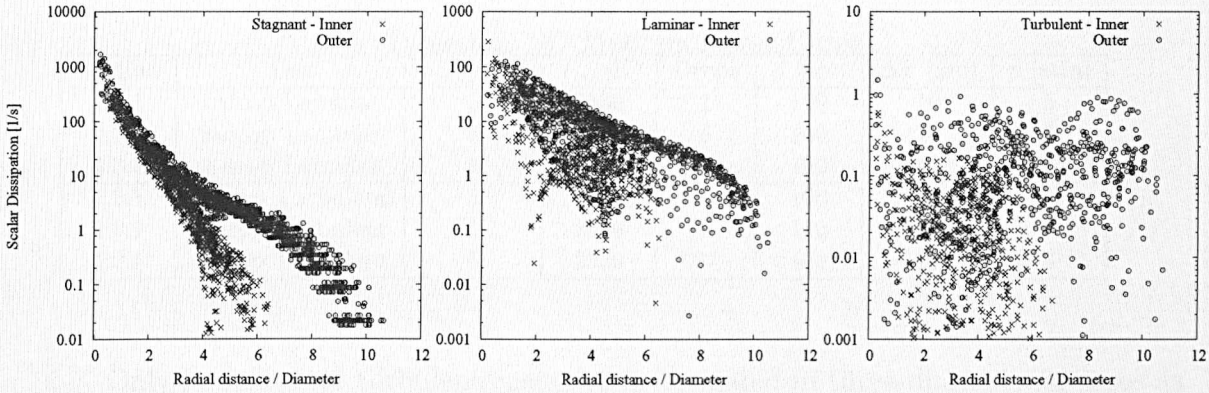

Figure 5.17: Scatter plot of global scalar dissipation in the 2-droplet cases for the stagnant, laminar and turbulent cases.

5.3 Direct Numerical Simulations of Droplet Arrays in 3D Cases

The results presented in the previous section show that the mixture fraction PDF and scalar dissipation vary greatly depending on the position relative to the droplets, droplet loading and flow conditions. In the search for accurate modelling, a zone and radial distance parameterisation is investigated in two-dimensional calculations.

However, two-dimensional droplets, i.e. cylinders, do not represent the three dimensionality of spheres and also two-dimensional turbulence cannot reproduce the energy cascade present in real three-dimensional turbulence. Therefore, the flow characteristics are expected to be different in three-dimensional cases and a further investigation is performed.

In the present section, three-dimensional DNS of methanol droplets are presented. As in the two-dimensional cases, multiple-droplet arrays organised in infinite, regular, planar layers with thicknesses of one, two and four droplets ($d_0 = 100\mu$m) as presented in Table 5.2. Inflow/outflow boundary conditions are used perpendicular to the droplet layers and periodic boundary conditions are used otherwise. The droplets are assumed to be at saturation conditions and the air surrounding the droplets is at a high temperature, 2530K, and ambient pressure is 5 atm.

Table 5.2: 3D Methanol Test Cases

Section	Test	u_∞ [m/s]	T_∞ [K]	Drops	d [μm]	Δx [μm]	p [atm]
4.3.1	1-drop Laminar	5	2530	1	100	10	5
4.3.1	2-drop Laminar	5	2530	8	100	10	5
4.3.1	4-drop Laminar	5	2530	64	100	10	5
4.3.1	1-drop Turbulent	5	2530	1	100	10	5
4.3.1	2-drop Turbulent	5	2530	8	100	10	5
4.3.1	4-drop Turbulent	5	2530	64	100	10	5

Only laminar and turbulent cases are investigated in three-dimensional cases as it better represents real applications of sprays. Regions of the domain and slices used in this work are defined as in Fig. 5.18. Differently from the two-dimensional cases, the slices here are planes perpendicular to the mean flow direction.

5.3.1 Laminar and Turbulent Flows

The laminar and turbulent cases are characterised by mean inflow velocity of 5 m/s. In the turbulent cases, the gas velocity is initialised with a turbulent field from a spectral isotropic DNS code. Turbulence is also imposed on the inflow conditions. Typical turbulence scales as measured in Diesel engines are around 0.8 mm for the integral length scale and 0.25 mm for the Taylor microscale as presented by Subramaniyam et al., 1990. In the simulations, the Taylor microscale is 0.15 mm

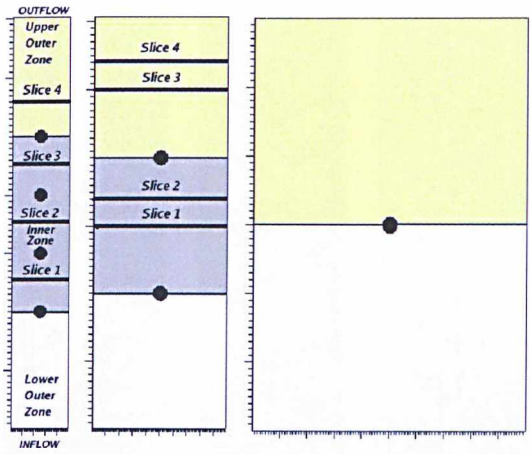

Figure 5.18: Geometry for the 4-, 2- and 1-droplet layer cases with definition of zones and slices (planes).

and the associated Kolmogorov microscale is 30 μm, equivalent to 3Δx. Due to the character of DNS, full scale separation cannot be realised and the computed integral length scale is relatively close to the Taylor length scale. Large scale motion is expected to move all particles equally and fuel concentrations and temperature distribution in inter-droplet space should be relatively invariant to the size of the integral length scale. The ratio between the Kolmogorov scale and the droplet diameter is $\eta/d_0 = 0.33$ and thus similar to the experiments of Birouk et al., 2000. The Reynolds number based on the gas-phase properties and the integral length scale is around 100.

The relative convective mean velocity between droplets and surroundings varies from 0 m/s to approximately 15 m/s with or without superposed vorticity fields. It is noticed from the simulations that the flow is directly affected by the droplets and with the same initial and inflow conditions, the flow field develops differently for different droplet densities. Figure 5.19 shows the mixture fraction fields for the laminar and turbulent 2-droplet cases and the magnitude of vorticity for the 2-droplet turbulent case. It is observed that the instantaneous mixture fraction distribution is completely different in the turbulent and the laminar cases.

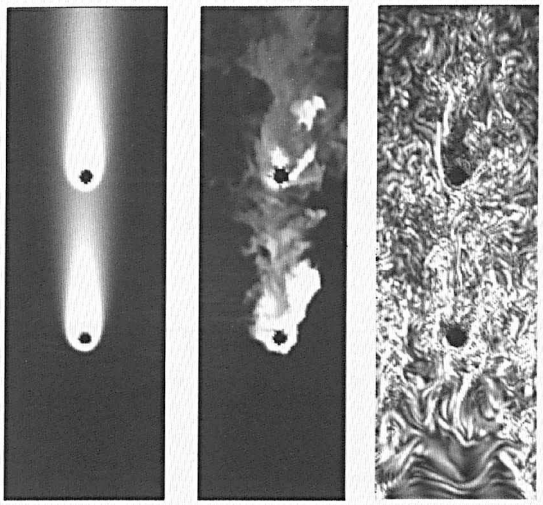

Figure 5.19: Instantaneous mixture fraction field of the 2-droplet laminar (left) and turbulent cases (middle) and magnitude of vorticity (right) of the turbulent case in a plane centrally located across the droplets.

5.3.2 Gas-phase Mixing

A first quantitative analysis of the spatial evolution of the mixture fraction field involves a comparison of the computational results with an analytic description of the near droplet field for inertial droplets. As presented before, mixture fraction along a transversal line perpendicular to the mean flow field in the near droplet region is given by Eq. (5.6) and as follows.

$$f = f_\infty + \frac{\dot{m}_d(f_d - f_\infty)}{4\pi\rho D l} \exp\left(\frac{-r^2}{4Dl/u_\infty}\right)$$

f_∞ is the value of mixture fraction far from the droplets, f_d is the value of mixture fraction inside the droplet initially centered at (x_d, y_d, z_d), r is the transverse distance from the droplet centre, $r = \sqrt[2]{(x - x_d)^2 + (z - z_d)^2}$, l is the distance from the line to the droplet, $l = y - y_d$, $\dot{m}_d$ is the mass evaporation rate of a single droplet, ρ and D are the density and diffusivity in the interdroplet space, respectively. Equation (5.6) gives good agreement with the simulations for the laminar case and for the time averaged mixture fraction distribution in the turbulent cases as depicted in Fig. 5.20.

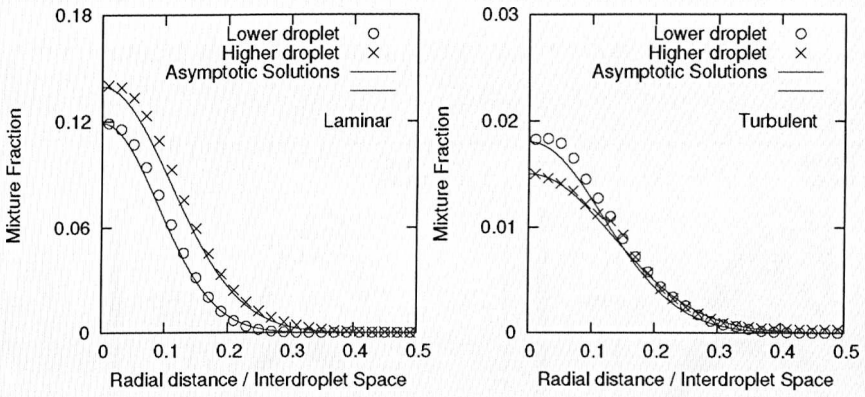

Figure 5.20: Time averaged mixture fraction along a transversal line in the 2-droplet laminar and turbulent cases.

5.3.2.1 Scalar Dissipation

Scalar dissipation is directly dependent on the local mixture fraction gradient. It is noted from the results that the mixture fraction gradients depend on the value of mixture fraction, the zone where the point is located and the axial distance relative to the previous droplet in the direction of the mean flow. Further investigation is then performed for the planes (slices) defined in Fig. 5.18.

Figure 5.21 shows the scatter plots of scalar dissipation conditioned on mixture fraction for the 4 slices defined for the 2-droplet laminar case. On the left hand side plot, the results of the slices located in the inner zone are presented. The plot shows that the data for both slices presents the same shape. However, they have different amplitudes and maximum values of mixture fraction. A similar trend is observed on the plot on the right hand side, for the planes 3 and 4.

The conditionally averaged means of scalar dissipation are shown on the left hand side plot of Fig. 5.22. Even if slices 1 and 3 are located at the same distance, l, to the upstream droplet, they present different maximum mixture fraction values. Furthermore, the value of maximum mixture fraction is directly related to the evaporation rate of the upstream droplets. The same is valid for slices 2 and 4. It is also noted that, within the same zone, the more distant from the upstream droplet, the lower the scalar dissipation. This is due to dissipation of the mixture fraction gradients along the flow. Normalising the value of mixture fraction using

the maximum value for each slice as reference value, the slices located at the same distance l seem to have the same scalar dissipation amplitude.

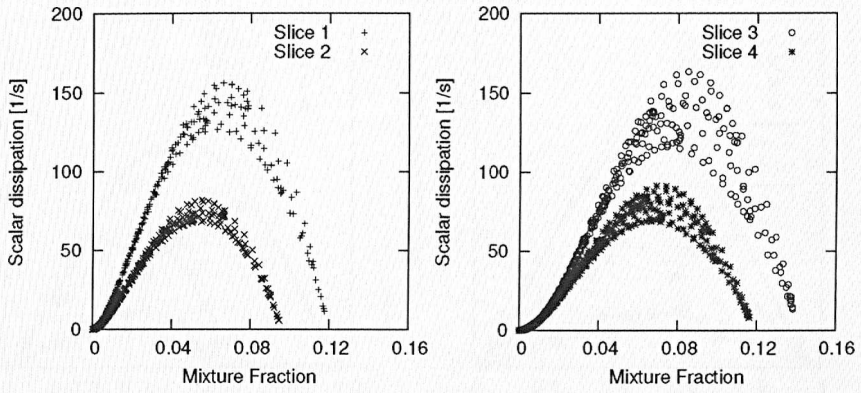

Figure 5.21: Scatter plot of scalar dissipation as function of mixture fraction for the different slices for the 2-droplet laminar case.

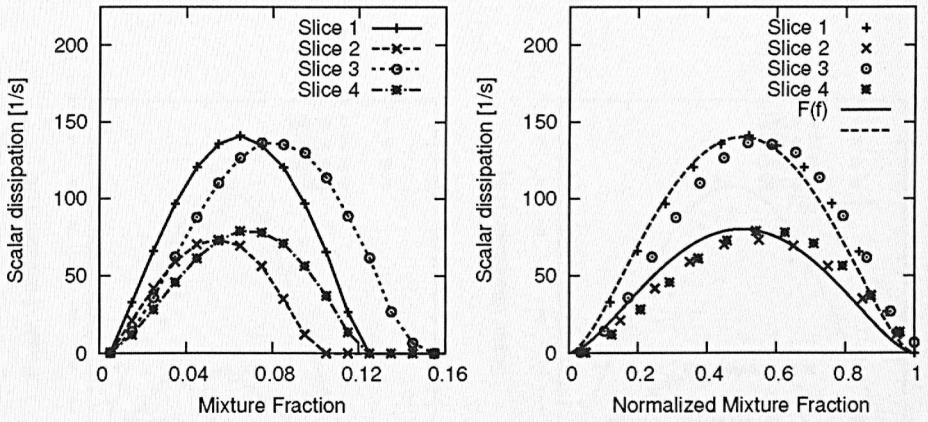

Figure 5.22: Mean scalar dissipation as function of mixture fraction and normalised mixture fraction for the different slices for the 2-droplet laminar case.

Figure 5.23 shows that the mean values of scalar dissipation conditioned on mixture fraction for the turbulent case follow similar profiles as the laminar case. However, in contrast to the laminar test case, the slices located at the same distance, l, do not present the same scalar dissipation amplitude. Furthermore, the further downstream the slice is located, the lower the amplitude. A similar trend is valid for the 4-droplet turbulent case. Figure 5.24 shows that for the case with more

droplet layers, the profile is still the same although amplitude and maximum mixture fraction values vary within the layers for the same distance l.

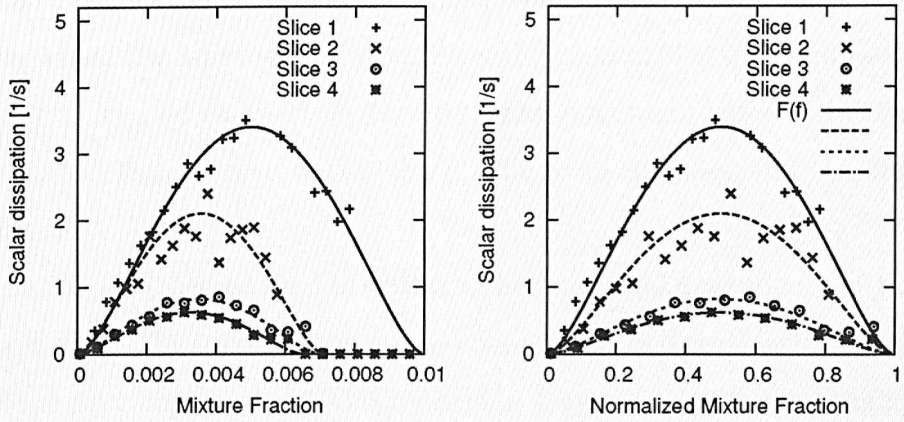

Figure 5.23: Time averaged mean scalar dissipation as function of mixture fraction and normalised mixture fraction for the different slices for the 2-droplet turbulent case.

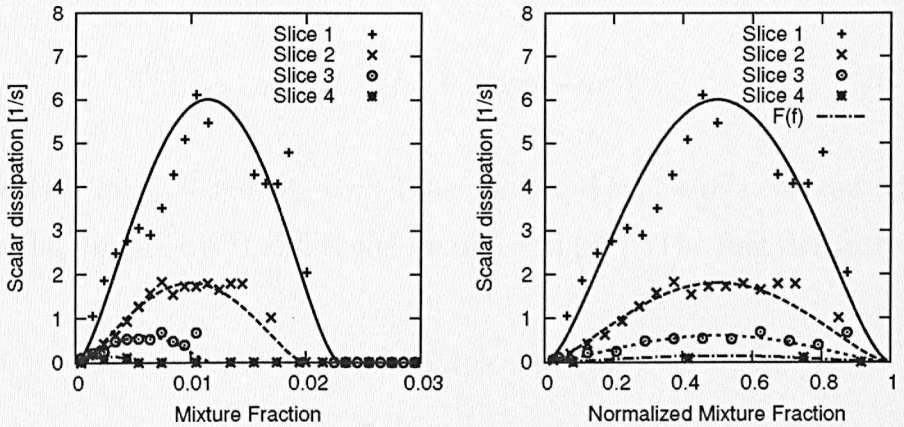

Figure 5.24: Time averaged mean scalar dissipation as function of mixture fraction for the different slices for the 4-droplet turbulent case.

Considering the vapour generation, it is observed that due to the Stefan flow, the gas flow around each droplet is seen as a counterflow. Therefore, an analogy to counterflow diffusion flames modelling can be made. The scalar dissipation follows the profile as proposed for these flames and presented by Peters, 2000. The mean scalar dissipation can be written as a function of the normalised mixture fraction as

$$F(f) = C_1 \exp\left[-2\left(\text{erf}^{-1}\left(1 - 2\frac{f}{f_{max}}\right)\right)^2\right] \tag{5.7}$$

As a result, we define a model for mean scalar dissipation conditioned on mixture fraction where the amplitude, C_1, varies with the axial distance and the zone where the plane is located so $C_1 = F_1(l, zone)$. The maximum value of mixture fraction in the plane, f_{max}, is also dependent on the axial distance and the zone, $f_{max} = F_2(l, zone)$.

Equation (5.6) can be used to estimate the functional dependence of $f_{max} \propto 1/l$ in the lower zone. The conditioning on the zone correlates directly with the evaporation rate of the previous droplets. This modelling suggests a multi-conditioning of scalar dissipation $N_f \equiv < N_f | f, l, zone >$ where the functional dependence on f is given by Equation (5.7).

Another multi-conditioning model for scalar dissipation can be obtained from Eq. (5.6). Assuming that $\frac{\partial f}{\partial r} >> \frac{\partial f}{\partial y}$ where y is the direction of the flow, scalar dissipation becomes $N_f = 2D\left(\frac{\partial f}{\partial r}\right)^2$. Then, rewriting Eq. (5.6) as

$$f = f_\infty + A\exp(-\alpha r^2) \tag{5.8}$$

and $\ln(f) = \ln(f_\infty + A\exp(-\alpha r^2))$. As $f_\infty << A\exp(-\alpha r^2)$, we can approximate $\ln(f) = \ln(A\exp(-\alpha r^2))$ and therefore $\alpha r^2 = \ln\left(\frac{A}{f}\right)$. The first derivative becomes

$$\frac{\partial f}{\partial r} = -2A\alpha r \exp(-\alpha r^2) \tag{5.9}$$

and the square of the first derivative, replacing αr^2 by $\ln\left(\frac{A}{f}\right)$ is

$$\left(\frac{\partial f}{\partial r}\right)^2 = 4A^2\alpha \ln\left(\frac{A}{f}\right) \exp\left(2\ln\left(\frac{A}{f}\right)\right) \tag{5.10}$$

Simplifying Eq. (5.11), the scalar dissipation can be calculated from

$$S(f) = 2D\left(4\alpha f^2 \ln\left(\frac{A}{f}\right)\right) \tag{5.11}$$

Therefore, we can define another model for scalar dissipation conditioned to mixture fraction $S(f) = C_2 ln(A/f)$. The amplitude, C_2, varies with the axial distance and the zone where the plane is located so $C_2 = 8D\alpha f^2$.

Figures 5.25, 5.26 and 5.27 show the comparison between the two models proposed for scalar dissipation, ($F(f)$ and $S(f)$), and the DNS. The first model, $F(f)$, shows a good agreement with the DNS results as mentioned before, however, the asymmetry of the scalar dissipation profile (see Fig. 5.21) is not well represented. The determination of the scalar dissipation amplitude is not closed.

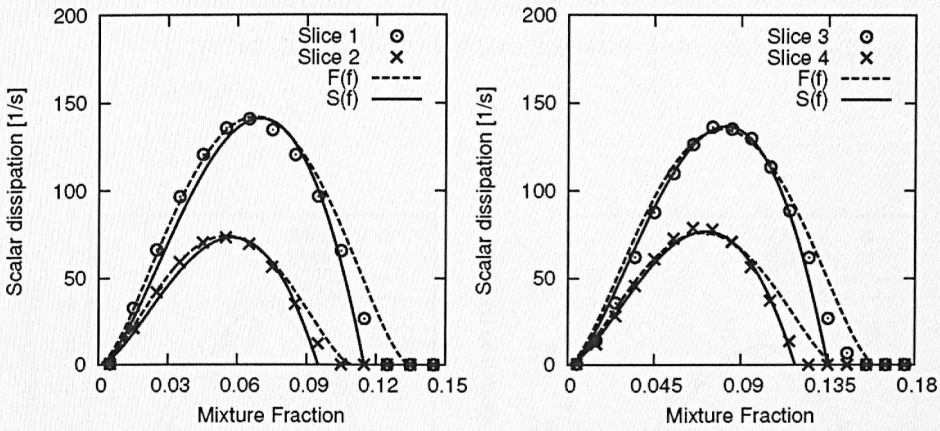

Figure 5.25: Time averaged mean scalar dissipation as function of mixture fraction for the different slices for the 2-droplet laminar case 2 models.

The second model, derived from the mixture fraction equation, presents even better agreement with the DNS results. Despite the relatively good agreement of $F(f)$ with the DNS data, the model is not able to reproduce the asymmetry of the data, which is correctly captured with $S(f)$. This shows that Eq. (5.11) is a better representation of scalar dissipation than Eq. (5.7). In this model, the amplitude of scalar dissipation is closed. The small differences observed between $S(f)$ and the DNS results are due to the assumption of constant density and diffusivity in Eq. (5.6).

Figure 5.28 compares the scalar dissipation for the 4 regions previously defined (see Fig. 5.18) for the 4-droplet laminar test case. The lower the region in the direction of the flow (from 4 to 1), the higher the scalar dissipation conditioned on

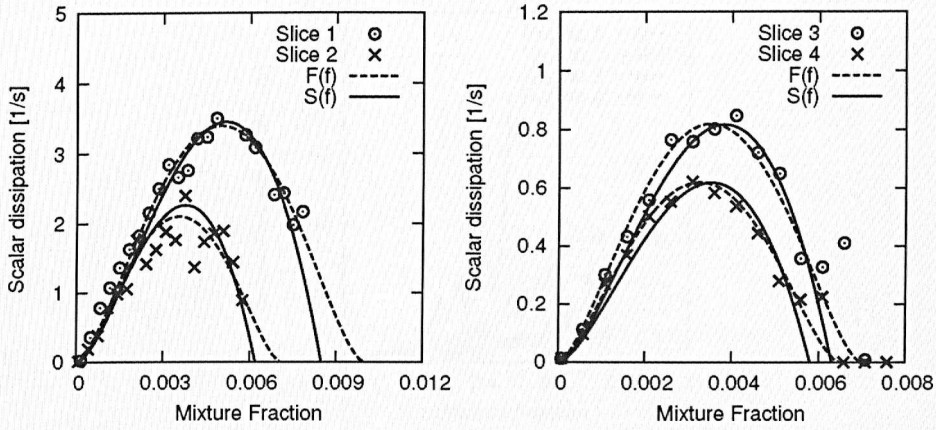

Figure 5.26: Time averaged scalar dissipation as function of mixture fraction for the different slices for the 2-droplet turbulent case 2 models.

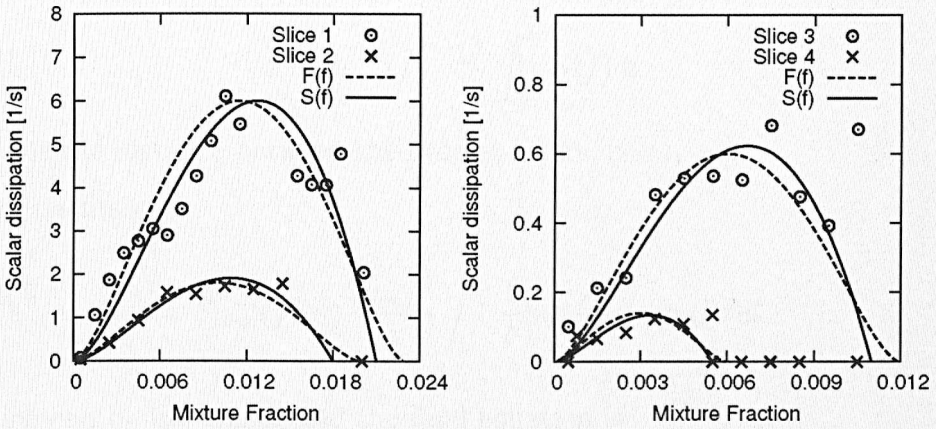

Figure 5.27: Time averaged scalar dissipation as function of mixture fraction for the different slices for the 4-droplet turbulent case 2 models.

mixture fraction. This can be explained by the accumulation of vapour as the flow passes the droplet layers. The mixture fraction gradients decrease, reducing the scalar dissipation as clearly shown in Fig. 5.28.

The two models presented apply for planes across the axial direction. However, the modelling of mean scalar dissipation in a zone is of more interest than the modelling of planes as it can be used in LES or RANS directly. In order to define a model for the mean scalar dissipation in a zone, $S_{zone}(f)$, a volume integral of the

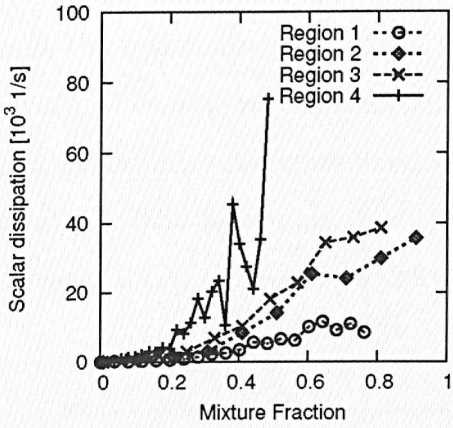

Figure 5.28: Scalar dissipation of different zones for the 4-droplet laminar test case.

second model, $S(f)$, over the zone is calculated.

$$S_{zone}(f) = \frac{1}{c}\int_{l_0}^{l_1} S(f)dl \tag{5.12}$$

where c is the distance between the droplet layers, $c = l_1 - l_0$.

This results in

$$S_{zone}(f) = \frac{2u_\infty f^2}{c}\int_{l_0}^{l_1} \frac{1}{l}\left[\ln(\frac{Al}{f}) - \ln(l)\right] dl \tag{5.13}$$

which can be integrated and the final equation is

$$S_{zone}(f) = \frac{2u_\infty f^2}{c}\left[\ln\left(\frac{A}{f}\right)\ln(c) - \frac{\ln^2(c)}{2}\right] \tag{5.14}$$

Again, the above Eq. (5.14) is fully closed. In Fig. 5.29, the results of its application to the present DNS is shown. The model agrees well with the results of the DNS for two zones (inner and upper outer) in the two-droplet cases. This is also valid for the 4-droplet cases.

From the observations of (Bilger, 2010), a family of scalar dissipation models can be derived depending on the regime and modelling assumptions used. If the droplet is not moving respect to the gas, $u_\infty = 0$ and the Stefan flow is neglected, the functional dependence of the scalar dissipation is $\sim f^4$ and the maximum scalar

dissipation occurs at the droplet surface. In a recent work, Bilger, 2010 include the Stefan flow and shows that the scalar dissipation is $\sim [ln(1-f)]^4 (1-f)^2$. Here, the maximum scalar dissipation occur at very rich mixtures $f \approx 0.86$ but away from the droplet surface. If inertial droplets are considered, the mixing is more intense and the maximum occurs at $f \approx 0.66$ (assuming $A = 1$) and in the limiting case of single phase mixing (not evaporation) the AMC model (OBrien and Jiang, 1991) is maximum at $f = 0.5$.

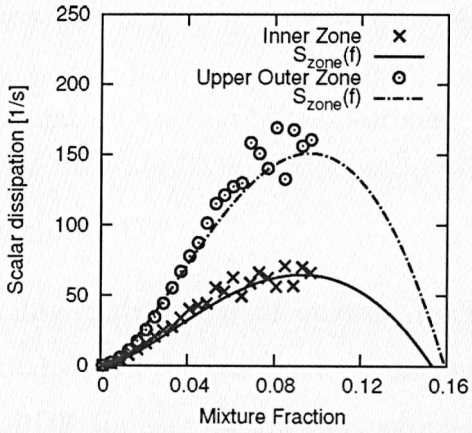

Figure 5.29: Mean scalar dissipation per zone for the 2-droplet laminar case.

The fluctuations of scalar dissipation are also examined through its PDF distribution. On the left hand side plot of Fig. 5.30 the conditional PDF of scalar dissipation is shown for $f = 0.002$. The lower branches correspond to the upper layer and vice-versa. On the right hand side plot different ranges of mixture fraction are considered for Slice 2. The qualitative behaviour is similar in all cases, fluctuations close to zero or smaller than the average have the highest probability.

It is highly probable that the scalar dissipation fluctuations depend on turbulence characteristics, however, no direct correlation could be extracted between the scalar dissipation fluctuations and the turbulent kinetic energy. It seems that the scalar disipation fluctuations will depend more on the size of turbulence, ℓ, than on the velocity fluctuation itself.

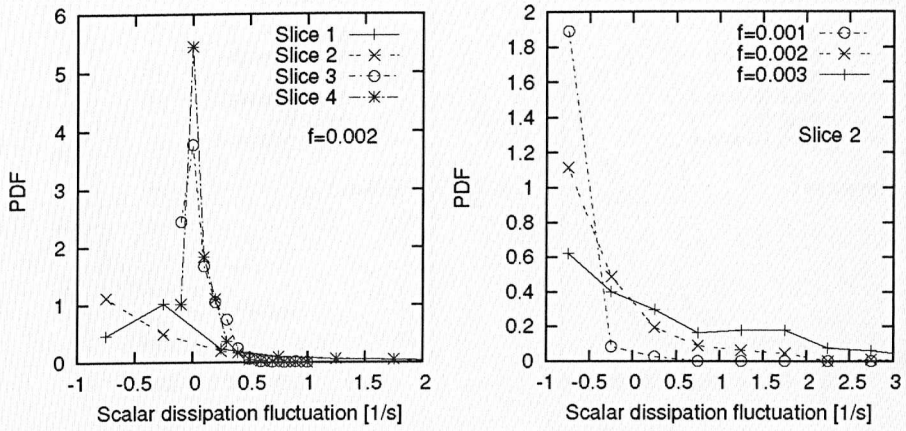

Figure 5.30: PDF of scalar dissipation fluctuation for different slices and various mixture fraction of the 2-droplet turbulent case.

5.3.2.2 Mixture Fraction PDF

With respect to probability distribution of mixture fraction, in two-dimensional stagnant cases, where expansion of the gas phase occurs only due to the Stefan flow, a bimodal profile of the PDF appears for low inter-droplet spaces (as in the 2 and 4-droplet cases) and the presumed β-PDF does not capture this behaviour. It has also been shown that for the two-dimensional laminar flows, the β-PDF seems to capture well the behaviour for the range of inter-droplet space investigated. In the turbulent environments, the β-PDF represents reasonably well the probability of the lower droplet density cases but it does not capture the profile of the higher density (4-droplet) case. In the three-dimensional cases investigated here, the β-PDF, where the mean and variance correspond to averages in homogenous directions, seems to capture correctly the behaviour for all the droplet densities assessed (see Fig. 5.31) and could be used to represent cell averaged PDFs. In the turbulent cases, however, it does not represent well instantaneous values (typical of Large Eddy Simulations) but only time-averaged values, as expected.

Furthermore, the mixture fraction PDF varies depending on the position relative to the droplets. Investigating the PDF for the different zones defined in Figure 5.18, it can be noted the accumulation of fuel vapour as the flow passes the successive droplet zones. Figure 5.32 indicates that in the 2-droplet cases, the Upper Outer

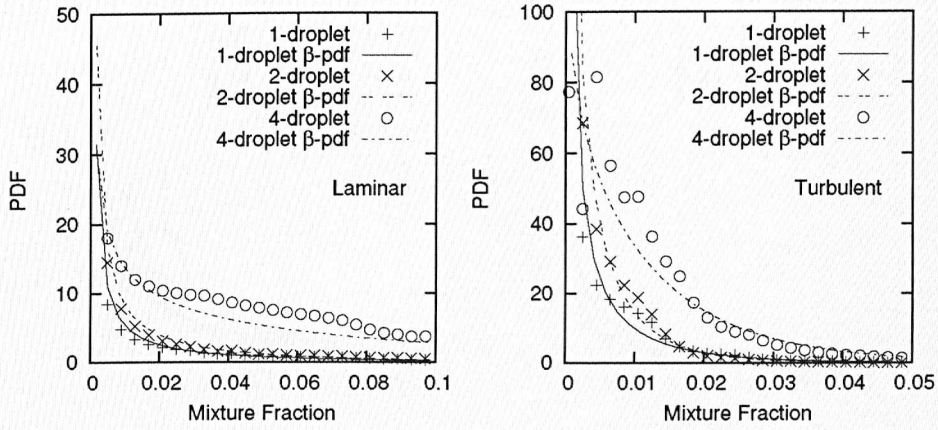

Figure 5.31: Comparison of DNS data and a presumed β-shape for the mixture fraction PDF for various flow fields and various droplet loadings.

zone has higher probability of higher mixture fraction than the previous zone, the Inner Zone, for both laminar and turbulent environments. This behaviour is also observed in the 4-droplet cases (see Fig. 5.33) showing that the further downstream the zone is located, the higher the probability of higher mixture fraction values.

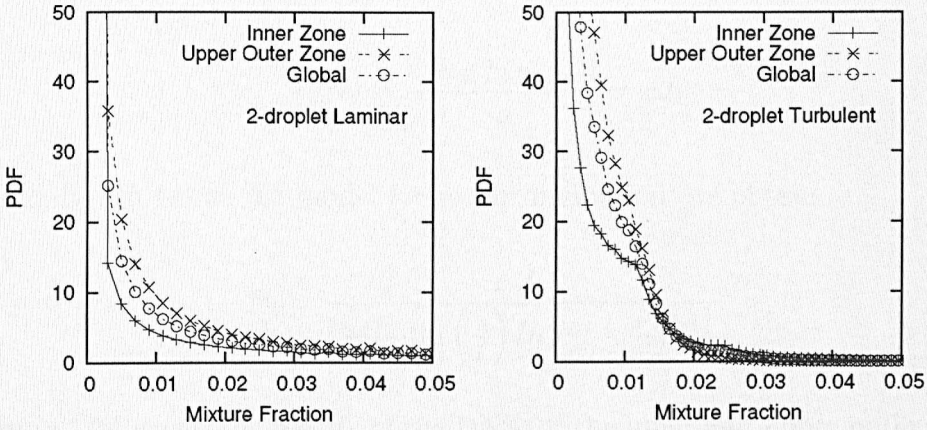

Figure 5.32: Comparison of mixture fraction PDF of different zones for the 2-droplet laminar and turbulent cases.

Comparing the PDFs from the DNS and the β-PDF, good agreement is also verified for the PDF of each region. Figure 5.33 shows the comparison of the PDFs for the 4-droplet laminar case. The β-PDF seems to very accurately represent the

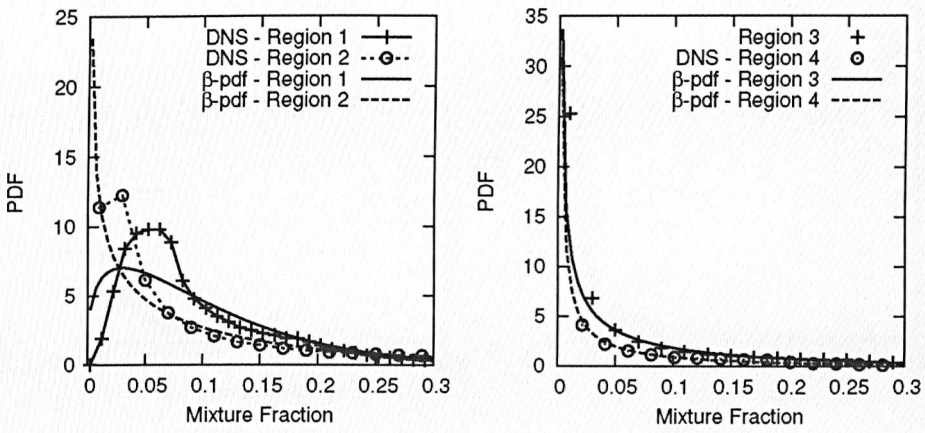

Figure 5.33: Comparison of mixture fraction PDF of different regions for the 4-droplet laminar case.

PDFs of the downstream regions (3 and 4) with errors lower than 2%. The PDFs of the upstream regions (1 and 2) are relatively well captured by the β-PDF. However, the peak of the PDF of Region 1 is significantly different from the presumed by the β-PDF with errors of approximately 25%.

Klimenko and Bilger, 1999 also proposed that the PDF, P_f, and the scalar dissipation, N_f, in the near droplet field are related through Eq. 5.4.

$$P_f N_f = \frac{c\,\dot{m}_d(f_d - f_\infty)}{\rho} = cJ_1 \tag{5.15}$$

Using Eq. (5.14) as the model for scalar dissipation, we obtain

$$P_f = \frac{c\,J_1}{\frac{2u_\infty f^2}{c}\left[\ln\left(\frac{A}{f}\right) ln(c) - \frac{\ln^2(R_c)}{2}\right]}. \tag{5.16}$$

Figure 5.34 shows the results of the DNS for the inner and upper outer zones for the 2-droplet laminar case. The mixture fraction PDF of the DNS is compared to the commonly used β-PDF and the PDF model of Eq. (5.16), defined as $K_{pdf,zone}$. The figure shows that the β-PDF and the model have very similar profiles in the mixture fraction range of interest. Furthermore, they both represent well the predictions of the DNS for mixture fraction PDF per zone, proving that both representations provide accurate results.

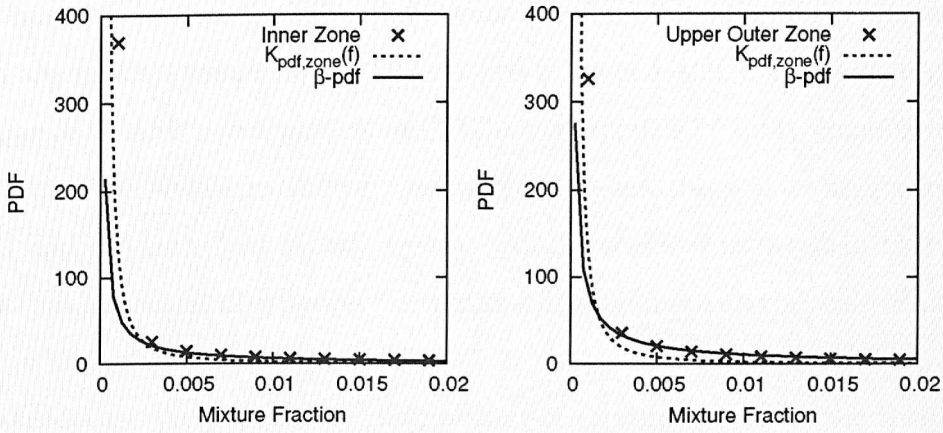

Figure 5.34: Comparison of PDF for the inner and upper outer regions of the 2-droplet laminar case.

5.4 Summary

Two- and three-dimensional evaporating droplet arrays in stagnant, laminar and turbulent environments are assessed in order to investigate local mixing inhomogeneities, mixture fraction PDFs and scalar dissipation. Different dependencies of PDF and scalar dissipation can be identified and large inhomogeneities exist for all test cases within the computational domain. In the two-dimensional cases, the β-PDF seems to capture the global behaviour for laminar environment test cases well, but not for higher droplet densities under stagnant and turbulent conditions. Radial distance to the droplets and droplet density do not provide sufficient structural information for accurate modelling.

In the three-dimensional calculations, it is found that scalar dissipation conditioned to mixture fraction follows a similar profile to that in a counterflow diffusion flame model. The conditioned scalar dissipation may be represented by an exponential of the inverse of the error function with the amplitude and reference value depending on structural parameters. Closure for the scalar dissipation amplitude is needed though. Another modelling is proposed deriving an analytical solution for mixture fraction as function of radial distance. Accurate representation of scalar dissipation is achieved and no closure model is needed. This second model is extended and a fully closed model for scalar dissipation per zone is derived. Further derivation of the second model is performed and a new model for scalar dissipation per zone

is proposed. These new multi-conditioning models offer accurate representation of scalar dissipation where no further closure is needed and may offer an attractive alternative to AMC-type models in CMC-based models of spray combustion.

No direct correlation could be extracted between the scalar dissipation fluctuations and the turbulent kinetic energy. At the scales considered in this study, it seems that the scalar dissipation fluctuations depend more on the scale of turbulence than on the velocity fluctuations.

Considering the probability distribution of mixture fraction, the relative good agreement of the AMC model translates into an expected good behaviour of the β-PDF for both laminar and turbulent cases. Arising from the new model for conditional scalar dissipation a mixture fraction PDF expression per zone is presented. The model shows similar agreement to the β-PDF for the range of mixture fraction studied. Therefore, accurate modelling is also achieved for the PDF of mixture fraction in the near droplet field.

Chapter 6

Conclusions and Future Work

6.1 Conclusions

The present thesis addresses important issues on the modelling of liquid sprays, namely droplet evaporation in laminar and turbulent and the associated vapour mixing. In order to help the understanding of these issues, a novel model, coupling a mass conservative Level Set approach with the Ghost Fluid method, is implemented and validated. The liquid phase and the immediate neighbourhood of the droplets are fully resolved.

Using this new implementation, DNS of *n*-heptane and kerosene droplets are performed to investigate evaporation rates of regular droplet arrays in stagnant, laminar and turbulent flows. The results in inert environments are compared to available experimental data for validation. Further investigations are performed and the effects of different inflow velocities and reactive environments on evaporation rates are assessed. The computed evaporation rates are then compared to two models commonly used in LES and RANS calculations. This is done in order to evaluate the errors associated with these models and with the method of calculation used for evaluation of the gas-phase properties.

The models denoted M1 and M2 use Nusselt and Sherwood number correlations, respectively, that vary with fuel and Reynolds number range. The comparison of the results with the models shows that M1 is more accurate than M2 in all the

droplet density range studied. The estimation of the gas properties in the models is of fundamental importance. The use of the properties of pure vapour at saturation temperature presents better results than the combination of vapour and air properties via a mixing rule for both fuels. However, transients cannot be captured. For the entire droplet density range, the use of mean properties obtained from a shell around each droplet as an estimation for the modelled gas properties allows the models to capture the initial transients and provides the most accurate predictions of the evaporation rates at later times with errors of around 2%. However, it is not yet evident how these values can be computed from RANS and LES.

In reactive environments, it is noted that for the test cases considered a droplet spacing lower than ten diameters generates group combustion instead of single droplet combustion. When single droplet combustion occurs, the evaporation rates are independent of the droplet loading. However, when combustion occurs as a group phenomenon, a reduction in the droplet evaporation rate is observed and this varies with droplet spacing.

In the results obtained, no evident correlation is observed between the evaporation rates and the subgrid kinetic energy either in inert or reacting flows. The effects of turbulence seem to mostly affect the vapour dispersion away from the droplet surface and the flame profile.

Gas-phase mixing is studied through the simulation of two- and three-dimensional evaporating droplet arrays in stagnant, laminar and turbulent environments. Local mixing inhomogeneities, mixture fraction PDFs and scalar dissipation are assessed. In the two-dimensional cases, the β-PDF captures well the global behaviour for laminar environment test cases, but not for the higher droplet densities under stagnant and turbulent conditions. In these cases, the radial distance to the droplets and the droplet density are investigated as a structural parameter for accurate modelling. However, no correlation is observed in laminar and turbulent cases and these parameters do not provide sufficient information.

In the three-dimensional calculations, it is found that scalar dissipation conditioned on mixture fraction follows a similar profile to that in a counterflow diffusion flame model, however, it is noted that some further closure is needed. A modified

modelling approach is proposed deriving an analytical solution for mixture fraction as a function of radial distance. This new approach provides a complete model and no further closure is needed. The two approaches presented offer a multi-conditioning modelling for scalar dissipation, using as the conditioning variables mixture fraction, distance to previous droplet and zone of location; the accurate representation of mean scalar dissipation is then achieved.

In all the studies reported, no direct correlation could be extracted between the scalar dissipation fluctuations and the turbulent kinetic energy. The β-PDF seems to capture well the global behaviour of mixture fraction in the laminar environment test cases and for the time averaged behaviour in the turbulent cases.

6.2 Main Contributions

The present thesis addresses some important issues on liquid sprays modelling. The main new contributions of this thesis are the development of a simple and computationally inexpensive mass conserving approach to overcome the mass loss associated with the Level Set method and the new treatment of interface flux using the Ghost Fluid method. These two new approaches allow better representation of two-phase flows.

A new model for the calculation of gas-phase properties and the mean scalar dissipation in reacting flows are proposed. In the evaporation rates studies, a "shell" model for the calculation of gas phase properties is proposed and accurate predictions for the rates are obtained. In the gas-phase mixing analysis, two new different models are proposed for the mean scalar dissipation, offering an attractive alternative to AMC-type models in CMC-based models of spray combustion. One of these models needs closure of the amplitude term, the other is fully closed. A mixture fraction PDF model is derived from the closed model and its results are similar results to those from the β-PDF.

6.3 Future Work

In the evaporation rate studies, it is observed that the commonly used models are strongly dependent on the Nusselt and Sherwood correlations and also in the definition of the gas phase properties. A shell model has been proposed in order to define the gas properties, however, its extension to LES and RANS calculations is not obvious. Therefore, improvements in the evaluation of these properties and possibly further work to define how to apply the shell model to LES and RANS methods should be investigated. Moreover, further assessment of the Nusselt and Sherwood number correlations for different fuels and wider ranges of temperature and Reynolds number should be performed. These correlations can be obtained through experiments but as the DNS have proved to well represent the available experiments, a series of simulations could be performed in order to generate a database for LES and RANS simulations.

The present investigation matches well the framework developed by Klimenko and Bilger, 1999 on droplet combustion, defining different asymptotic regimes depending on the interdroplet spacing and turbulent scales. A natural extension of this work would be to study the regimes not covered herein and provide closures for the probability density function and scalar dissipation fluctuations. In order to validate the models, non-uniform droplet distributions should be analysed to better reflect the liquid droplet and gas interactions found in practical two-phase flows.

Appendix A

n-Heptane and Kerosene Chemical Mechanisms

In the present work, the combustion of kerosene and *n*-heptane droplets is investigated. Complete mechanisms can be composed of hundreds of chemical reactions and the costs of using them would make the computational simulations unfeasable. Therefore, reduced chemical mechanisms are used in order to represent the main reactions involved. The mechanisms used in the simulations are as follows.

A.1 *n*-Heptane mechanism

The reduced mechanism used for *n*-heptane was proposed by (Liu et al., 2004) and uses 21 species (OH, HO_2, H, CO, CO_2, H_2, H_2O_2, H_2O, CH_2O, O_2, *n*-C_7H_{16}, C_3H_6, C_2H_4, C_6H_{12}, CH_3, C_4H_8, C_3H_4, C_2H_2, CH_4, $C_7H_{15}O_2$ and OC_7H_{13}) in 18 steps. The reactions are

$$n - C_7H_{16} \rightharpoonup C_3H_6 + 2C_2H_4 + H_2$$

$$n - C_7H_{16} + O_2 + OH \rightharpoonup RO_2 + H_2O$$

$$RO_2 + O_2 \rightharpoonup OR"O_2H + OH$$

$$OR"O_2H \rightharpoonup 2C_2H_4 + CH_2O + CH_3 + CO + OH$$

$$1 - C_6H_{12} + H_2O \rightharpoonup C_3H_6 + C_3H_4 + H_2O$$

$$1 - C_4H_8 + OH \rightharpoonup C_2H_4 + CH_3 + CH_2O$$

$$C_3H_6 + H_2O \rightharpoonup C_2H_4 + CH_2O + H_2$$

$$C_3H_4 + H_2O \rightharpoonup C_2H_4 + CO + H_2$$

$$C_2H_4 \rightharpoonup C_2H_2 + H_2$$

$$C_2H_2 + O_2 \rightharpoonup 2CO + H_2$$

$$CH_4 + H \rightharpoonup CH_3 + H_2$$

$$CH_3 + OH \rightharpoonup CH_2O + H_2$$

$$CH_2O \rightharpoonup CO + H_2$$

$$2HO_2 \rightleftharpoons H_2O_2 + O_2$$

$$H_2O_2 \rightleftharpoons 2OH$$

$$CO + H_2O \rightleftharpoons CO_2 + H_2$$

$$O_2 + H_2 \rightleftharpoons 2OH$$

$$2H \rightleftharpoons H_2$$

The reaction rates of the skeletal mechanism is presented in Liu et al., 2004.

A.2 Kerosene mechanism

The chemistry of kerosene is approximated by a 4 steps and 7 species (CO, CO_2, H_2, N_2, H_2O, O_2 and $C_{12}H_{23}$) mechanism for hydrocarbon combustion (Jones and

Lindstedt, 1988). The reaction mechanism is

$$C_{12}H_{23} + 6O_2 \rightharpoonup 12CO + 11.5H_2 \qquad (i)$$

$$C_{12}H_{23} + 6H_2O \rightharpoonup 12CO + 23.5H_2 \qquad (ii)$$

$$H_2 + 0.5O_2 \rightleftharpoons H_2O \qquad (iii)$$

$$CO + H_2O \rightleftharpoons CO_2 + H_2 \qquad (iv)$$

with rate constants*:

$$r_{f,i} = 3.00 \times 10^8 \exp\left(\frac{-30000}{RT}\right) \rho\, n_{C_{12}H_{23}}\, n_{H_2O}$$

$$r_{f,ii} = 4.4 \times 10^{11} \exp\left(\frac{-30000}{RT}\right) \rho^{0.75} \sqrt{n}_{C_{12}H_{23}}\, {n_{O_2}}^{1.25}$$

$$r_{f,iii} = \frac{2.50 \times 10^{16}}{T} \exp\left(\frac{-40000}{RT}\right) \rho^{0.75} \sqrt{n}_{H_2}\, {n_{O_2}}^{2.25} / n_{H_2O}$$

$$r_{f,iv} = 2.75 \times 10^9 \exp\left(\frac{-20000}{RT}\right) \rho\, n_{CO}\, n_{H_2O}$$

A.3 Ignition delays of *n*-heptane and kerosene

The ignition delay of *n*-heptane is similar to kerosene. Figure A.1 shows the ignition delays for kerosene at 8.7 atm and for *n*-heptane at different pressures. Comparing the ignition times at approximately 9 atm for temperature equal to 1000 K, for example, it is can be seen that the ignition delay of both fuels is around 1 ms.

*The units of the reaction rates are: $\frac{kmol}{kg\ s}$.

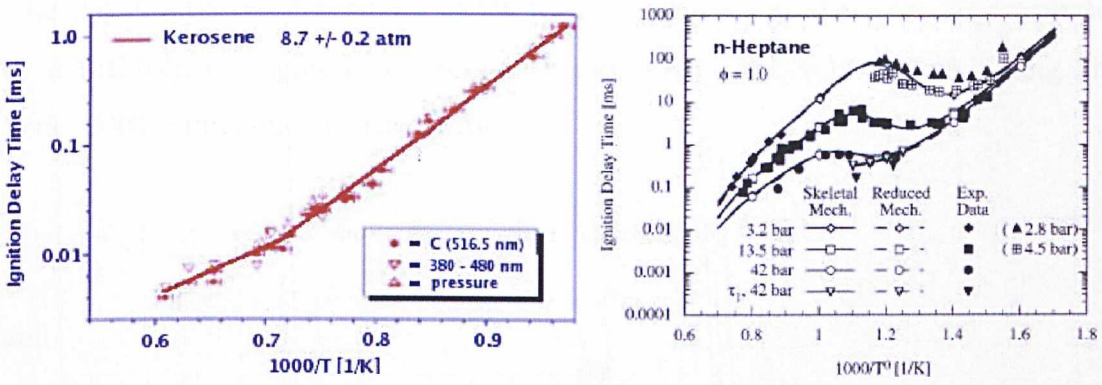

Figure A.1: Ignition delays of kerosene (Dean et al., 2005) and *n*-heptane (Liu et al., 2004).

Appendix B

WENO Scheme

The absolute partial derivatives of the level set function gradient are approximated by a fifth-order weighted essentially nonoscillatory (WENO) scheme (Jiang and Peng, 2000). Introducing the notation:

$$\Delta^+\phi_k = \phi_{k+1} - \phi_k, \quad \Delta^-\phi_k = \phi_k - \phi_{k-1},$$

and

$$\phi_x = \frac{\partial\phi}{\partial x},$$

the WENO approximations in 1D, for simplicity, are

$$\phi_x^{\pm} = \frac{1}{12}(-\frac{\Delta_x^+\phi_{i-2}}{\Delta x} + 7\frac{\Delta_x^+\phi_{i-1}}{\Delta x} + 7\frac{\Delta_x^+\phi_i}{\Delta x} - \frac{\Delta_x^+\phi_{i+1}}{\Delta x}) \pm \Phi^{WENO}(a,b,c,d) \quad \text{(B.1)}$$

where

$$a = \frac{\Delta_x^-\Delta_x^+\phi_{i\pm2}}{\Delta x},\ b = \frac{\Delta_x^-\Delta_x^+\phi_{i\pm1}}{\Delta x},\ c = \frac{\Delta_x^-\Delta_x^+\phi_i}{\Delta x},\ d = \frac{\Delta_x^-\Delta_x^+\phi_{i\mp1}}{\Delta x}.$$

and

$$\Phi^{WENO}(a,b,c,d) = \frac{1}{3}\omega_0(a-2b+c) + \frac{1}{6}(\omega_2 - \frac{1}{2})(b-2c+d). \quad \text{(B.2)}$$

The nonlinear weights are given by

$$\omega_0 = \frac{\alpha_0}{\alpha_0 + \alpha_1 + \alpha_2}, \ \omega_2 = \frac{\alpha_2}{\alpha_0 + \alpha_1 + \alpha_2}$$

$$\alpha_0 = \frac{1}{(\epsilon + IS_0)^2}, \ \alpha_1 = \frac{6}{(\epsilon + IS_1)^2}, \ \alpha_2 = \frac{3}{(\epsilon + IS_2)^2}$$

The smoothing indicators are

$$IS_0 = 13(a-b)^2 + 3(a-3b)^2,$$

$$IS_1 = 13(b-c)^2 + 3(b+c)^2$$

and

$$IS_2 = 13(c-d)^2 + 3(3c-d)^2.$$

The smoothing indicators proposed by (Jiang and Peng, 2007) are also tested but no significant improvement in the stability or the accuracy of the reinitialisation procedure is observed.

In order to guarantee monoticity of the reinitialisation equation the partial derivatives are defined by

$$if\ \phi \geq 0 \begin{cases} \phi_x^+ = -\min(\phi_x^+, 0) \\ \phi_x^- = \max(\phi_x^-, 0) \\ \phi_x = \max(\phi_x^+, \phi_x^-) \end{cases}$$

$$if\ \phi < 0 \begin{cases} \phi_x^+ = \max(\phi_x^+, 0) \\ \phi_x^- = -\min(\phi_x^-, 0) \\ \phi_x = \max(\phi_x^+, \phi_x^-) \end{cases}$$

Appendix C

Code Parallelisation

The simulations are computationally expensive and high performance computers are used. In order to reduce the simulations time, a computational domain is split into several sub-domains which can be calculated in different processors. Each sub-domain has halo cells which overlap its neighbour domains cells as shown in Fig. C.1. These halo cells keep the information necessary for the domain to compute derivatives, check interfaces and check level set errors. However, the information is calculated only in the domain where the cells belong to and not in the halo cells. Therefore, once the solution of the domains is calculated, information have to be exchanged to the halo cells so the neighbour domains have the information they need to calculate the next solutions.

All the scalars (temperature, energy and species), velocities and pressure are exchanged between domains as indicated in Figure C.1. As TVD schemes are used for the scalars, the number of halo cells rows passed is 2. For velocities and pressure only one row of halo cells is passed. The lateral parallelisation is explained in detail in (Marquis and Wille, 2008).

The level set, however, requires 3 rows of halo cells and corners exchanges (see Figure C.2) because of the WENO scheme in the reinitialisation procedure and in order to check the existence of interfaces. Figure C.2 shows the way the corners exchanges are done. Extra information about diagonal neighbours must be passed so these exchanges can be done.

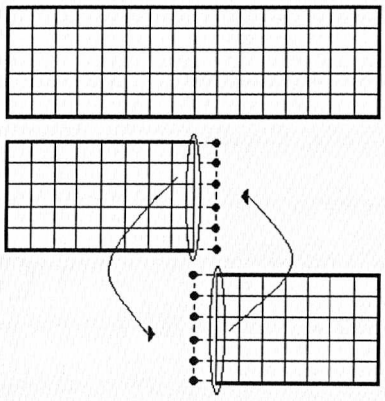

Figure C.1: Basic scheme of halo cells for the left-side sub-domain

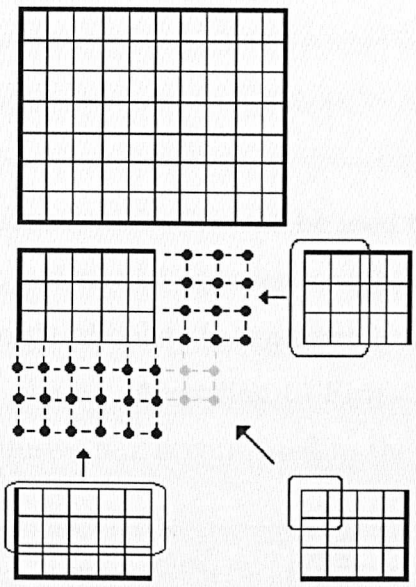

Figure C.2: Scheme of halo cells with level set information for the upper left-side sub-domain

The communication between processors is implemented using Message Passing Interface (MPI) routines.

Appendix D

Non-inertial droplet - near droplet zone

If binary diffusivity is assumed, Fick's law can be used to model diffusivity. In this appendix, this law is used to derive an equation for mixture fraction as a function of radial distance for non-inertial droplets (when there is no relative velocity between the droplets and the gas phase). According to Fick's law and following a radial coordinate system, the diffusive flux is correlated to the concentration field by

$$(f_d - f)\dot{m}_d'' = -\rho D \frac{df}{dr} \tag{D.1}$$

where $\dot{m}_d = 4\pi r^2 \dot{m}''$.

Integrating Equation (D.1) from a point at r to r_∞, we get

$$\int_r^{r_\infty} \frac{1}{r^2}\, dr = -\frac{4\pi\rho D}{\dot{m}_d} \int_f^{f_\infty} \frac{1}{(f_d - f)}\, df \tag{D.2}$$

Defining, $R_v = \frac{\dot{m}_d}{4\pi\rho D}$, we can write

$$-\frac{1}{r} + \frac{1}{r_\infty} = \frac{1}{R_v} \ln\left(\frac{f_d - f}{f_d - f_\infty}\right). \tag{D.3}$$

So the mixture fraction, f correlates with radial distance by

$$f = f_d - (f_d - f_\infty)\exp(-Rv/r). \tag{D.4}$$

As $\frac{\partial f}{\partial r} >> \frac{\partial f}{\partial l}$, scalar dissipation can be redefined as $N \equiv 2D\left(\frac{\partial f}{\partial r}\right)^2$. Moreover, being a new variable defined as $X = \frac{f-f_\infty}{f_d-f_\infty}$, Eq. (D.4) can be rewritten as

$$X = 1 - \exp(-R_v/r). \tag{D.5}$$

Therefore, $\frac{\partial X}{\partial r} = -\frac{1}{f_d-f_\infty}\frac{\partial f}{\partial r}$ and $\ln(1-X) = -R_v/r$,

$$\frac{\partial X}{\partial r} = -\frac{1}{R_v}(1-X)[\ln(1-X)]^2 \tag{D.6}$$

Expanding the natural logarithm in Taylor series (Mercator Series) gives

$$\ln(1-X) = -X - \frac{-X^2}{2} + \frac{-X^3}{3} - \frac{-X^4}{4} + ... \tag{D.7}$$

However, as $X < 1$ the terms with higher exponents can be neglected and then Eq. (D.6) becomes

$$\frac{\partial X}{\partial r} = -\frac{1}{R_v}(1-X)[-(X + \frac{X^2}{2})]^2 \tag{D.8}$$

which again, neglecting the high exponential terms, gives

$$\frac{\partial X}{\partial r} = -\frac{1}{R_v}X^2. \tag{D.9}$$

The scalar dissipation can be redefined as $N \equiv D\left(\frac{\partial f}{\partial r}\right)^2 = D\left(\frac{\partial X}{\partial r}\right)^2(f_d - f_\infty)^2$ so

$$N = \frac{D^3(4\pi)^2\rho^2}{\dot{m}_d}\frac{(f-f_\infty)}{(f_d-f_\infty)}. \tag{D.10}$$

Appendix E

Inertial droplet - near droplet zone

In spray flows, when the droplets move relatively to the gas phase, the heat and mass transport occur in the wake-like structures. Figure E.1 shows a scheme of the velocities of a turbulent wake.

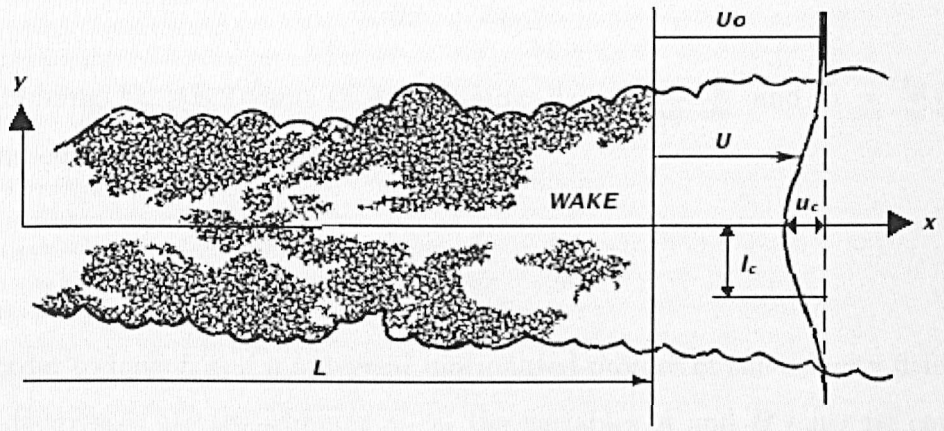

Figure E.1: Turbulent wake scheme (Tennekes and Lumley, 1972).

In this appendix, the principle of self-preservation (Tennekes and Lumley, 1972) is used to define an equation for mixture fraction as function of radial and axial distances for inertial droplets. Using this principle, the evolution of a flow can be determined by the local length and time scales. Moreover, the velocity defect and Reynolds stresses become invariant with respect to x (expressed as function of characteristic scales). Characteristic length and velocity which may change downstream

are defined as l_c and u_c, respectively. The non-dimensional length becomes $\epsilon = \frac{y}{l_c}$. The self-preserved variable is defined as

$$h = \frac{U_0 - U}{u_c}. \tag{E.1}$$

The momentum equation becomes

$$\frac{\partial U}{\partial x} = -\frac{du_c}{dx}h + \frac{u_c}{l_c}\frac{dl_c}{dx}\epsilon\frac{\partial h}{\partial \epsilon}. \tag{E.2}$$

Defining $-\bar{uv} = u_c^2 g(\frac{y}{l_c})$ where g is also a preserved variable,

$$\frac{\partial \bar{uv}}{\partial y} = -\frac{u_c^2}{l_c}\frac{\partial g}{\partial \epsilon}. \tag{E.3}$$

The momentum flux due to the cross-stream velocity fluctuations is

$$U_0\frac{\partial U}{\partial x} + \frac{\partial \bar{uv}}{\partial y} = 0. \tag{E.4}$$

Combining Eq. (E.2) and (E.4), defining $A = -\frac{U_0 l_c}{u_c^2}\frac{du_c}{dx}$ and $B = \frac{U_0}{u_c}\frac{dl_c}{dx}$, the following equation can be derived,

$$Ah + B\epsilon\frac{dh}{d\epsilon} = \frac{\partial g}{\partial \epsilon}. \tag{E.5}$$

In order to have h and g universal -normalised profiles of the velocity defect and Reynolds stresses are the same at all x- the variables A and B must be constant. Being U_0 constant, A and B are constant if $l_c \propto x^n$ and $u_c \propto x^{n-1}$. In order to define a consistent value for n, the momentum integral is written as

$$U_0 u_c l_c \int_{-\infty}^{\infty} h d\epsilon - u_c^2 l_c \int_{-\infty}^{\infty} h^2 d\epsilon = \rho U_0^2 \theta \tag{E.6}$$

where $\theta = \int_{-\infty}^{\infty} \frac{U}{U_0}\left(1 - \frac{U}{U_0}\right) dy$.

As the second term on the right side is much lower than the first term,

$$u_c l_c \int_{-\infty}^{\infty} h d\epsilon = U_0 \theta. \tag{E.7}$$

and $u_c l_c$ must be independent of x so $x^n x^{n-1}$ must be independent of x. Therefore $n + n - 1 = 0$ and $n = 0.5$. This implies in

$$l_c \propto x^{0.5} \qquad u_c \propto x^{-0.5}. \tag{E.8}$$

Using the same principle of self-preservation for a new mixture fraction related preserved variable $h = \frac{f - f_\infty}{f_0}$ and $\eta = \frac{r}{l_c}$ where r is the radial direction. The fluctuation of mixture fraction is defined as θ and $-\bar{\theta v} = f_0 u_c g(\frac{y}{l_c})$.

The transport equation of mixture fraction is

$$U_0 \frac{\partial f}{\partial x} + \frac{\partial}{\partial x}(\bar{u\theta}) + \frac{\partial}{\partial y}(\bar{v\theta}) = \gamma \frac{\partial^2 f}{\partial x^2} + \gamma \frac{\partial^2 f}{\partial y^2}. \tag{E.9}$$

The second term on the left side and the first term on the right side are much smaller than the other terms therefore negligible. Rearranging the previous equation and rewriting in cylindrical coordinates, we get

$$U_0 \frac{\partial f}{\partial x} + \frac{\partial}{\partial r}(\bar{v\theta}) = \gamma \frac{\partial^2 f}{\partial r^2}. \tag{E.10}$$

Assuming $f_\infty = 0$, then $f = h f_0$. And as $\eta = \frac{r}{l_c}$, then $\frac{\partial}{\partial x} = \frac{\partial}{\partial \eta}\left(-\frac{\eta}{l_c}\frac{dl_c}{dx}\right)$. Equation (E.10) becomes

$$\frac{U_0}{f_0}\frac{l_c}{u_c}\frac{\partial f_0}{\partial x} h - \frac{U_0}{u_c}\frac{dl_c}{dx}\frac{\partial h}{\partial \eta}\eta = \frac{\partial g}{\partial \eta} + \frac{\gamma}{u_c l_c}\frac{\partial^2 h}{\partial \eta^2}. \tag{E.11}$$

The Peclet number is introduced as $Pe = \frac{u_c l_c}{\gamma}$ so the equation becomes

$$A_1 h - A_2 \frac{\partial h}{\partial \eta}\eta = \frac{\partial g}{\partial \eta} + Pe^{-1}\frac{\partial^2 h}{\partial \eta^2} = -B(h + \eta \frac{\partial h}{\partial \eta}). \tag{E.12}$$

Assuming eddy diffusivity is constant,

$$-B\eta h = (Pe_T^{-1} + Pe^{-1})\frac{\partial h}{\partial \eta}), \tag{E.13}$$

$$h = \exp(-\frac{1}{2}\eta^2). \tag{E.14}$$

Recovering the mass flux integral

$$2\pi f_0 U_0 l_c^2 \int_0^\infty \eta \exp(-\frac{1}{2}\eta^2) d\eta = J_1 \tag{E.15}$$

where $J_1 = J_m \frac{(f_d - f_\infty)}{\rho}$.

Therefore, f_0 is

$$f_0 = \frac{J_1}{2\pi U_0 l_c^2}. \tag{E.16}$$

As $h = \frac{f - f_\infty}{f_0}$, the mixture fraction becomes

$$f = f_\infty + \frac{J_1}{2\pi U_0 l_c^2} \exp(-\frac{1}{2}\eta^2). \tag{E.17}$$

As mentioned before, $l_c = k_l x^{0.5}$ so $\eta = \frac{r}{k_l x^{0.5}}$. Being $k_l = \sqrt{\frac{2D}{u_c}}$ the mixture fraction as a function of radial distance for inertial droplets becomes

$$f = f_\infty + \frac{J_1}{4\pi D x} \exp(-\frac{r^2}{4D\frac{x}{U_0}}). \tag{E.18}$$

Bibliography

Abramzon, B. and Sirignano, W. A. (1989). Droplet vaporization model for spray combustion calculations. *Int. J. Heat and Mass Transfer*, 32:1605–1618.

Adalsteinsson, D. and Sethian, J. A. (1999). The fast construction of extension velocities model in level set methods. *J. Comp. Phys.*, 148:2–22.

Andrianov, N. and Warnecke, G. (2004). The riemann problem for the baernunziato two-phase flow model. *J. Comp. Physics*, 195:434–464.

Apte, S. V., Gorokhovski, M., and Moin., P. (2003). Les of atomizing spray with stochastic modeling of secondary breakup. *Int. J. Multiphase Flow*, 29:1503–1522.

Babinsky, E. and Sojka, P. E. (2002). Modeling drop size distribution. *Prog. in Energy and Combust. Sci.*, (28):303–329.

Bilger, R. W. (2000). Future progress in turbulent combustion research. *Prog. Energy Combust. Sci.*, 26:367–380.

Bilger, R. W. (2010). A mixture fraction framework for the theory and modeling of droplets and sprays. *Comb. Flame (in press)*.

Bini, M. and Jones, W. P. (2009). Large eddy simulation of an evaporating acetone spray. *Int. J. Heat and Fluid Flow*, 30:471–480.

Birouk, M. and Al-Sood, M. M. A. (2010). Droplet evaporation in a turbulent high-pressure freestream - a numerical study. *Int. J. Thermal Sc.*, 49:264–271.

Birouk, M., Chauveau, C., and Gokalp, I. (2000). Turbulence effects on the combustion of single hydrocarbon droplets. *Int. J. Heat Mass Transfer*, 44:4593–4603.

Brackbill, J. U., Kothe, D. B., and Zemach, C. (1992). A continuum method for modeling surface tension. *J. Comp. Phys.*, 100:335–354.

Castanet, G. and Lemoine, F. (2007). Heat transfer within combusting droplets. *Proc. Comb. Inst.*, 31:2141–2148.

Castro, C. E. and Toro, E. F. (2006). A riemann solver and upwind methods for a two-phase flow model in non-conservative form. *Int. J. Num. Methods in Fluids*, 60:275–307.

Chiu, H. H., Kim, H. Y., and Croke, E. J. (1982). Internal group combustion of liquid droplets. *Proc. Combust. Inst.*, 19:971–980.

Clift, R., Grace, J. R., and Weber, M. E. (1978). *Bubbles, Drops und Purticles.* Academic Press, Mechanics of Fluids.

Coyajee, E. R. A., Herrmann, M., and Boersma, B. (2004). Simulation of dispersed two-phase flow using a coupled volume-of-fluid/level-set method. *Proc. Summer Program, Center for Turbulence Research.*

Crank, J. and Nicolson, P. (1947). A practical method for numerical evaluation of solutions of partial differential equations of the heat-conduction type. *Proc.Cambridge Philos. Soc.*, 43:50–67.

Cristini, V., Blawzdziewicz, J., and Loewenberg, M. (2001). An adaptive mesh algorithm for evolving surfaces: simulations of drop breakup and coalescence. *J. Comp. Phys.*, 168:445–463.

Dean, A. J., Penyazkov, O. G., Sevruk, K. L., and Varatharajan, B. (2005). Ignition of aviation kerosene at high temperatures. *Proc. 20th ICDERS*, 1.

Dopazo, C. (1975). Probability density function approach for an axisymmetric heated jet: centerline evolution. *Phys. Fluids.*, 18:397.

Dopazo, C. and O'Brien, E. (1974). Functional formulation of nonisothermal turbulent reactive flows. *Phys. Fluids.*, 17:1968.

EIA, U. E. I. A. (2010). Total energy consumption and intensity. `http://www.eia.doe.gov/international/`.

Estrade, J.-P., Carentz, H., Lavergne, G., and Biscos, Y. (1999). Experimental investigation of dynamic binary collision of ethanol droplets - a model for droplet coalescence and bouncing. *International Journal of Heat and Fluid Flow*, 20:486–491.

Faeth, G. M. (1977). Current status of droplet and liquid combustion. *Prog. Energy Combust. Sci.*, 3:191–224.

Faeth, G. M. (1987). Mixing, transport and combustion in sprays. *Prog. Energy Combust. Sci.*, 13:293–345.

Faeth, G. M. (1996). Spray combustion phenomena. *26th Symposium (International) on Combustion, The Combustion Institute*, pages 1593–1612.

Faeth, G. M. and Lazar, R. S. (1971). Fuel droplet burning rates in a combustion gas environment. *AIAA. Journal*, 9(11):2165–2171.

Fedkiw, R., Aslam, T., Merriman, B., and Osher, S. (1999). A non-oscillatory eulerian approach to interfaces in multimaterial flows (the ghost fluid method). *J. Comp. Phys.*, 152:457–492.

Ferziger, J. H. and Peric, M. (2002). *Computational Methods for Fluid Dynamics.* Springer, CFD.

Frossling, N. (1938). Uber die verdunstung fallender tropfen. *Beytr. Geophys.*, 52:170–216.

Godsave, G. A. E. (1953). Studies of the combustion of drops in a fuel spray - the burning of single droplets of fuel. *Proc. Comb. Inst.*, (4):818–830.

Godunov, S. K. (1959). A difference scheme for numerical solution of discontinuous solution of hydrodynamic equations. *Math. Sbornik*, 47:pp. 271306. (Translated US Joint Publ. Res. Service, JPRS 7226, 1969).

Gueyffier, D., Li, J., Nadim, A., Scardovelli, S., and Zaleski, S. (1999). Volume of fluid interface tracking with smoothed surface stress methods for three-dimensional flows. *J. Comp. Phys.*, 152:423–456.

Hewitt, G. F. (1982). *Handbook of Multiphase Systems.* McGraw-Hill Book Co.

Imaoka, R. I. and Sirignano, W. A. (2005). Vaporization and combustion in three-dimensional droplet arrays. *Proc. Comb. Inst.*, 30:1981–1989.

Ishii, M. and Hibiki, T. (2006). *Thermo-Fluid Dynamics of Two-Phase Flow.* Springer US.

Jiang, G. S. and Peng, D. (2000). Weighted eno schemes for hamilton-jacobi equations. *J. Sci. Comput.*, 21:2126–2143.

Jiang, G. S. and Peng, D. (2007). A new smoothness indicator for the weno schemes. *J. Sci. Comput.*, 31:273–305.

Jones, W. P., di Mare, F., and Marquis, A. J. (2002). LES-BOFFIN: Users Guide. Technical Memorandum, Imperial College, London.

Jones, W. P. and Lettieri, C. (2010). Large eddy simulation of spray atomization with stochastic modelling of breakup. *J. Fluid Mechanics (submitted).*

Jones, W. P. and Lindstedt, R. P. (1988). Global reaction schemes for hydrocarbon combustion. *Combustion and Flame*, 73:233–249.

Keays, J. F. (2006). *Large Eddy Simulation of Premixed Combustion.* PhD thesis, Imperial College London.

Kerr, R. (1985). Higher order derivative correlations and the alignment of smallscale structures in isotropic numerical turbulence. *J. Fluid Mech.*, 153:31–58.

Klimenko, A. Y. and Bilger, R. W. (1999). Conditional moment closure for turbulent combustion. *Prog. Energy Combust. Sci.*, 25:595–688.

Kuo, K. K. (1986). *Principles of Combustion.* John Wiley and Sons.

Lebas, R., Menard, T., Beau, P. A., Berlemont, A., and Demoulin, F. X. (2009). Numerical simulation of primary break-up and atomization: Dns and modelling study. *Int. J. of Multiphase Flow*, 35:247–260.

Lederlin, T. and Pitsch, H. (2008). Large-eddy simulation of an evaporating and reacting spray. *Annual Research Briefs 9 Center for Turbulence Research*, pages 479–490.

Lefebvre, A. H. (1989). *Atomization and Sprays*. BookCrafters.

Liu, H.-F., Gong, X., Li, W.-F., Wang, F.-C., and Yu, Z.-H. (2006). Prediction of droplet size distribution in sprays of prefilming air-blast atomizers. *Chemical Engineering Science*, 61(6):1741–1747.

Liu, S., Hewson, J. C., Chen, J. H., and Pitsch, H. (2004). Effects of strain on high-pressure non-premixed n-heptane auto-ignition in counterflow. *Combustion and Flame*, 137:320–339.

Marquis, A. J. and Wille, M. (2008). Boffin for parallel computers. Technical Memorandum, Imperial College, London.

Miller, R. S., Harstad, K., and Bellan, J. (1998). Evaluation of equilibrium and non-equilibrium evaporation models for many-droplet gas-liquid flow simulations. *Int. J. Multiphase Flow*, 24:1025–1055.

Mortensen, M. and Bilger, R. W. (2009). Derivation of the conditional moment closure equations for spray combustion. *Combustion and Flame*, 156:62–72.

Nomura, H., Ujiie, Y., Rath, H. J., Sato, J., and Kono, M. (1996). Experimental study of high-pressure droplet evaporation using microgravity conditions. *Proc. Comb. Inst.*, 26:1267–1273.

Osher, S. and Sethian, J. A. (1988). Fronts propagating with curvature-dependent speed: algorithms based on hamilton-jacobi formulations. *J. Comp. Phys.*, 79:12–49.

OBrien, E. E. and Jiang, T. L. (1991). The conditional dissipation rate of an initial binary scalar in homogeneous turbulence. *Phys. Fluids*, A3:31213123.

Peng, D., Merriman, B., Osher, S., Zhao, H.-K., and Kang, M. (1999). A pde-based fast local level set method. *J. Comp. Phys.*, 155:410–438.

Pergamalis, H. (2002). *Droplet Impigement onto Quiescent and Moving Liquid Surfaces.* PhD thesis, Imperial College London.

Peters, N. (2000). *Turbulent Flows.* Cambridge University Press, Turbulent Combustion.

Poinsot, T. and Veynante, D. (2005). *Theoretical and Numerical Combustion.* Edwards Inc.

Pope, S. B. (1981). A monte carlo method for the pdf equations of turbulent reactive flow. *Combust. Sci. and Tech.*, 25:159–174.

Pope, S. B. (1985). PDF methods for turbulent reacting flows. *Prog. Energy Combust. Sci.*, 11:119–192.

Pope, S. B. (2000). *Turbulent Flows.* Cambridge University Press.

Potter, M. C. and Wiggert, D. C. (2002). *Mechanics of Fluids.* Brooks/Cole, Mechanics of Fluids.

Reitz, R. D. (1987). Modeling atomization processes in highpressure vaporizing sprays. *Atomisation and Spray Technology*, 3:309–337.

Renardy, Y. and Renardy, M. (2002). A parabolic reconstruction of surface tension for the volume-of-fluid method. *J. Comp. Phys.*, 183:400–421.

Renksizbulut, M. and Yuen, M. C. (1983). Experimental study of droplet evaporation in a high temperature air stream. *J. Heat Transfer*, 105:384–388.

Reveillon, J. and Vervisch, L. (2005). Analysis of weakly turbulent dilute-spray flames and spray combustion regimes. *J. Fluid Mechanics*, 537:317–347.

Sabel'nikov, V. and Soulard, O. (2005). Rapidly decorrelating velocity-field model as a tool for solving one-point fokker-planck equations for probability density functions of turbulent reactive scalars. *Phys. Rev.E*, 72:16301–163022.

Sazhin, S. S. (2006). advanced models of fuel droplet heating and evaporation. *Prog. Energy Combust. Sci.*, 32:162–214.

Scardovelli, R. and Zaleski, S. (1999). Direct numerical simulation of free-surface and interfacial flow. *Annual Rev. Fluid Mech.*, 31:567–603.

Schmidt, S. J., Sezal, I. H., Schnerr, G. H., Thalhamer, M., and Forster, M. (2007). Compressible simulation of liquid/vapour two-phase flows with local phase transition. *6th International Conference on Multiphase Flow.*

Schroll, P., Wandel, A. P., Cant, R. S., and Mastorakos, E. (2009). Direct numerical simulations of autoignition in turbulent two-phase flows. *Proc. Combust. Inst.*, 32(2):2275–2282.

Selvam, R. P., Lin, L., and Ponnappan, R. (2006). Direct simulation of spray cooling: Effect of vapor bubble growth and liquid droplet impact on heat transfer. *Int. J. Heat and Mass Transfer*, 49:4265–4278.

Shirani, E., Ashgriz, N., and Mostaghimi, J. (2005). Interface pressure calculation based on conservation of momentum for front capturing methods. *J. Comp. Phys.*, 203:154–175.

Shu, C.-W. (1988). Total-variation-diminishing time discretizations. *SIAM J. Sci. Statist. Comput.*, 9:1073–1084.

Smith, A. (2002). *Experimental Analysis of a Spray Impinging on a Plate.* PhD thesis, Imperial College London.

Stauch, R. and Maas, U. (2007). The auto-ignition of single n-heptane/iso-octane droplets. *Int. J. Heat and Mass Transfer*, 50:3047–3053.

Stauch, R. and Maas, U. (2008). Transient detailed numerical simulation of the combustion of carbon particles. *Combustion and Flame*, 52:4584–4591.

Subramaniyam, S., Ganesan, V., Rao, P. S., and Sampath, S. (1990). Turbulent flow inside the cylinder of a diesel engine - an experimental investigation using hot wire anemometer. *Experiments in Fluids*, (9):167–174.

Sussman, M., Smereka, P., and Osher, S. (1994). A level set approach for computing solutions to incompressible two-phase flow. *J. Comp. Phys.*, 114:146–159.

Tanguy, S., Menard, T., and Berlemont, A. (2006). A level set method for vaporizing two-phase flows. *J. Comp. Phys.*, 221:837–853.

Tanner, F. X. (1997). Liquid jet atomization and droplet breakup modeling of non-evaporating diesel fuel sprays. *SAE Technical Paper Series*, (970050).

Taylor, G. I. (1963). Generation of ripples by wind blowing over a viscous fluid. *In Scientific Papers of Sir G. I. Taylor*, 3:244–254.

Tennekes, H. and Lumley, J. L. (1972). *A First Course in Turbulence.* The MIT Press.

Turns, S. R. (1996). *An Introduction to Combustion: Concepts and Applications.* McGraw-Hill, Inc.

Unverdy, S. O. and Tryggvason, G. (1992). A front-tracking method for viscous, incompressible multi-fluid flows. *J. Comp. Phys.*, 100:25–37.

Valiño, L. (1998). A field Monte carlo formulation for calculating the probability density function of a single scalar in a turbulent flow. *Flow, Turb. Combust.*, 60:157–172.

Versteeg, H. K. and Malalasekera, W. (1995). *An Introduction to Computational Fluid Dynamics - The Finite Volume Method.* Pearson - Prentice Hall.

Veynante, D. and Vervisch, L. (2002). Turbulent combustion modeling. *Prog. Energy Combust. Sci.*, 28:193–266.

Wilke, C. R. (1950). A viscosity equation for gas mixtures. *J. Chem. Phys.*, 18:517–519.

Wu, J.-S., Liu, Y.-J., and Sheen, H. (2001). Effects of ambient turbulence and fuel properties on the evaporation rate of single droplets. *Int. J. Heat Mass Transfer*, (44):4593–4603.

Wu, P. K., Miranda, R. F., and Faeth, G. M. (1995). *Atomiz. Sprays*, 5:175.

Yanenko, N. N. (1971). The method of fractional steps. *Springer, Berlin.*

Yuen, M. C. and Chen, L. W. (1976). On drag of evaporating liquid droplets. *Comb. Sci. Tech.*, 14:147–154.

Yuen, M. C. and Chen, L. W. (1977). Heat transfer measurements of evaporating liquid droplets. *Int. Jour. of Heat and Mass Transfer*, 21:537–542.

Zhang, H. (2000). *Evaporation of a spherical moving fuel droplet over a wide range of ambient pressures within a nitrogen environment.* PhD thesis, University of Nebraska.

Zoby, M. R. G., Navarro-Martinez, S., and Kronenburg, A. (2009a). Mixture fraction pdf and dissipation in dense sprays. *Proc. of the 4th European Combustion Meeting.*

Zoby, M. R. G., Navarro-Martinez, S., Kronenburg, A., and Marquis, A. J. (2009b). Gas-phase mixing in droplet arrays. *Notes on Numerical Fluid Mechanics and Multidisciplinary Design (in press).*

Zoby, M. R. G., Navarro-Martinez, S., Kronenburg, A., and Marquis, A. J. (2010). Turbulent mixing in three-dimensional droplet arrays. *Int. J. Heat and Fluid Flow (submitted).*